Development of an Electromagnetic Glottal Waveform Sensor for Applications in High Acoustic Noise Environments

by

Altin Pelteku

A Thesis

Submitted to the Faculty

of the

WORCESTER POLYTECHNIC INSTITUTE

in partial fulfillment of the

Degree of Master of Science

in

Electrical Engineering

by

Altin Pelteku

January 2004

APPROVED:

Prof. Reinhold Ludwig, ECE Dept., WPI
Advisor

Prof. Gene Bogdanov, ECE Dept., WPI
Committee Member

Prof. Hossein Hakim, ECE Dept., WPI
Committee Member

Prof. Donald R. Brown III,
Committee member

Prof. Fred J. Looft,
Head of ECE Dept., WPI

Abstract

The challenges of measuring speech signals in the presence of a strong background noise cannot be easily addressed with traditional acoustic technology. A recent solution to the problem considers combining acoustic sensor measurements with real-time, non-acoustic detection of an aspect of the speech production process. While significant advancements have been made in that area using low-power radar-based techniques, drawbacks inherent to the operation of such sensors are yet to be surmounted. Therefore, one imperative scientific objective is to devise new, non-invasive non-acoustic sensor topologies that offer improvements regarding sensitivity, robustness, and acoustic bandwidth.

This project investigates a novel design that directly senses the glottal flow waveform by measuring variations in the electromagnetic properties of neck tissues during voiced segments of speech. The approach is to explore two distinct sensor configurations, namely the "six-element" and the "parallel-plate" resonator. The research focuses on the modeling aspect of the biological load and the resonator prototypes using multi-transmission line (MTL) and finite element (FE) simulation tools. Finally, bench tests performed with both prototypes on phantom loads as well as human subjects are presented.

Acknowledgements

This work was sponsored by the Defense Advanced Research Projects Agency (DARPA). Their support and feedback were invaluable to the completion of this work. I would like to extend many thanks my advisor, Prof. Reinhold Ludwig, for his optimism, leadership and encouragement throughout the term of this project. I would also like to thank the members of my committee: Prof. Brown for providing me with the opportunity to work on this project and for being a driven project manager, Dr. Gene Bogdanov for making the MTL tools available and carefully reviewing this document, and Prof. Hakim, who is a great teacher and person. I would also like to thank professor Jill Ruffs for dedicating time to construct the agarose neck model. Additional thanks go out to Todd Billings for helping out with many practical issues and the faculty of the Electrical and Computer Engineering department here at Worcester Polytechnic Institute. And finally, my deepest gratitude goes towards my parents and family, whose support and encouragement have helped me in all facets of life.

Table of Contents

List of Figures

List of Tables

1 Introduction

Detection of speech signals with non-acoustic methods has been previously attempted by different groups and organizations (see [1] [2] and [3], for instance). The idea has lately received renewed attention, primarily for measuring speech signals in high acoustic noise environments. The Defense Advanced Research Projects Agency (DARPA) has recently sponsored the Advanced Speech Encoding program, the goal of which, as stated by DARPA [4], is to "develop a voice communication concept that:

1. Requires very low bandwidth (~200 bps or less).
2. Provides excellent intelligibility (at least as good as the DoD 4800 bps std).
3. Suppresses external acoustic noise.
4. Can provide speaker authentication."[1]

The difficulty of measuring speech signals in high acoustic noise environments originates from the limitation of acoustic transducers: they are inept in differentiating between noise and speech on a fundamental basis. Limitations of traditional acoustic technology can be overcome by implementing multiple-sensor systems that combine acoustic with non-acoustic measurements of the speech signal. While such systems have proven to be effective in noise cancellation [5] and reconstruction of the original speech signal [1], significant challenges relating to sensitivity and robustness still remain (see Section 2.4). One important scientific goal is to develop new non-acoustic sensor ideas that offer improvements regarding sensitivity, bandwidth and immunity to complicated scattering environments. As a subset of the Advanced Speech Encoding program this

---

[1] http://www.darpa.mil/ato/programs/vocorder.htm

project determines the feasibility of the glottal resonator (GRES), a novel non-acoustic speech sensor.

1.1 Objective

The objective of this thesis is to determine the feasibility and quantify the performance of the glottal resonator (GRES) for the purpose of non-evasive measurements of the glottal waveform in high acoustic noise environments. The new sensor exploits the capacitive sensing technique as described in Section 2.1. The project goal is to design and built a prototype and evaluate its sensitivity to voiced speech.

The practical objectives for this project are to:

1. Develop a theoretical foundation that closely predicts the behavior of the sensor. The approach is to conduct a computer simulation study of GRES sensors using multi-transmission line and finite element analysis tools.
2. Construct prototypes of the GRES sensor and perform bench testing to determine the sensitivity to voiced speech.
3. Provide technical support in the collection of the experimental datasets for the GRES sensor prototype containing synchronized GRES sensor and acoustic measurements of at least two human subjects in a variety of standardized noise environments and noise levels.
4. Address practical implementation issues of the GRES sensors including sensitivity, ergonomics, potential health effects, acoustic bandwidth, electromagnetic field containment, and cost.

The approach is to explore two sensor designs: a coupled microstrip line resonator, and a parallel plate resonator. Both sensor designs measure variations in electromagnetic properties of human tissue near the region of the vocal folds during voiced segments of speech.

1.2 Organization

Following the Introduction, Section 2 of this thesis explores the basis of a novel non-acoustic speech sensor. Such material includes the anatomy of the vocal tract, sound production, and the dielectric properties of human tissues. Theoretical considerations are presented in Section 3, which includes: an overview of the resonator structures (Section 3.1), distributed resonator structures (Section 3.2), coupled transmission line TEM resonators (Section 3.3.1), multi-conductor transmission line model for TEM resonators (Section 3.5.1) and the full-wave finite element method (Section 3.5.2). Computer simulated results can be found in Section 4 with significant weight put on biological load modeling, field strength issues inside the load, and sensitivity to changes in the glottal state. Section 5 presents the implementation process for the two resonators built as part of this project. Results from the coupled microstrip line resonator (Section 5.1) and the parallel plate resonator (Section 5.2) are discussed. The thesis concludes with a summary of findings and future work in Section 6.

2 Background

This section presents the principle of operation of the GRES sensor and speech information relevant to the function of the sensor.

2.1 Principle of operation

The principle of operation of the glottal resonator sensor is based on two key aspects of speech production. First, it is known that during voiced segments of speech the vocal folds open and close at a rate equal to the fundamental frequency of the acoustic waveform produced at the output of the vocal tract. Second, experimental research shows that the relative permittivity of most body tissues near the position of the vocal folds is on the order of 40-200 times that of air for frequencies in the range of 20MHz-200MHz [6]. From these facts, it is presumed that during voiced segments of speech, the compound relative permittivity of a cross-section of the neck near the vocal folds experiences significant variations, while oscillating at the same fundamental frequency as the acoustic waveform output. This suggests that the glottal state and part of the acoustic waveform at the output of the vocal tract can be deduced from measurements of the relative permittivity of the larynx during voiced segments of speech.

In this project we investigate two separate designs for measuring the change in relative permittivity of the larynx. First, we discuss the "six-element" sensor that utilizes a coupled microstrip line transverse electromagnetic structure, driven by a low power (≤100 µW) radio frequency (RF) source operating around 200MHz. Second, a new sensor is developed that utilizes a tuned parallel plate resonator (PPRES) with a lower drive frequency (approximately 50MHz). Figure 2-1 can be illustrative for both sensors designs.

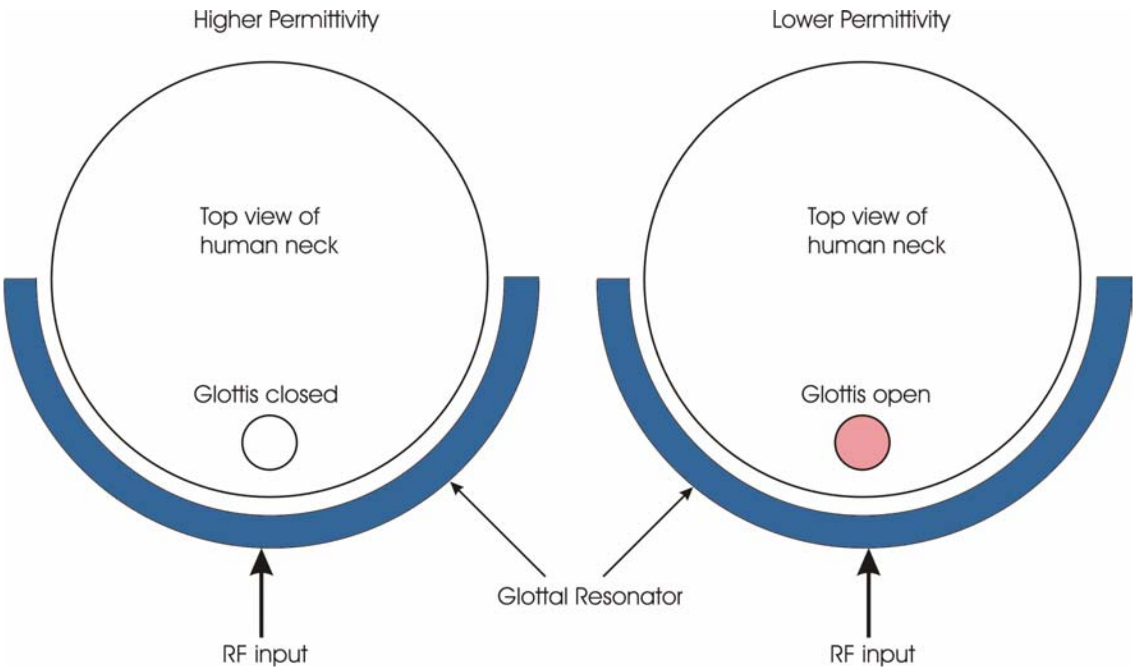

Figure 2-1: *Measurement of glottal state and change in relative permittivity.*

From the point of view of the RF drive circuit the resonator in conjunction with the neck area is simply seen as a load. The resonator's sensitivity to changes in relative dielectric permittivity can be quantified as changes in the load impedance $Z_{Load}(f)$. The goal is then to maximize the load impedance variations due to perturbations in electric permittivity; hence, capacitive sensing seems to be the logical approach. Let us consider the expression of a parallel plate capacitor:

$$C_{Load}(t) = \frac{\varepsilon_0 \varepsilon_r(t) \cdot A}{d} \qquad (1)$$

where A is the area of each plate, d the distance between them, ε_0 the electric permittivity of free space, and $\varepsilon_r(t)$ the time-dependent relative permittivity of the material between the plates. During voiced speech segments we can ignore geometric variations and regard permittivity value perturbations as the dominant factor. To simplify the analysis, we can consider the relative permittivity to be a sinusoidal function of time:

$$\varepsilon_r(t) = \varepsilon_{mag} \sin(\omega_{audio} t) \tag{2}$$

where ε_{mag} is the peak value of permittivity and ω_{audio} is the fundamental acoustic frequency. Changes can then be observed in the load capacitance at the same acoustic frequency:

$$C_{Load}(t) = \left(\frac{\varepsilon_0 \cdot A}{d}\right) \varepsilon_{mag} \sin(\omega_{audio} t) \tag{3}$$

Because of the glottis size, the load capacitance may experience relatively small perturbations during the glottal cycle, resulting in slight shifts in the resonance frequency of the sensor. By utilizing a well-matched resonator, the sensitivity due to small frequency shifts can be greatly enhanced. One way this can be implemented is by monitoring the input reflection coefficient of such resonator, while driving it at a fixed frequency at or near the resonance. The reflection coefficient is defined as the ratio of reflected voltage over the incident voltage:

$$\Gamma(f) = \frac{V_r}{V_i} = S_{11}(f) = \frac{Z_{Load}(f) - Z_0}{Z_{Load}(f) + Z_0} \tag{4}$$

where Z_0 is the characteristic line impedance that connects to the load and a one-port network configuration is assumed. The detection principle is depicted in Figure 2-2.

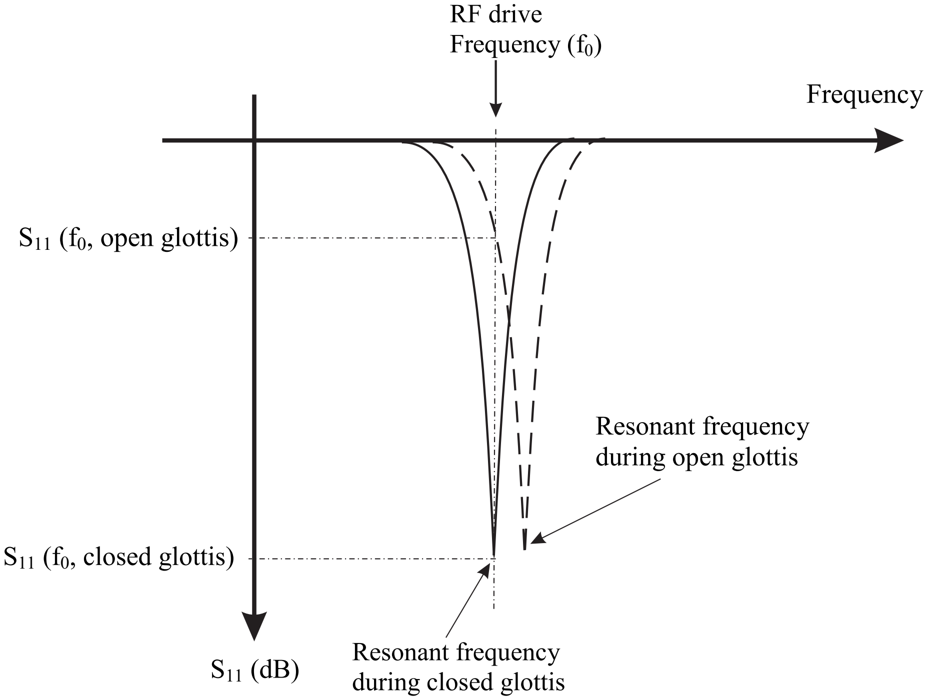

Figure 2-2: *S_{11} change in a tuned resonator when driven near resonance.*

By monitoring the return loss continuously we would be able to retrieve phonation at the glottal level (speech as it emerges from the glottis). Such information can be used in conjunction with microphone signals to filter out acoustic noise and finally reconstruct articulate speech in high noise environments.

2.2 Overview of the human speech process

A detailed description of the human speech process and the underlying physics will be given in this chapter. This will facilitate a better understanding of the principle behind the GRES sensor and will later aid in the construction of a human neck model.

2.2.1 Anatomy of the vocal tract

In order to convey a general picture of the human speech process we shall begin by looking at a functional block diagram of the vocal tract system (see Figure 2-3) as adopted from Clark and Yallop (1995) [7].

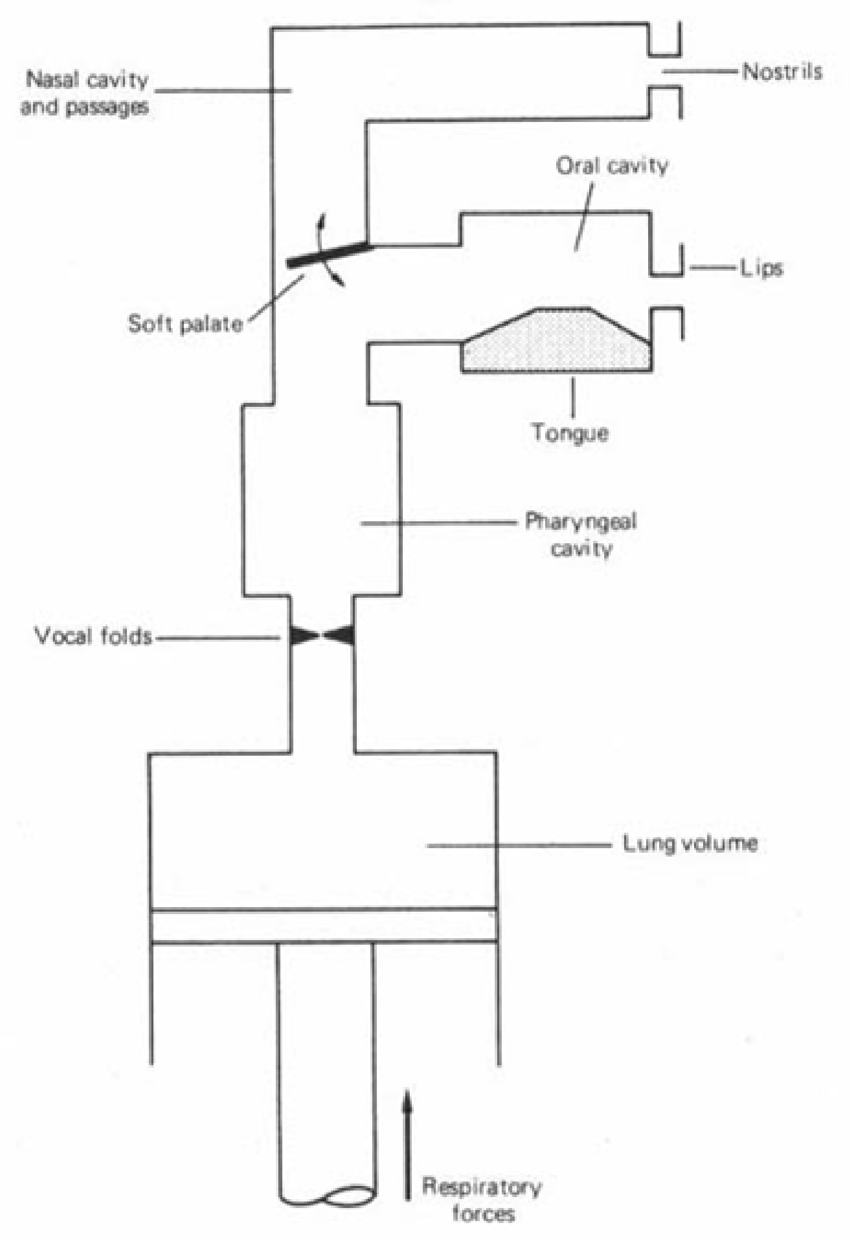

Figure 2-3: *Functional block diagram of the vocal tract structures.*

Let us next examine the vocal tract anatomy while entailing some of its important structures. Prior to presenting such material, however, we need to introduce some anatomical terms, summarized in Table 2-1.

Table 2-1: Summary of anatomical terms.

Anatomical term	Meaning
Anterior	Toward the front
Posterior	Toward the back
Superior	Above
Inferior	Below
Longitudinal	In the direction of
Transverse	Perpendicular to
Coronal	Frontal
Medial	Towards a center axis or a midplane
Lateral	Away from a center axis or a midplane
Sagittal	Along a median plane
Glottis	The air cavity between the vocal folds
Subglottal	Below the glottis
Supraglottal	Above the glottis

The vocal tract is part of the respiratory system; its main functional blocks are: the lungs, the larynx, the pharynx, the oral apparatus and the nasal cavities (see Figure 2-4). During voiced speech, flexure of the diaphragm causes the lung pressure to rise above atmospheric: usually between 0.3kPa and 1.2kPa [8] (where 1.2kPa is associated with loud voicing). As a result of the pressure difference to the outside world, a stream of air flows upwards into the larynx where phonation begins.

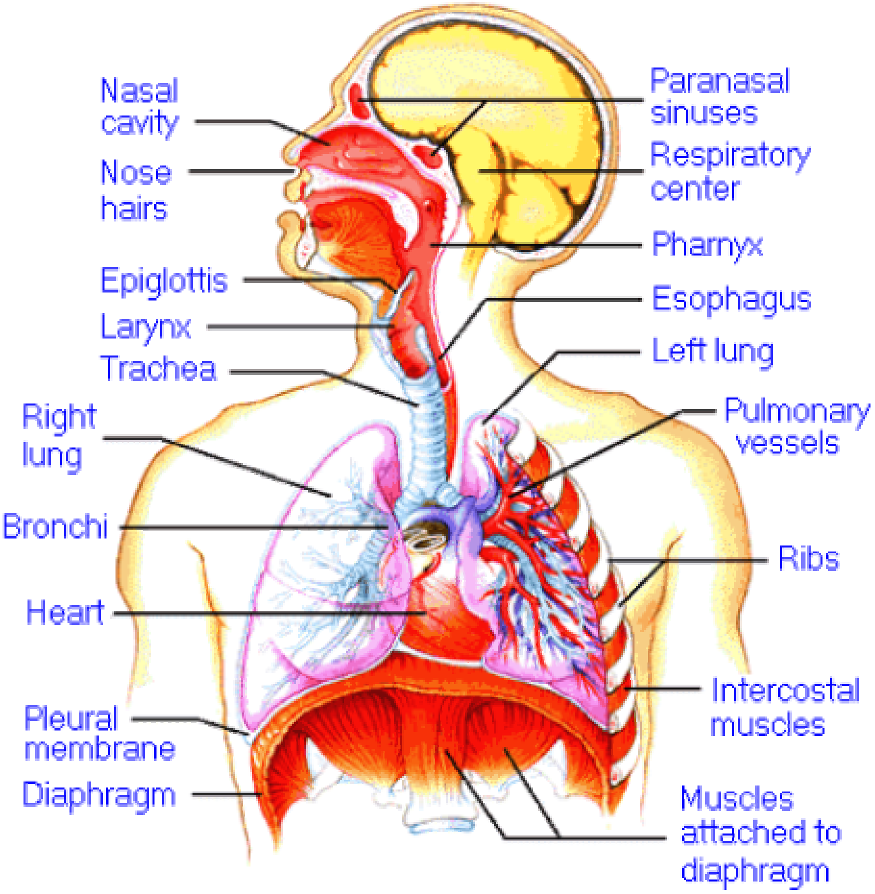

Figure 2-4: *Overview of the vocal tract [9]*.

The larynx itself is a flexible structure that begins with the uppermost tracheal rings and ends with the epiglottis. Its primary biological function is to prevent foreign substances from entering the lungs during inspiration. In addition, during expiration and/or voiced speech its cross section changes in order to regulate the airflow in the respiratory tract. A sagittal view of the larynx is shown in Figure 2-5.

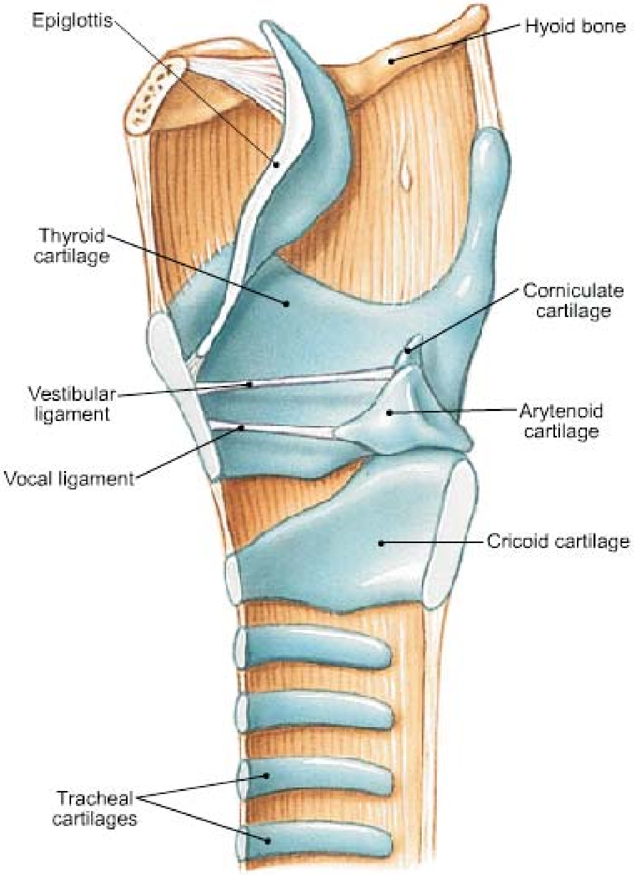

Figure 2-5: *Sagittal view of the laryngeal structures [10].*

Since the new sensor is to be worn near the area of the larynx, we need to review its constituent structures. The most relevant laryngeal structures to the speech formation process are the cricoid cartilage, the arytenoid cartilages (paired), the thyroid cartilage and the vocal folds. A posterior view of the laryngeal cartilages is shown in Figure 2-6.

The cricoid cartilage resembles the uppermost tracheal rings, yet it differs from them in its shape and functionality. It completely surrounds the trachea and is wider and taller posteriorly, giving it the form of a signet ring. The cricoid is attached to the thyroid cartilage via the cricothyroid joint, which is located at the articular facets, found on the lateral curvatures of the cricoid (see Figure 2-6). In addition, the cricothyroid muscle, which is subdivided in two groups, connects the two cartilages together. The function of these muscle groups is to move the anterior portion of the cricoid, also known as the arch, in the vertical direction. In the process, the length of the vocal folds changes and such movement is considered to be the primary pitch control mechanism.

The pyramidal-shaped arytenoid cartilages are positioned on top of the posterior section of the cricoid cartilage, forming what is known as the cricoarytenoid joint. This joint is flexible such that it allows lateral/medial and back/forward rotation of the arytenoids. The arytenoids connect to the cricoid via two muscle groups that oppose each other's action. First, the lateral cricoarytenoid muscle connects the posterior section of the arytenoid base, also known as the muscular process, to the superior portion of the cricoid's arch; this muscle group is used to move the arytenoids medially and forward, thereby closing the glottis. Second, the posterior cricoarytenoid muscle connects the muscular processes to the posterior surface the cricoid; this muscle group moves the arytenoids laterally and backwards, thereby opening the glottis. The opening and closing of the glottis is possible by such movement, since the anterior section of each arytenoid base, also known as the vocal process, is connected to the vocal ligament, which is an important part of the vocal folds. The major portion of the vocal folds, however, consists of the thyroarytenoid muscle that connects the arytenoids to the interior lamina of the thyroid cartilage.

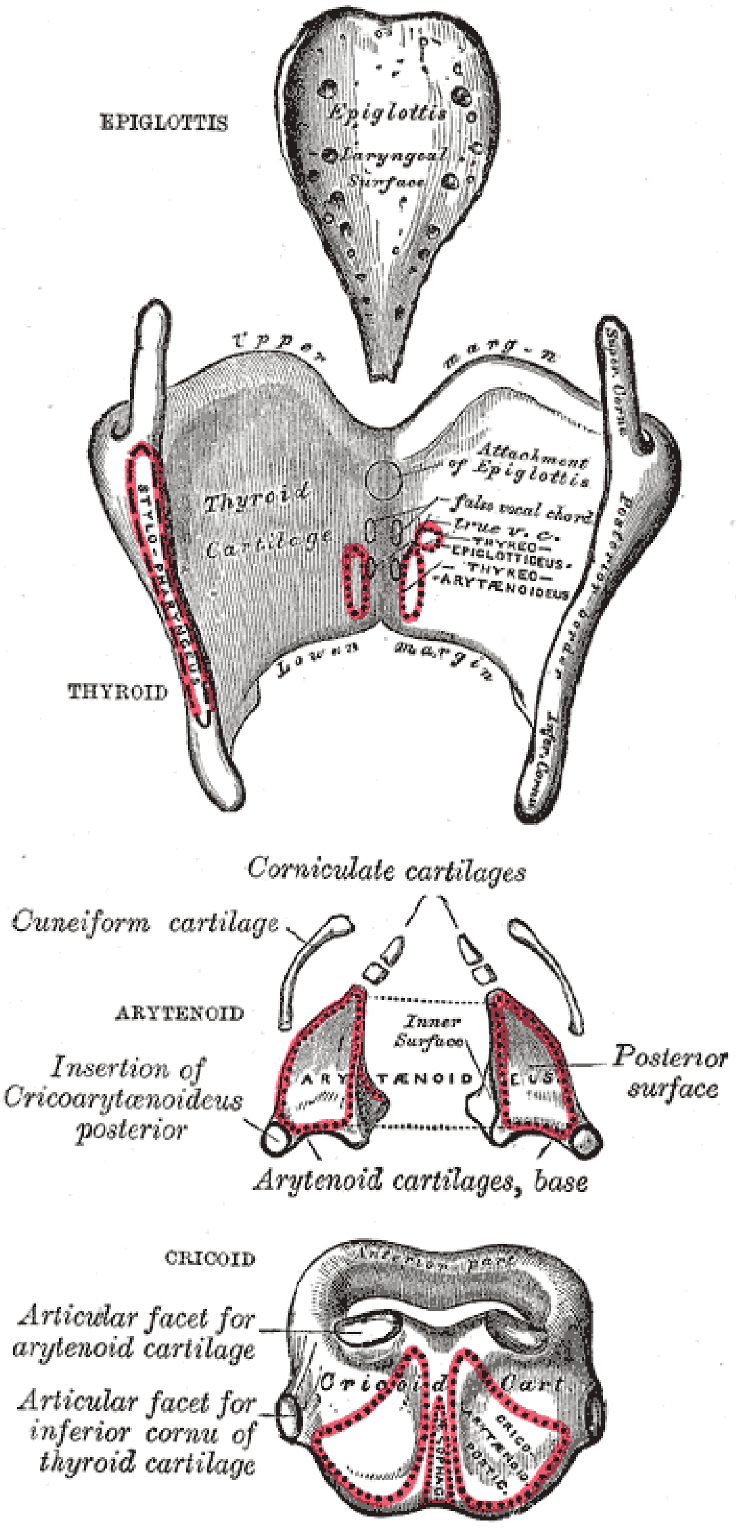

Figure 2-6: *Posterior view of the laryngeal cartilages [11].*

The thyroid cartilage itself has four ridges (or cornua) and a notch. The superior cornua are attached to the hyoid bone by means of a ligament, while the inferior cornua connect to the articular facets of the cricoid, forming the cricothyroid joint. The notch can be easily located by palpating one’s own "Adam’s Apple", or what is technically known as the laryngeal prominence. The anterior portion of the vocal folds is attached to the interior part of the prominence, while the posterior portions can open or close via rotation of the arytenoids.

A coronal view of the vocal fold area is shown in Figure 2-7. The epilethium, a skin-like structure, is the outermost layer of the vocal folds. It envelops the lamina propia, a fluidlike tissue. For convenience the lamina propia is divided into three layers: the superficial, the intermediate and the deep layer. The superficial layer resembles a loose arrangement of rubber bands; it consists of elastin fibers and as such it can easily elongate. The intermediate layer is composed in part of longitudinally oriented elastin fibers while having some layers of collagen fibers. The collagen fibers have a protein structure that restricts elongation; these fibers make up the bulk of the deep layer. Together, the intermediate and deep layers have a thickness of approximately 1 to 2mm; the two are alternatively labeled as the vocal ligament. After the lamina propia we find the thyroarytenoid muscle group, which makes up the bulk of the vocal folds with a thickness of about 7 to 8mm.

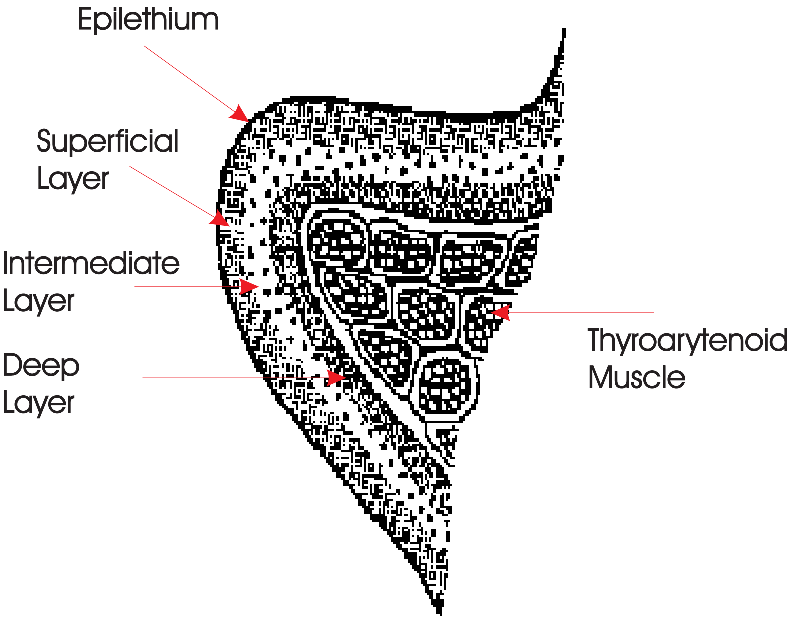

Figure 2-7: *Coronal view of the vocal folds [12].*

While the vocal folds are the primary sound source of voiced speech, articulation is performed in the oral and nasal cavities. The tongue, the lips, the jaw and teeth are all important instruments that take part in forming articulate speech. The function of the tongue is to change the cross-section area of the vocal tract output at different distances form the sound source (the vocal folds); this technique enables us to form different phonemes. Alternatively, the lips shape sound by changing the length of the vocal tract, which alters its resonance frequencies. The jaw employs similar technique during high-pitched screaming. The teeth also modify the resonance qualities of the tract, and are primarily important in the formation of fricative consonants like /s/ and /f/. (A list of American English phonemes can be found in [8] for example). The nasal cavity aids in the resonance qualities of speech by adding antiresonances or zeroes to the vocal tract transfer function [1]. Stated otherwise, it removes energy from the acoustic waveform at particular harmonics. The effect is more prominent during the production of nasal sounds (phonemes such as /m/, /n/), when the nasal tract is open and the oral cavity is shut off.

Now that we have a basic understanding of the constituent structures of the vocal tract we shall look at the sound production process. Sound propagation through the vocal tract can be found in several references [1][8], and is not explored here.

2.2.2 Sound generation

The vocal folds movement during voiced speech exhibits the properties of a mechanical oscillator. A model of the vocal tract area and the factors that aid in self-sustained oscillations of the vocal folds has been formulated by Titze [8] and is shown in Figure 2-8. This is a simplified spring-mass model with mass m, spring constant k and damping factor b.

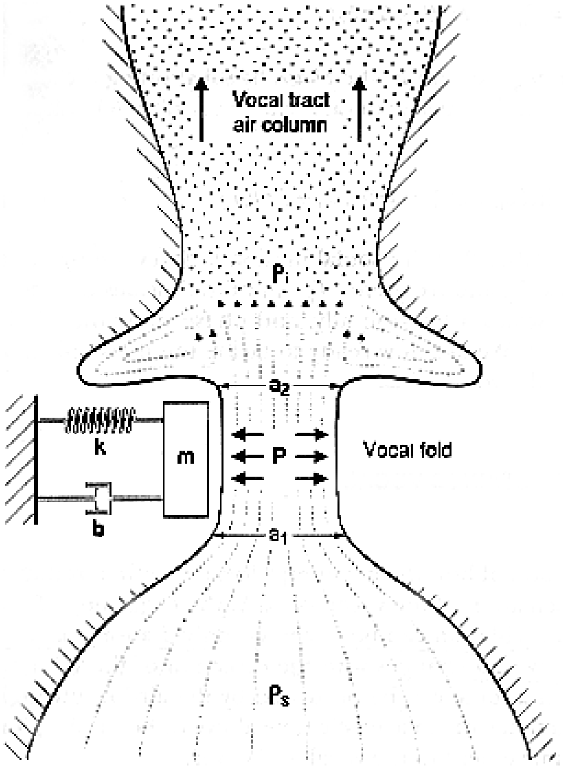

Figure 2-8: *The one-mass model of the vocal area [8].*

A brief description of the voiced speech process via the vocal fold vibration theory can be as follows: as phonation begins, an increase in relative lung pressure, P_s, forces the folds to partially open and air to flow through the glottis into the supraglottal region. This airflow causes the supraglottal and intraglottal pressures, P_i and P, to rise. The folds continue to open until equilibrium is reached: the force caused by intraglottal pressure balances internal forces acting the opposite way (the spring in Figure 2-8 is recoiled). This will coincide with the maximum distance reached between the vocal folds (or maximum glottal area). At this point the flow begins to decrease; however, the air column in the supraglottal region has inertia associated with it. The air column continues to move upwards causing a rarefaction (decrease in air density) above the vocal folds, which forces them to close.

As with any type of oscillator a compensating mechanism must be in place to neutralize any losses, such as friction forces that occur during the speech cycle. The compensating mechanism ensures that vocal fold vibrations are self-sustained, otherwise acoustical waves would “die-out” and speech would not be continuous. It has been shown mathematically [8] that the inertia of the air column in the supraglottal region during voiced speech serves such role. Based on such premise, vocal fold oscillations transform the airflow generated from the lungs into pressure pulses at the glottis, which propagate both in the subglottal and supraglottal directions.

The rate at which the folds vibration takes place is equal to the fundamental frequency of the acoustic wave at the output of the vocal tract. Since the airflow is modulated at the same rate during the glottal cycle, the glottal flow (airflow through the glottis) must correspond to a periodic waveform; however, this waveform is not a sinusoid (see [13] and [14] for example).

The harmonic content of the acoustic wave at the output of the vocal tract differs from the frequency spectrum of the glottal flow. It can be derived from the spectrum of the glottal flow by superimposing a particular frequency envelope (see [14] for example); the shape of this envelope differs from one phoneme to the other. From a system level point of view the speech process can then be described by the source-filter theory, which considers the vocal folds to be the sound source and the rest of the vocal tract as a filter with a certain transfer function (see Figure 2-9).

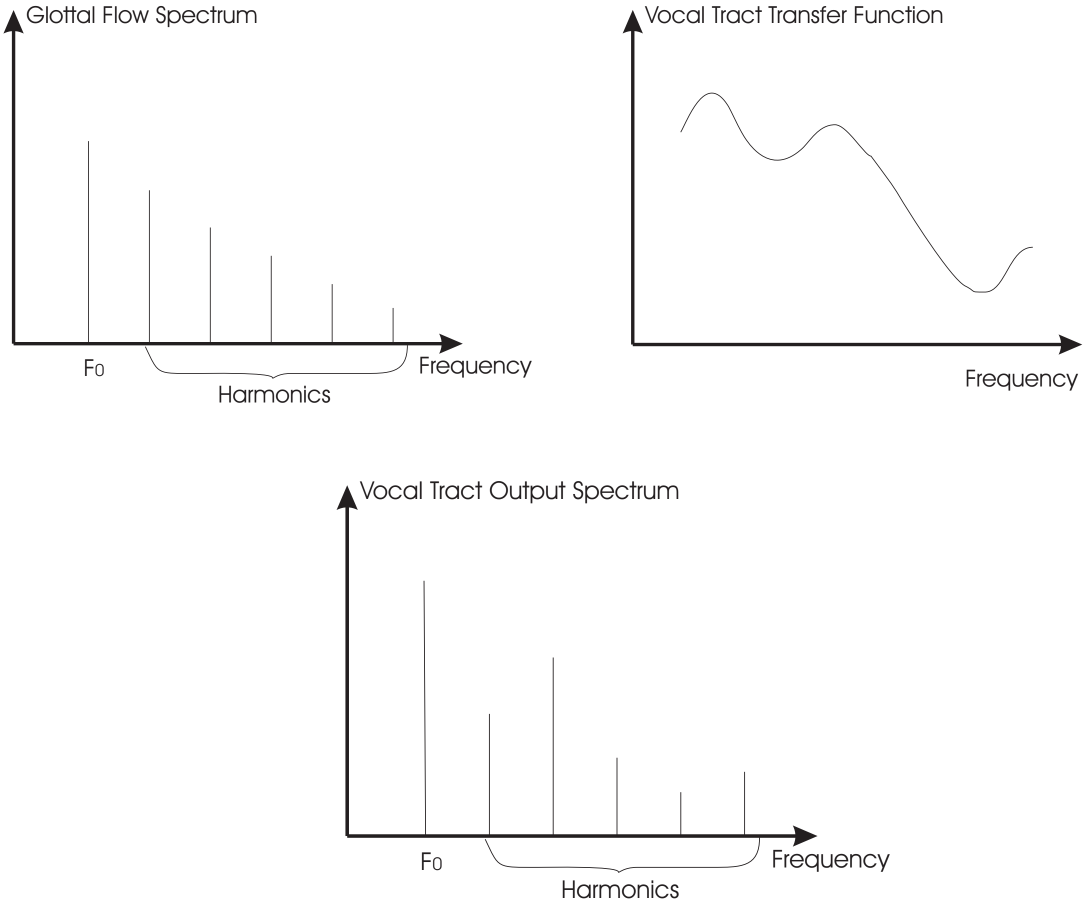

Figure 2-9: *The vocal tract output spectrum via the source-filter theory.*

By detecting volumetric changes in the dielectric properties of neck tissues near the position of the glottis, the GRES sensor is designed to provide “noise-free” measurements of the glottal flow waveform during voiced segments of speech. Research has shown that measurements of the glottal flow waveform (see Section 2.4) combined with acoustic sensor measurements can effectively yield the vocal tract transfer function and recover the speech signal in the presence of strong background noise.

2.2.3 Other speech sounds

There are additional speech sounds that are not produced during vibrations of the glottal area. These include fricatives. The generation of fricative sounds can be explained in terms of fluid dynamic quantities, where it is customary to study the flow of fluid through a quantity called the Reynolds number:

$$\mathrm{Re} = \frac{vh}{\mu} \tag{5}$$

where v is the particle velocity, h is the effective width of the orifice and μ is the kinematic coefficient of viscosity. This quantity helps to describe the flow of a fluid through a constriction; if a certain threshold value is exceeded, turbulence will be created at exit. Otherwise, the flow will be smooth or laminar.

Turbulence is the cause for the production of fricatives. When the opening of the glottis is small, its flow impedance increases. This causes a higher particle velocity, which means that the Reynolds number increases. Turbulent flow creates nearly random variations of air pressure in the glottis area, or otherwise stated an aperiodic acoustic source. Fricatives are produced when this aperiodic source is sustained over a sufficient amount of time [15]. In addition to fricatives there are speech sounds that may have more than one source: for example the voiced fricative /z/.

Because of the nature of fricatives, i.e. turbulence instead of vocal tract oscillations, we do not anticipate detecting them with the GRES sensor positioned around the neck (the electric permittivity does not change).

2.3 Dielectric properties of human tissue

In order for the sensor to be effective, we need to capitalize on the difference between air and human tissue relative permittivity. There is an abundance of measured data on the dielectric constant of different body tissues over a wide frequency range. In addition, researchers have focused on how to interpolate the empirical data into a function for the electric permittivity over a wide frequency range [6]. Such efforts enable us to obtain relative permittivity data over a wide frequency range. It is worthy to note two important things:

1. The value of the relative permittivity in the region of interest is on the order of 40-200 for most body tissues
2. The relative permittivity of all tissues experiences minimal change over a narrow band (even several MHz)

For example, the graphs in Figure 2-10 were produced from tabulated data retrieved from the Italian Research Health Council's website [6]:

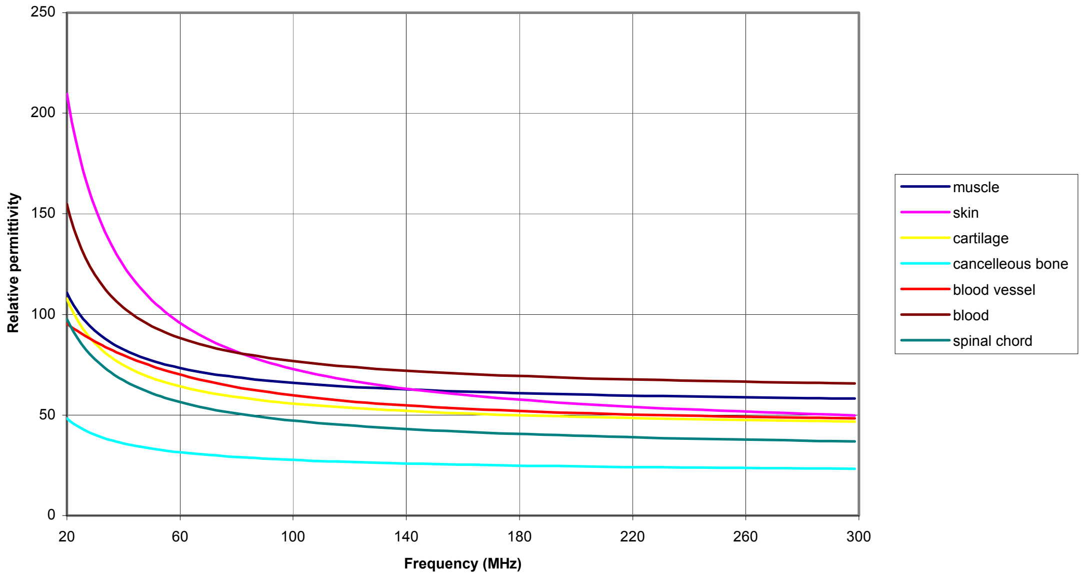

Relative permittivity (20-300MHz) for different body tissues

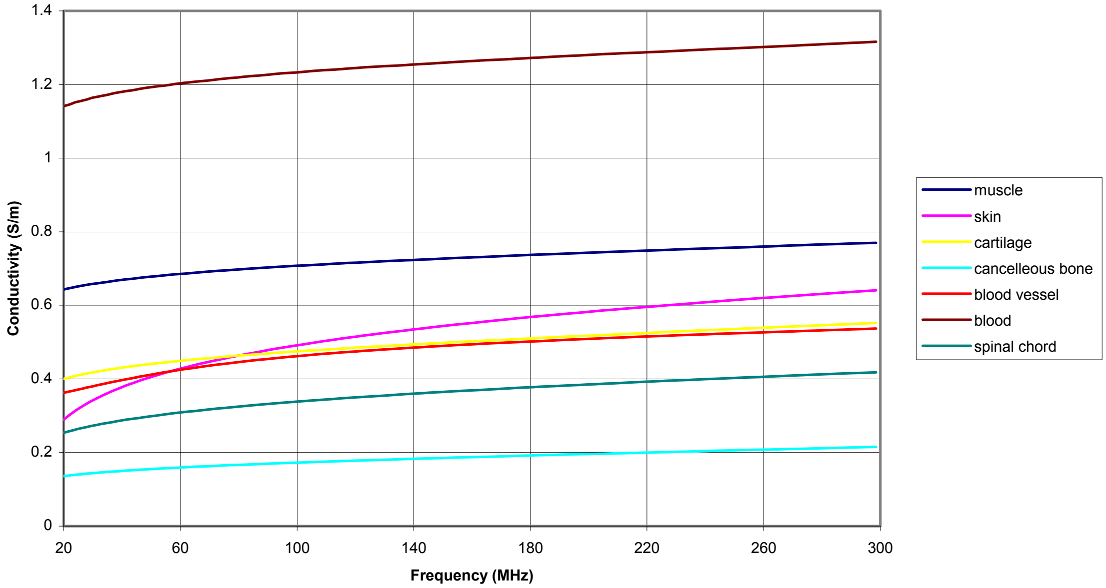

Conductivity (20-300MHz) for different body tissues

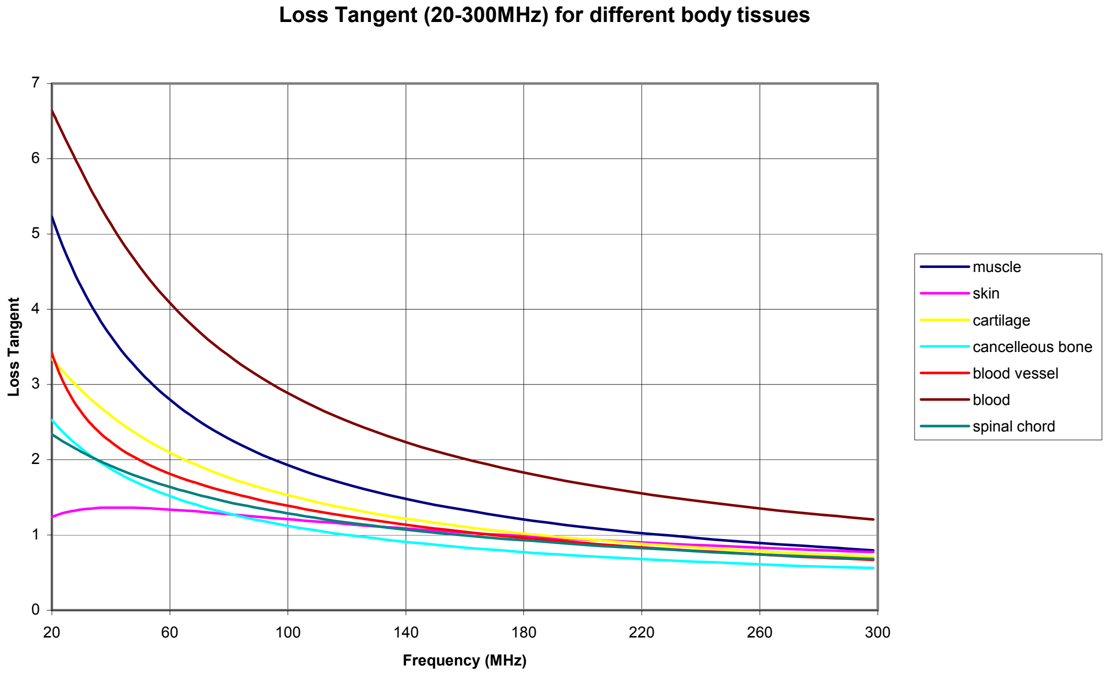

Figure 2-10: *Relative permittivity, conductivity and electric loss tangent for different body tissues in the frequency range 20-300MHz.*

2.4 Overview of existing non-acoustical speech detection techniques

Non-acoustic speech sensors measure an aspect of the speech process, therefore they are not meant to replace traditional microphones; they are rather used in combination with acoustic sensors to enhance signal quality in high-noise environments. Additional intended applications of these types of sensors include: very low bitrate speech encoding [16], studies of the speech process and speaker authentication, to name a few. Examples of non-acoustic speech sensors include the electroglottogram (EGG) [2], low-power radar-based sensors [1] and [17] and ultrasonic and photoelectric sensors [3].

Research in the area of non-acoustic speech sensors has recently focused on low power radar-based techniques. These sensors detect changes in the position of a vocal articulator based on the amount of time between the transmission and reception of a radar pulse. Radar-based sensors usually operate in the microwave region, i.e. 2GHz, and by utilizing the scattering properties of the microwave signal can obtain a reflection from a voice articulator's surface, such as a tracheal wall. When worn near the vocal fold region, radar-based sensors are able to obtain a signal related to subglottal pressure that is used as a means for defining an excitation function for the human vocal tract during voiced segments of speech [1]. The excitation function has been combined with acoustic measurements to describe the human vocal tract transfer function [18], as well as to provide a method for removing acoustic noise from speech signals [5].

One significant disadvantage of low-power radar vocal function sensors originates from their inherent reliance on accurately measuring the roundtrip-time of an RF pulse. Consequently, these types of sensors are sensitive to antenna alignment and positioning. In addition, the human vocal tract has several soft and hard tissue layers and that allows for multiple signal reflections. It has been observed that in the presence of complicated scattering environments, radar based sensors can produce ambiguous results [19]. The goal of this project is to overcome the aforementioned limitations of recently developed non-acoustic sensor technologies. One evident advantage of the GRES sensor is that by measuring an integrated effect of a cross section of the neck on a propagating electromagnetic field, the sensor is unaffected by complicated scattering environments.

3 Theoretical Considerations

This section presents two different configurations of the GRES sensor along with modeling methods used for predicting its behavior.

3.1 Lumped resonator structures

The basic building block of any resonator structure is LC-tank circuit (Figure 3-1), consisting of an inductor L and capacitor C. The resonance frequency of such system is well known to be $f_0 = \frac{1}{2\pi\sqrt{LC}}$. Clearly this is an idealized circuit that exhibits no power loss and infinite quality factor, Q, which is defined as: $Q = 2\pi \frac{\text{Peak energy stored}}{\text{Energy loss per cycle}}$. In general, the Q of a resonator is indicative of how sharp the impedance transition at resonance is. For the GRES sensor, a higher Q intuitively results in a higher sensitivity to changes in the relative permittivity during voiced segments of speech. However, Q is not the only factor that determines sensitivity of the sensor. If the sensor is well-matched at resonance, small perturbations in the load parameters cause large swings in the S_{11} magnitude response.

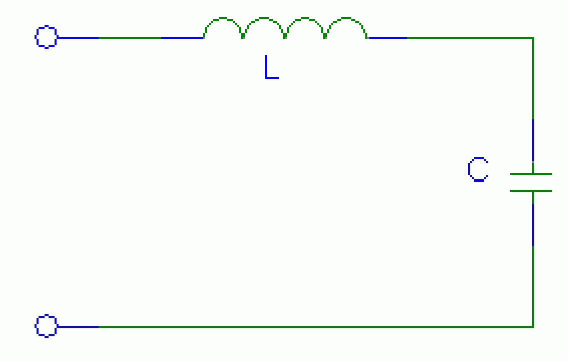

Figure 3-1: *The basic LC cell.*

To account for inherent losses in practical implementation of such structures, a resistance is added to the initial LC circuit. There are two commonly discussed resonator topologies, both of which will be summarized below:

1. The parallel RLC
2. The series RLC

The basic topology of the parallel RLC is shown in Figure 3-2. The resonance frequency of such topology is again: $f_0 = \frac{1}{2\pi\sqrt{LC}}$. The quality factor of the parallel RLC is found to be: $Q = \omega_0 RC = \frac{R}{\omega_0 L} = R\sqrt{\frac{C}{L}}$. In order for this circuit to have a high Q the parallel resistance must be fairly high compared to the impedance of either the inductor or capacitor.

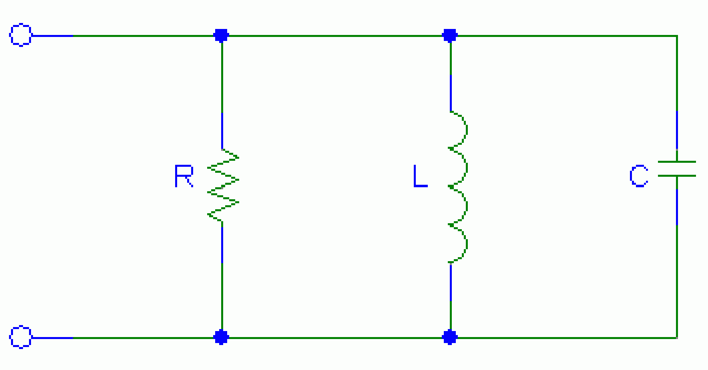

Figure 3-2: *The parallel RLC resonator.*

The basis topology of the series RLC is shown in Figure 3-3. The resonance frequency is the same as that of a basic LC cell: $f_0 = \frac{1}{2\pi\sqrt{LC}}$. The quality factor is found to be: $Q = \frac{\omega_0 L}{R} = \frac{1}{\omega_0 RC} = \frac{1}{R}\sqrt{\frac{L}{C}}$.

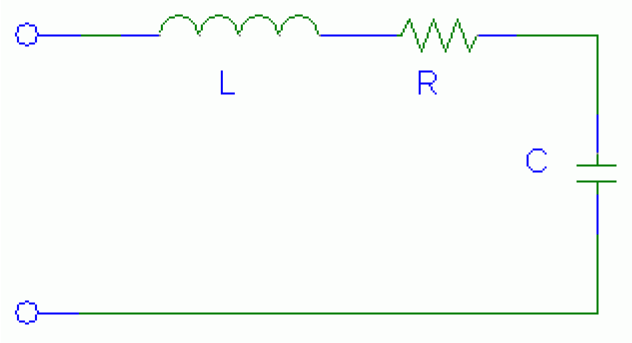

Figure 3-3: *The series RLC resonator.*

In order for this circuit to have a high Q the series resistance must be relatively small when compared to the impedance of either the inductor or capacitor. The series RLC topology is a simplified model of the "parallel plate" resonator (see Section 3.2.1).

3.2 Distributed resonator structures

Depending on the RF coil implementation, one or more of the lumped elements presented in the above figures can be implemented as distributed structures.

3.2.1 Parallel plate resonator

In the case of the "parallel plate" resonator, the capacitor is implemented as a distributed structure: two copper plates encompassing the vocal fold area. By means of the distributed capacitance an electric field is formed through the glottis to observe any changes in the relative permittivity that occur during the glottal cycle. The design originated as a series RLC configuration, where L is a lumped inductor that allows for tuning of the operating center frequency, which is normally around 50MHz. The series resistance is used to model losses that occur due to the conductivity of body tissues at the operating frequency. Since these losses are significant, the Q of the parallel plate resonator is expected to be low. Therefore, in order for such design to be sensitive to changes during the glottal cycle a good match must be achieved to the characteristic line impedance of the source, which from now on we will consider it to be 50Ω. The design is realized as a flexible collar that would fit around a person's neck and is shown in Figure 3-4.

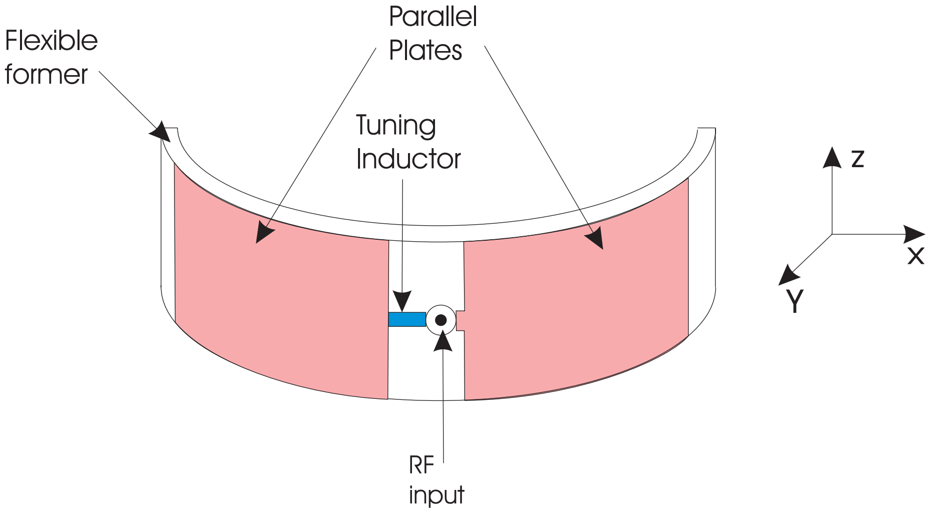

Figure 3-4: *Topology of the parallel plate resonator.*

Radiation currents

Before addressing impedance matching issues we will tackle a subtle problem that was observed with the initial design: the occurrence of radiation currents otherwise known as antenna currents. This effect is well known to antenna designers and is normally a problem for high-frequency devices. A traditional example involves a feeder cable and an antenna that have well matched impedances, yet significant reflections, much stronger than predicted from (4), can still be observed. The phenomenon is due to unequal current distributions at the feed point and is sometimes labeled as a "field mismatch" [20].

Consider the dipole antenna of Figure 3-5 connected directly to a coaxial cable of impedance Z_0. The transmission line currents are equal to each other, $I_1 = I_2$, and because of the skin effect are decoupled from environmental influences. On the other hand, the currents in each leg of the antenna may not be equal. Due to asymmetry radiating currents flow on the outside of the cable's shield, modifying the antenna's radiation pattern. Unbalanced antenna currents alter the S_{11} response of the resonator and add unwanted sensitivity to outside disturbances such as a conductor moving toward the coaxial cable. It is worthy to note that the magnitude of the radiating current on the outside of the shield depends on the impedance seen back at the feed point.

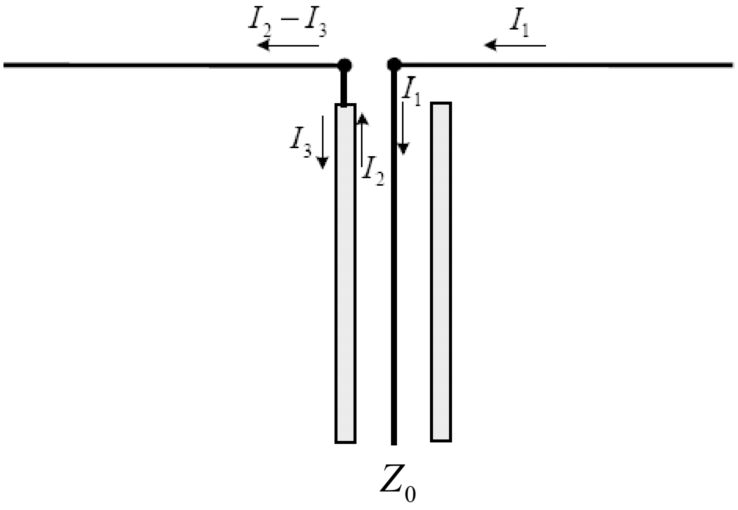

Figure 3-5: *Radiation currents due to unbalanced feed-point [20].*

Because the parallel plate resonator is a half-open system, it exhibits properties of an antenna, which is one of the indications that the resonator may not be modeled as a lumped impedance over a wide frequency range. To overcome limitations introduced by the aforementioned antenna effects a balanced design was investigated, whereas the tuning inductor of Figure 3-4 is divided in two equal halves that connect to each copper plate (see Figure 3-6); in this manner the resonance frequency stays the same as previously.

Normally, a balun is employed to join an unbalanced feed to a balanced antenna [21]. Baluns are usually divided into current baluns and voltage baluns [22] and [23]. Current baluns provide a high impedance to radiating currents at the feed point. Voltage baluns, on the other hand, provide differential voltage at the feed point. Voltage baluns may or may not suppress radiating currents locally, i.e. if the system is perfectly symmetric radiating currents will be suppressed. When considering the balanced design of Figure 3-6, the inductor connected to the shield of the cable acts as a current balun by presenting a high local impedance to radiating currents that flow back from the copper plate to the feed point.

Tuning and matching

It is well known that maximum power is transferred to a load, when the load impedance is the complex conjugate of the source impedance. For the parallel plate speech sensor a good impedance match means that the reflected voltage wave is small (most of the power is delivered to the load). When looking at a return loss plot a good match displays itself as a dip in the $S_{11}(f)$ response. Since it is unlikely that losses in the neck will equal to the characteristic impedance of the source, a matching network must be devised to transform the load impedance at resonance to 50Ω.

To resolve issues related to radiating currents flowing in the cable and to improve matching at resonance a balanced, well-matched design is introduced in Figure 3-6.

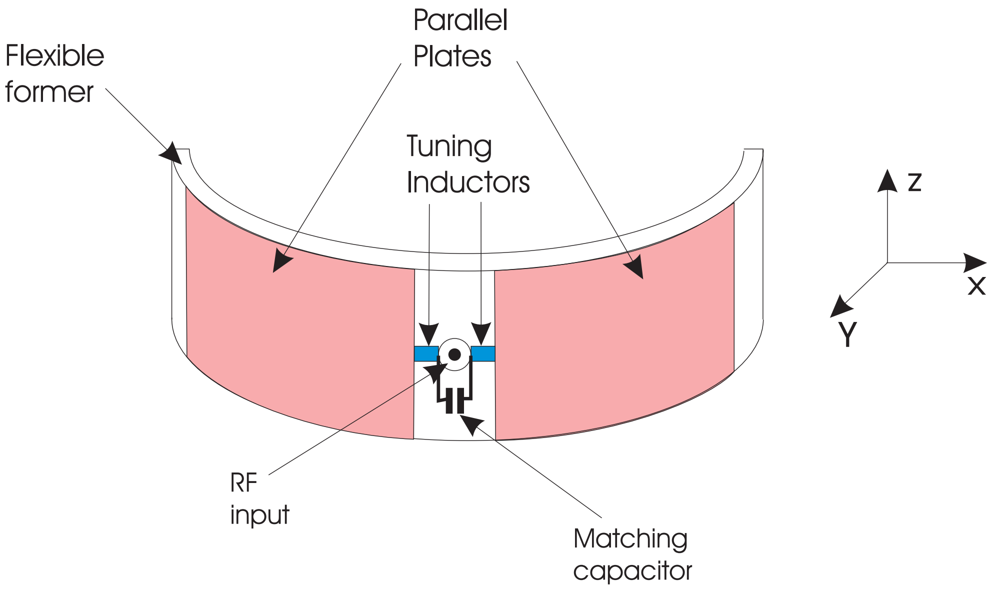

Figure 3-6: *Topology of the balanced, well-tuned parallel plate resonator.*

A lumped representation of the final resonator configuration is shown in Figure 3-7.

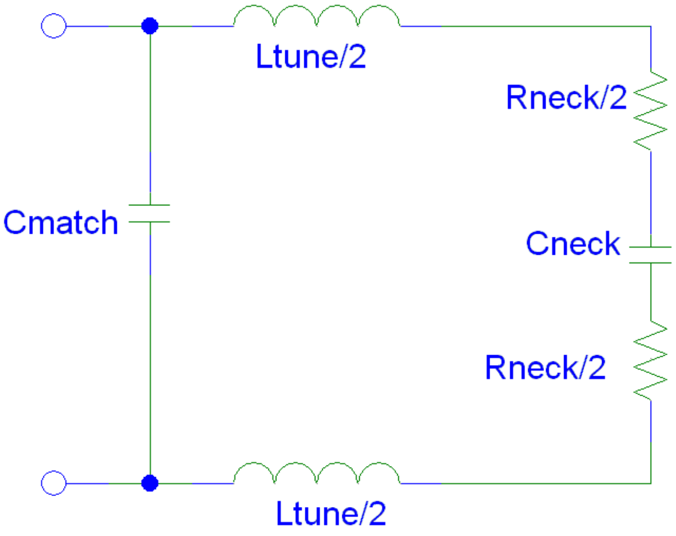

Figure 3-7: *Lumped representation of the balanced, well-tuned parallel plate resonator.*

Since a modeling tool will be used to predict the behavior of the sensor, the matching procedure will be as follows: the sensor will be simulated over the full range with tuning inductors shorted out and with matching capacitors left open. In this fashion we can determine the impedance at the desired resonance frequency. A matching program based on the well-known Smith Chart method (see [24], [25] and [26] for example) will be utilized to transform the sensor's impedance to the 50Ω characteristic line impedance of the source.

3.3 Six-element resonator

For the six-element resonator the distributed inductance is formed via the microstrip line between the inner copper strips and the outer copper shield. The inner strips are connected to the outer surface via terminating capacitors. This resonator configuration, shown in Figure 3-8, was inspired by high-field MRI applications [27]. The design was initially proposed to the project sponsor, the Defense Advanced Research Projects Agency (DARPA), because it has been observed that this coil is sensitive to changes in the biological load composition [28].

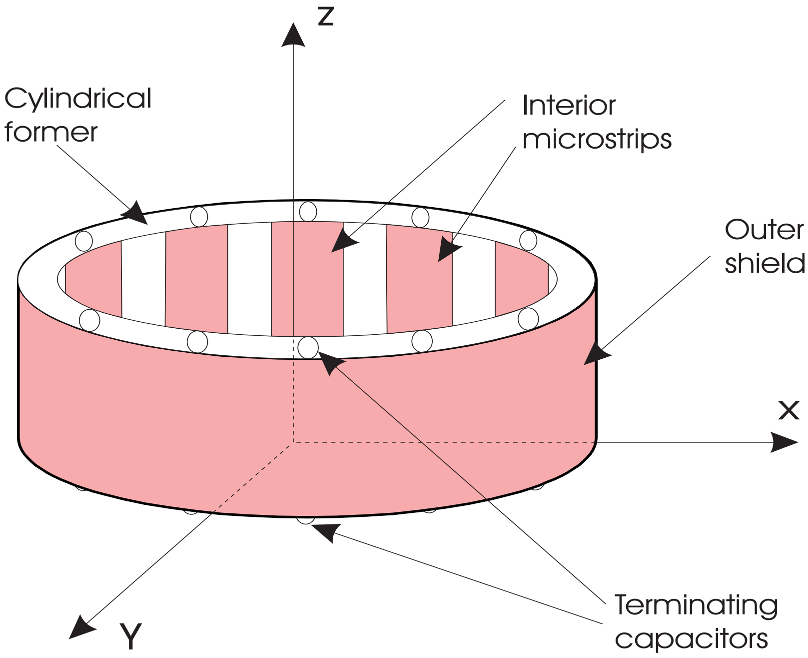

Figure 3-8: *Topology of the six-element resonator.*

Initially, the design was presented as a capacitive sensor (see [28]); however, its detection technique is based on conductive and eddy-current losses that occur during the glottal cycle. The simplest way to see this from a lumped element point of view is by considering the coupling between the coil elements, which is primarily inductive in nature (it resembles a transformer). In fact, the mutual inductance between the current-carrying strips has been an important parameter in the modeling of traditional MRI coils designs (see [29], [30] and [31]). Based on such premise and on the fact that the human tissue is conductive at the operating frequency, the time-varying magnetic field induces eddy-currents in the biological load; these losses modify the S_{11} response during voiced segments of speech.

A circuit representation of the final resonator configuration is shown in Figure 3-9.

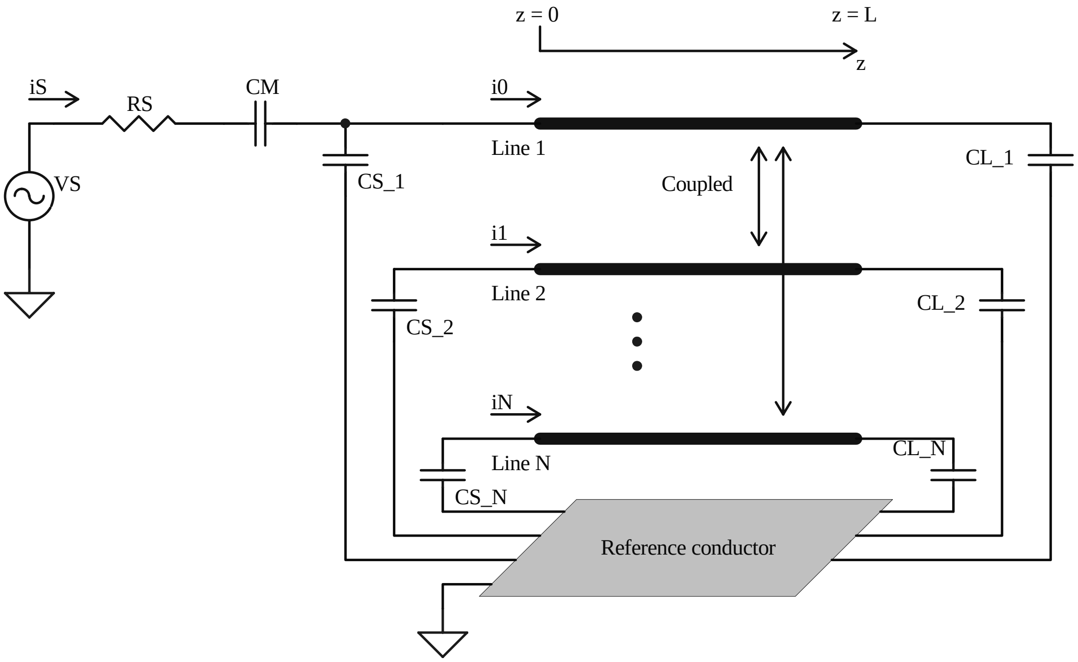

Figure 3-9: *Circuit representation of the six-element resonator [32].*

In order to make the sensor wearable, a half-open system will be utilized, i.e. the dielectric former will not cover 360°, but only a fraction of the full circle. The name six-element resonator is derived from the fact that only 6-inner strips are utilized.

3.3.1 Coupled microstrip line resonators

In general, a linear system can be represented as an N-port network system. In most practical implementations one-port or two port networks (see Figure 3-10) are encountered.

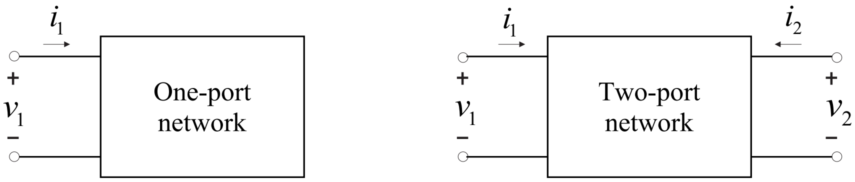

Figure 3-10: *Single-port and two-port network representation.*

Both proposed sensors are implemented as a single port network. The six-element resonator, however, has different LC-cells (see Figure 3-9), which are coupled between one another and can be characterized by two-port networks. Without knowing what is actually inside the “box” a two-port network can be characterized via its impedance Z-matrix that relates the port voltages to the port currents:

$$\begin{bmatrix} v_1 \\ v_2 \end{bmatrix} = \begin{bmatrix} Z_{11} & Z_{12} \\ Z_{21} & Z_{22} \end{bmatrix} \begin{bmatrix} i_1 \\ i_2 \end{bmatrix} \tag{6}$$

This network can be used as an equivalent model to a particular element of a complex resonating structure. The whole resonator can then be described by cascading several of these networks in order to come up with an overall model for the resonator. The best route to arrive at the overall model is by utilizing the ABCD or chain matrix. The Z-matrix can be converted into its ABCD-equivalent by the following formula:

$$\begin{bmatrix} A & B \\ C & D \end{bmatrix} = \begin{bmatrix} \dfrac{Z_{11}}{Z_{21}} & \dfrac{\Delta Z}{Z_{21}} \\ \dfrac{1}{Z_{21}} & \dfrac{Z_{22}}{Z_{21}} \end{bmatrix} \tag{7}$$

where $\Delta Z = Z_{11}Z_{22} - Z_{12}Z_{21}$. The overall ABCD-matrix would then be the product of the individual matrices. This idea is illustrated below (Figure 3-11).

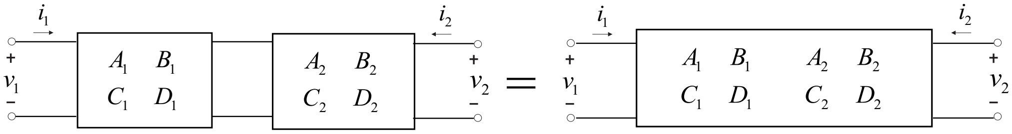

Figure 3-11: *Cascading of different networks via the ABCD representation.*

If we consider the mutual inductive coupling to be primarily influenced by the adjacent strip, then the six-element resonator can be represented as a series of the LC resonating cells. The entire structure can then be described by cascading the ABCD networks of the individual cells as depicted in Figure 3-11. This technique is valuable since the coupling between the resonating elements determines to a large extent the sensitivity of the six-element resonator, and in general that of a multi transmission line resonator. Since this method is only applicable for relatively low frequencies, a mathematical solution based on Maxwell's equations must be devised.

3.4 A review of Maxwell's equations

Obtaining field solutions via analytical or numerical techniques requires solving Maxwell's equations. In the frequency domain Maxwell's equations are presented in the differential form as:

$$\nabla \cdot \vec{D} = \rho \tag{8}$$

$$\nabla \cdot \vec{B} = 0 \tag{9}$$

$$\nabla \times \vec{E} = -j\omega\mu\vec{H} \tag{10}$$

$$\nabla \times \vec{H} = \vec{J} + j\omega\varepsilon\vec{E} \tag{11}$$

With the constitutive relationships:

$\vec{D} = \varepsilon\vec{E}$

$\vec{B} = \mu\vec{H}$

$\vec{J} = \sigma\vec{E}$

The above quantities are defined as:

$\vec{D}$: Electric flux density

$\vec{E}$: Electric field intensity

$\vec{B}$: Magnetic flux density

$\vec{H}$: Magnetic field intensity

ε: Electric permittivity

μ: Magnetic permeability

ρ: Electric charge density

$\vec{J}$: Impressed current density

In general, analytical solutions to Maxwell's equations become cumbersome and unfeasible even for distributed structures with modest complexities. So, in order to predict the frequency response and field values in and around the proposed resonator designs, a numerical modeling method is employed.

3.5 Modeling efforts

Several modeling methods exist, each offering certain advantages and disadvantages. The simplest method treats all coil elements and the load as lumped impedances, which is usually a good approximation at relatively low frequencies. As the structure size becomes comparable to the wavelength, so-called full-wave solvers based on Maxwell's equations must be utilized. Full-wave solvers discretize the solution domain and solve the governing partial differential equations (PDEs) by either explicit or implicit means. The most common techniques include finite differences, the method of moments and finite elements.

The finite difference time domain (FDTD) method solves the governing PDEs explicitly by using a marching in time technique. The field values are updated at the end of each time step and if the mesh size is chosen appropriately, field values converge to a stable state. Although this technique is relatively fast its main disadvantage rests on the fact that FDTD solvers cannot easily handle arbitrary geometrical shapes. The method of moments (MoM) is based on the integral formulation of Maxwell's equations. MoM generates results very fast, however, it cannot easily handle a complex biological load with different material properties and it scales worse than FDTD or the finite element method (FEM) due to fully populated matrices. The finite element method, on the other hand, can easily conform to arbitrary geometrically shaped objects with different material properties. FEM discretizes the solution domain into contiguous non-overlapping elements and interpolates the fields inside each element through so-called basis functions. Typical solution times with a FEM solver last from several hours to days depending on the desired accuracy and the availability of computational resources; hence, speed is the biggest drawback to the FEM.

In addition to these well-known techniques, the multi-conductor transmission line (MTL) theory has been recently implemented for predicting the behavior of MRI coils [27] and [32]. This particular MTL solver employs a boundary element method (BEM) in the transverse plane (xy-plane Figure 3-8), while considering transverse electromagnetic (TEM) propagation in the longitudinal direction (z-direction Figure 3-8). We discuss the MTL method and the FEM on the subsequent chapters.

3.5.1 Multi-conductor transmission line model

The MTL method can be utilized to predict the electromagnetic field distributions of a multi-conductor transmission line structure extruded in the z-direction. While the MTL tools were originally developed in [27] and [32], important principles that aid in the design of coupled microstrip line resonators, such as the six-element resonator, are presented here. In the frequency domain, the multi-conductor transmission line equations can be written in the following matrix form:

$$\frac{d}{dz}\begin{bmatrix}\mathbf{V}(z)\\ \mathbf{I}(z)\end{bmatrix}=\begin{bmatrix}\mathbf{0} & -\mathbf{Z}\\ -\mathbf{Y} & \mathbf{0}\end{bmatrix}\begin{bmatrix}\mathbf{V}(z)\\ \mathbf{I}(z)\end{bmatrix} \tag{12}$$

where **V**(z) and **I**(z) are column vectors that represent the voltage and current distributions along the longitudinal axis of the structure. In addition, $\mathbf{Z}=\mathbf{R}+j\omega\mathbf{L}$ and $\mathbf{Y}=\mathbf{G}+j\omega\mathbf{C}$ are the per-unit-length impedance and admittance matrices, respectively, which characterize the multi-conductor transmission line structure as a function of angular frequency $\omega = 2\pi f$. A boundary element numerical technique based on the Laplace's equation is employed to compute these matrices in the xy-plane [32].

In general, solution to the linear system represented by (12) is of the form:

$$\begin{bmatrix} \mathbf{V}(z) \\ \mathbf{I}(z) \end{bmatrix} = \mathbf{\Phi}(z) \begin{bmatrix} \mathbf{V}(0) \\ \mathbf{I}(0) \end{bmatrix} = \begin{bmatrix} \mathbf{\Phi}_{11}(z) & \mathbf{\Phi}_{12}(z) \\ \mathbf{\Phi}_{21}(z) & \mathbf{\Phi}_{22}(z) \end{bmatrix} \begin{bmatrix} \mathbf{V}(0) \\ \mathbf{I}(0) \end{bmatrix} \tag{13}$$

where $\mathbf{\Phi}(z)$ is the so-called chain-parameter matrix defined as:

$$\mathbf{\Phi}(z) = \mathbf{e}^{z\mathbf{A}}\ ;\ \mathbf{A} = \begin{bmatrix} \mathbf{0} & -\mathbf{Z} \\ -\mathbf{Y} & \mathbf{0} \end{bmatrix};\ \mathbf{e}^{z\mathbf{A}} = \mathbf{E} + z\mathbf{A} + \frac{z^2\mathbf{A}^2}{2!} + \frac{z^3\mathbf{A}^3}{3!} + \ldots \tag{14}$$

with $\mathbf{E}$ being the identity matrix.

As shown in [32], one useful solution can be derived from (13) when the load impedance matrix is known. If the load side contains no sources, the sensor's termination conditions at $z = 0$ and $z = L$ (see Figure 3-9) can be expressed as:

$$\begin{aligned} \mathbf{V}(0) &= \mathbf{Z}_{in}\mathbf{I}(0) \\ \mathbf{V}(L) &= \mathbf{Z}_L\mathbf{I}(L) \end{aligned} \tag{15}$$

where $\mathbf{Z}_{in}$ is the input impedance matrix of the MTL structure of length L terminated by a known load network $\mathbf{Z}_L$. Applying (15) to (13) yields the input impedance matrix:

$$\mathbf{Z}_{in} = \left[\mathbf{\Phi}_{11}(L) - \mathbf{Z}_L\mathbf{\Phi}_{21}(L)\right]^{-1}\left[\mathbf{Z}_L\mathbf{\Phi}_{22}(L) - \mathbf{\Phi}_{12}(L)\right] \tag{16}$$

Since $\mathbf{Z}_L$ is typically comprised of lumped elements such as terminating capacitors, the MTL formulation can combine lumped elements with distributed transmission line structures. It is evident from (16) that adjusting the values of terminating capacitors inherently alters the frequency response seen at the input side of the resonator. Once the input impedance matrix is computed, the source side of the TEM resonator is simulated as a lumped circuit (see Figure 3-9). As revealed in [32], the model is complete once the following Kirchhoff's Voltage Law (KVL) equations are solved:

$$\begin{bmatrix} [Z_{in}]_{1,1}+\frac{1}{j\omega C_{S\_1}} & [Z_{in}]_{1,2} & \cdots & [Z_{in}]_{1,N} & -\frac{1}{j\omega C_{S\_1}} \\ [Z_{in}]_{2,1} & [Z_{in}]_{2,2}+\frac{1}{j\omega C_{S\_2}} & & [Z_{in}]_{2,N} & 0 \\ \vdots & & \ddots & & \vdots \\ [Z_{in}]_{N,1} & [Z_{in}]_{N,2} & & [Z_{in}]_{N,N}+\frac{1}{j\omega C_{S\_N}} & 0 \\ -\frac{1}{j\omega C_{S\_1}} & 0 & \cdots & 0 & R_S+\frac{1}{j\omega C_M}+\frac{1}{j\omega C_{S\_1}} \end{bmatrix} \begin{pmatrix} i_1 \\ i_2 \\ \vdots \\ i_N \\ i_S \end{pmatrix} = \begin{pmatrix} 0 \\ 0 \\ \vdots \\ 0 \\ V_S \end{pmatrix} \tag{17}$$

where C_{S_i} is the capacitance terminating the i^{th} line at the source side, C_M is the matching capacitance, R_S is the source impedance, $i_{1\ldots N}$ are the input currents to the transmission lines, i_S is the source current, and V_S is the source voltage.

Finally, the system of equations in (17) is solved and the input impedance Z_{in} is computed as:

$$Z_{in} = \frac{V_S}{i_S} - R_S \tag{18}$$

Knowing the input impedance allows for the computation of the input reflection coefficient by:

$$\Gamma_{in} = \frac{[Z_{in} - R_S]}{[Z_{in} + R_S]} \tag{19}$$

where R_S denotes the characteristic impedance of the source, usually 50Ω. For a single port-network the input reflection coefficient is related to s-parameters by the expression $S_{11}(f) = \Gamma_{in}$. Therefore, the numerical results obtained through the MTL tools can be directly compared to s-parameter measurements obtained from a standard network analyzer.

Typically, the MTL method can predict the $S_{11}(f)$ response of the six-element resonator, including a biological load model inside it, within a matter of minutes on a standard personal computer. This great benefit renders the MTL method as a primary candidate for performing rapid design tasks.

3.5.2 Finite Element Frequency Domain Model

While the MTL simulator serves as a rapid design tool for quickly predicting the behavior of a multi-conductor structure, it cannot take into account radiation effects and eddy-currents induced by magnetic fields. In order to overcome these shortcomings of the MTL and more accurately predict the behavior of a given structure, a full-wave three-dimensional finite element formulation is adopted. The basic formulation rests on the double curl vector wave equation for the electric field:

$$\nabla \times \nabla \times \vec{E} = \omega^2 \mu \varepsilon \vec{E} - j\omega\mu\sigma\vec{E} \tag{20}$$

and the magnetic field:

$$\nabla \times \nabla \times \vec{H} = \omega^2 \mu \varepsilon \vec{H} - j\omega\mu\sigma\vec{H} \tag{21}$$

where we have assumed homogeneous material properties. These equations can be compressed by choosing a complex permittivity $\varepsilon = \varepsilon' - j\varepsilon'' = \varepsilon_0 \varepsilon_r$ and a complex permeability $\mu = \mu' - j\mu'' = \mu_0 \mu_r$:

$$\nabla \times \nabla \times \vec{E} - \omega^2 \mu \varepsilon \vec{E} = \vec{0} \tag{22}$$

$$\nabla \times \nabla \times \vec{H} - \omega^2 \mu \varepsilon \vec{H} = \vec{0} \tag{23}$$

where ε_r and μ_r are complex quantities.

There exist two standard FEM treatment techniques:

a) The variational method

b) The method of weighted residuals

In the following section we discuss the method of weighted residuals primarily because of its wide use and ease of implementation.

3.6 Weighted residual formulation

The method of weighted residuals takes the governing equation and approximates the field with a trial-function, for example in (22):

$$\vec{E} \cong \hat{E} = \sum_{j=1}^{n} E_j \vec{N}_j(x, y, z) \tag{24}$$

where $\vec{N}_j(x, y, z)$ are the user-specified basis functions, E_j the unknown coefficients and n is the number degrees of freedom. Consequently, an error or residual is obtained:

$$\nabla \times \frac{1}{\mu_r} \nabla \times \hat{E} - k_0 \varepsilon_r \hat{E} = \vec{R} \tag{25}$$

where: $k_0 = \omega\sqrt{\mu_0 \varepsilon_0}$ is the free space wave number. The method requires that the inner product of this residual with a user-specified weighting function, $\vec{W}$, over the whole volume (V) is forced to zero; this is equivalent to satisfying the governing equation in the weak form.

$$\int_V \vec{W} \cdot \vec{R} dv = \int_V \vec{W} \cdot \left(\nabla \times \frac{1}{\mu_r} \nabla \times \hat{E} - k_0{}^2 \varepsilon_r \hat{E} \right) dv = 0 \tag{26}$$

Expansion of the integral can be accomplished by utilizing the vector identity:

$$\vec{W} \cdot \left(\nabla \times \left(\nabla \times \hat{E} \right) \right) = \left(\nabla \times \hat{E} \right) \cdot \left(\nabla \times \vec{W} \right) - \nabla \cdot \left(\vec{W} \times \left(\nabla \times \hat{E} \right) \right) \tag{27}$$

and the divergence theorem:

$$\int_V \left(\nabla \cdot \hat{E} \right) dv = \oint_S \left(\hat{n} \cdot \hat{E} \right) ds \tag{28}$$

Application of (27) to (25) results in:

$$\int_V \vec{W} \cdot \left(\nabla \times \left(\frac{1}{\mu_r} \nabla \times \hat{E} \right) \right) dv = \int_V \left(\frac{1}{\mu_r} \left(\nabla \times \hat{E} \right) \cdot \left(\nabla \times \vec{W} \right) \right) dv - \oint_S \frac{1}{\mu_r} \hat{n} \cdot \left(\vec{W} \times \left(\nabla \times \hat{E} \right) \right) ds \tag{29}$$

where S is the surface enclosing the solution domain, and the normal $\hat{n}$ points away from the solution (integration) region. Using the clockwise property of the scalar triple-product:

$$\hat{n} \cdot \left(\vec{W} \times \nabla \times \hat{E} \right) = \vec{W} \cdot \left(\nabla \times \hat{E} \times \hat{n} \right) = -\vec{W} \cdot \left(\hat{n} \times \nabla \times \hat{E} \right) \tag{30}$$

the electric field formulation (26) reduces to:

$$\int_V \left(\frac{1}{\mu_r} \left(\nabla \times \vec{W} \right) \cdot \left(\nabla \times \hat{E} \right) - k_0{}^2 \varepsilon_r \vec{W} \cdot \hat{E} \right) dv = -\oint_S \frac{1}{\mu_r} \vec{W} \cdot \left(\hat{n} \times \nabla \times \hat{E} \right) ds \tag{31}$$

Proper choice of the basis functions enables us to implement the surface integral as an explicit impedance boundary. Perfect $\vec{E}$ and perfect $\vec{H}$ boundaries do not contribute to the surface integral while for radiation boundaries the region of interest has special tensor properties; boundary conditions will be explored in depth in Section 3.6.3

In order to implement the impedance boundary, the $\hat{n} \times \nabla \times \hat{E}$ term must be expanded. Since $\hat{E}$ represents the electric field, from equation (10) the wave equation can be converted into the following form:

$$\int_V \left(\frac{1}{\mu_r} \left(\nabla \times \vec{W} \right) \cdot \left(\nabla \times \hat{E} \right) - k_0{}^2 \varepsilon_r \vec{W} \cdot \hat{E} \right) dv = jk_0 \eta_0 \oint_S \vec{W} \cdot \left(\hat{n} \times \hat{H} \right) ds \tag{32}$$

where $\eta_0 = \sqrt{\frac{\mu_0}{\varepsilon_0}}$ is the intrinsic impedance of free space.

The lumped elements can be represented by surface patches, such as rectangles, of certain surface-wave-impedance:

$$\vec{E}_t = -Z_S \hat{n} \times \vec{H} \tag{33}$$

$$\vec{H}_t = \frac{1}{Z_S} \hat{n} \times \vec{E} \tag{34}$$

This result provides a theoretical tool for handling lumped impedance boundaries, such as the terminating capacitors depicted in Figure 3-8. Polylines are used to form surfaces connecting the strips to the ground plane; these surfaces emulate the four parallel-connected terminating capacitors. The E-field formulation in such a case becomes:

$$\int_V \left(\frac{1}{\mu_r} \left(\nabla \times \vec{W} \right) \cdot \left(\nabla \times \hat{E} \right) - k_0{}^2 \varepsilon_r \vec{W} \cdot \hat{E} \right) dv = -jk_0 \frac{\eta_0}{Z_S} \oint_S \left(\vec{W} \cdot \hat{E}_t \right) ds \tag{35}$$

By decomposing the electric field into a normal, $\hat{E}_n$, and tangential component, $\hat{E}_t$, where $\hat{E}_t = -\left(\hat{n} \times \hat{n} \times \hat{E} \right)$, equation (35) can be modified to:

$$\int_V \left(\frac{1}{\mu_r} \left(\nabla \times \vec{W} \right) \cdot \left(\nabla \times \hat{E} \right) - k_0{}^2 \varepsilon_r \vec{W} \cdot \hat{E} \right) dv = jk_0 \frac{\eta_0}{Z_S} \oint_S \vec{W} \cdot \left(\hat{n} \times \hat{n} \times \hat{E} \right) ds \tag{36}$$

Employing the property of the vector triple product:

$$\vec{W} \cdot \left(\hat{n} \times \hat{n} \times \hat{E} \right) = \left[\left(\hat{n} \cdot \hat{E} \right) \left(\hat{n} \cdot \vec{W} \right) - \vec{W} \cdot \hat{E} \right] = -\left[\left(\hat{n} \times \vec{W} \right) \cdot \left(\hat{n} \times \hat{E} \right) \right] \tag{37}$$

the E-field formulation can be finally brought to the form:

$$\int_V \left(\frac{1}{\mu_r} \left(\nabla\times\vec{W}\right)\cdot\left(\nabla\times\hat{E}\right) - k_0{}^2 \varepsilon_r \vec{W}\cdot\hat{E} \right) dv + jk_0 \frac{\eta_0}{Z_S} \oint_S \left(\hat{n}\times\vec{W}\right)\cdot\left(\hat{n}\times\hat{E}\right) ds = 0 \tag{38}$$

Although rarely used, a similar statement can be obtained for the magnetic field:

$$\int_V \left(\frac{1}{\varepsilon_r} \left(\nabla\times\vec{W}\right)\cdot\left(\nabla\times\hat{H}\right) - k_0{}^2 \mu_r \vec{W}\cdot\hat{H} \right) dv + jk_0 \frac{Z_S}{\eta_0} \oint_S \left(\hat{n}\times\vec{W}\right)\cdot\left(\hat{n}\times\hat{H}\right) ds = 0 \tag{39}$$

3.6.1 Domain discretization and matrix formulation

The solution domain is partitioned by deploying a desired number of nodes throughout the region of interest, while choosing the desired tessellation. Common implementations utilize tetrahedrons as the basic cell in order to make good approximations for arbitrary shaped objects. Consequently, basis functions are applied inside each basic cell. Using (24) the discretized formulation takes the form:

$$\sum_{j=1}^{N} \left(\int_V \left(\frac{1}{\mu_r} \left(\nabla\times\vec{W}_i\right)\cdot\left(\nabla\times\vec{N}_j\right) - k_0^2 \varepsilon_r \vec{W}_i\cdot\vec{N}_j \right) dv + jk_0 \frac{\eta_0}{Z_S} \oint_S \left(\hat{n}\times\vec{W}_i\right)\cdot\left(\hat{n}\times\vec{N}_j\right) ds \right) E_j = 0 \tag{40}$$

for *i*=1..*N*.

The different weighted residual formulations vary from each other in the way the weighting functions are selected. A widely used technique, the Galerkin, uses the same weighting functions as the basis functions:

$$\vec{W}_k = \vec{N}_k \tag{41}$$

The Galerkin formulation for the electric field now becomes:

$$\sum_{j=1}^{N} \left(\int_V \left(\frac{1}{\mu_r} \left(\nabla\times\vec{W}\right)_i\cdot\left(\nabla\times\vec{W}_j\right) - k_0^2 \varepsilon_r \vec{W}_i\cdot\vec{W}_j \right) dv + jk_0 \frac{\eta_0}{Z_S} \oint_S \left(\hat{n}\times\vec{W}_i\right)\cdot\left(\hat{n}\times\vec{W}_j\right) ds \right) E_j = 0 \tag{42}$$

for *i*=1..*N*. This result can be represented in the matrix form:

$$\mathbf{AE} = 0 \tag{43}$$

where $\mathbf{E}$ denotes the vector of unknown E-field coefficients, and $\mathbf{A}$ is the matrix with known elements:

$$A_{ij} = \int_V \left(\frac{1}{\mu_r} \left(\nabla \times \vec{W} \right)_i \cdot \left(\nabla \times \vec{W}_j \right) - k_0^2 \varepsilon_r \vec{W}_i \cdot \vec{W}_j \right) dv + jk_0 \frac{\eta_0}{Z_S} \oint_S \left(\hat{n} \times \vec{W}_i \right) \cdot \left(\hat{n} \times \vec{W}_j \right) ds \tag{44}$$

Since the $\mathbf{A}$ matrix is known, then it's a matter of choosing an efficient solver in order to obtain the values of the unknown coefficients. Ongoing research in this area includes devising more efficient banded matrix solvers and matrix preconditioning for faster convergence of iterative solvers such as conjugate gradient [33].

3.6.2 Basis function selection

The choice of basis functions determines to a large extent the accuracy of the FEM formulation. Generally speaking, the key ingredients in selecting a basis function are:

a) Selection of an orthogonal series basis function

b) Selection of a computationally efficient series

In the frequency domain formulation, a fully orthogonal basis set ensures that both conditions are satisfied:

$$\begin{gathered} \int_V \vec{W}_i \cdot \vec{W}_j dv = 0 \quad for \quad i \neq j \\ \text{and } \int_{V_e} \nabla \times \vec{W}_i \cdot \nabla \times \vec{W}_j dv = 0 \quad for \quad i \neq j \end{gathered} \tag{45}$$

If such basis set could be implemented in practice, the result would be a diagonal matrix the inversion of which is trivial. Computational efficiency can still be improved by properly choosing a nearly orthogonal basis set, the result of which is a sparse matrix structure. For example, the Lagrange polynomials find many uses in the solution of heat problems, where node-based interpolation is adequate for the divergence operators:

$$N_j = \prod_{j=1}^{k} \frac{(x - x_i)}{(x_j - x_i)} \tag{46}$$

where $i \neq j$; k = number of nodes in element and $N_j = 0$ for all nodes not in element.

In the solution of electromagnetic problems node-based interpolation is not well suited for the curl operator. Instead, edge or face basis functions are chosen. For example, the Whitney 1-form vector shape function associated with the edge between two adjacent nodes (i and j) takes the form:

$$W_{ij} = \lambda_i \nabla \lambda_j - \lambda_j \nabla \lambda_i \tag{47}$$

where λ_i and λ_j are the barycentric functions for the two nodes [34]. Higher order functions are possible, however, stretching the limits of the scope of this project we refer the interested reader to the appropriate literature [34].

3.6.3 Boundary Conditions

The finite element solution ensures that continuity of the electric and magnetic field is maintained between interfaces of different material boundaries.

$$\begin{gathered} \hat{n} \times \left(\vec{E}_1 - \vec{E}_2 \right) = 0 \\ \hat{n} \times \left(\vec{H}_1 - \vec{H}_2 \right) = \vec{J}_s \end{gathered} \tag{48}$$

Here the normal points from medium region 1 to region 2 and J_s is an impressed surface current density. Where the finite element mesh is terminated, additional boundary conditions can be imposed that are either of electric type

$$\hat{n} \times \vec{E} = 0 \tag{49}$$

specifying an electric wall boundary, or of magnetic type

$$\hat{n} \times \vec{H} = 0 \tag{50}$$

specifying a magnetic wall boundary.

In the case of an open region problem however, the FEM mesh must be terminated into a radiation boundary, which fully absorbs all fields impinging on it. We have applied the idea of a perfectly matched layer (PML) as initially proposed for solving finite difference time domain problems [35] and later adopted for FE formulations [36]. This technique describes an idealized medium that provides a reflectionless surface for all incident waves between the solution domain and the PML region. Consistent with Maxwell's theory, the divergence equation and Ampere's law for such a medium can be stated as:

$$\begin{gathered} \nabla \cdot \varepsilon_0 [\varepsilon_{PML}] \vec{E} = 0 \\ \nabla \times \vec{H} = j\omega \left[\varepsilon_{PML}\right] \varepsilon_0 \vec{E} + \vec{J} \end{gathered} \tag{51}$$

The special material is described with diagonally anisotropic material tensors:

$$[\varepsilon_{PML}] = \varepsilon_0 \begin{pmatrix} \varepsilon_x - j\dfrac{\sigma_E^x}{\omega} & 0 & 0 \\ 0 & \varepsilon_y - j\dfrac{\sigma_E^y}{\omega} & 0 \\ 0 & 0 & \varepsilon_z - j\dfrac{\sigma_E^z}{\omega} \end{pmatrix} \tag{52}$$

One way of implementing the PML method is to enclose the sensor in a sufficiently large air box and then add the special layers with appropriate tensors on top of it. For example, a PML wall in the xy plane corresponds to a z-directed tensor:

$$[\varepsilon_{PML}] = \begin{pmatrix} \alpha - j\beta & 0 & 0 \\ 0 & \alpha - j\beta & 0 \\ 0 & 0 & (\alpha - j\beta)^{-1} \end{pmatrix} \tag{53}$$

Where α and β can be chosen based on the frequency range, attenuation, the distance from the radiating source and the desired mesh size. It must also be noted that material tensors will be different for edge and corner PMLs and that the same procedure must be followed for the permeability tensors.

3.7 Simulation procedure

The simulation of the six-element resonator was initially conducted through the use of available MTL tools that have been developed for high-field MRI coils. For further refinement of the model and more accurate results, the FE analysis was carried out with commercially available software. Ansoft's HFSS 8.5 package was chosen, because of its reputation and the ability to handle lumped impedances. In general the use of the FEM solver model consists of three steps that include:

- Setup
    - Draw the coil geometry in the 3D modeler
    - Specify material properties for each object
    - Specify boundary conditions, including lumped impedances and sources
    - Apply radiation boundaries through available macros
- Solution
    - Set up a single frequency solution. Adaptive solutions will be employed to provide an acceptable level of accuracy.

  - The generated mesh may be further refined in order to get higher accuracy.
  - Based on the refined mesh, set up the desired sweep range, the field accuracy, the number of frequency steps and solve.
  - Because of the finite number of steps allowed for frequency sweeps, additional sweeps may be carried in order to zoom-in to a particular mode.
- Post-processing
  - Plot the S_{11} response of the resonator and save the data file.
  - Import the data file into Matlab where better manipulation of the plots can be carried through.
  - The electric field distribution at the mode of interest can be captured as a screenshot.

We next examine the results of various frequency sweeps for both resonators.

4 Numerical Simulations and Field Predictions

This section applies the MTL and FE methods to specific examples of the six-element and the parallel plate resonator. The behavior of each sensor is predicted in the context of changes during the glottal cycle.

4.1 Six element resonator

The six-element resonator design was initially modeled with the basic construction shown in Figure 3-8 and with specific parameters given in Table 4-1.

Table 4-1: Six-element resonator prototype design parameters.

Parameter	Value
Plexiglass former inner radius	69.8mm
Plexiglass former outer radius	76.2mm
Plexiglass former height	38.1mm
Number of interior microstrip lines	6
Width of interior microstrip lines (same for all)	21.21mm
Spacing between interior microstrip lines (same for all)	3.175mm
Total angle spanned by shield	120 degrees
Value of terminating capacitance	108pF

In order for the sensor to be easily worn around the neck, the cylindrical former spans a total angle of 120 degrees. As a result, there are only six copper-strips (hence the name six-element resonator) in the interior of the sensor. The MTL method was used to select values for the terminating capacitance for this design such that the first resonant mode would be placed around 195MHz. The appropriate terminating capacitance value was computed to be approximately 108pF.

4.1.1 MTL simulation results

Given this sensor design, the MTL tools can be applied to model the human neck and approximate the $S_{11}(f)$ response in two states: glottis open and glottis closed. The load model is a solid cylinder of muscle with radius of 67mm and a height of 38.1mm that includes a 12mm radius cylinder (same height) in the location of the glottis (see Figure 4-1). The material properties of the latter cylinder are alternated between muscle, in the closed glottis state, and air, in the open glottis state. The size of the glottis cylinder represents approximately 3.2% of the entire neck model volume, which in reality is overly generous. This was initially done as a proof of concept and to gain an understanding about the sensitivity of the sensor.

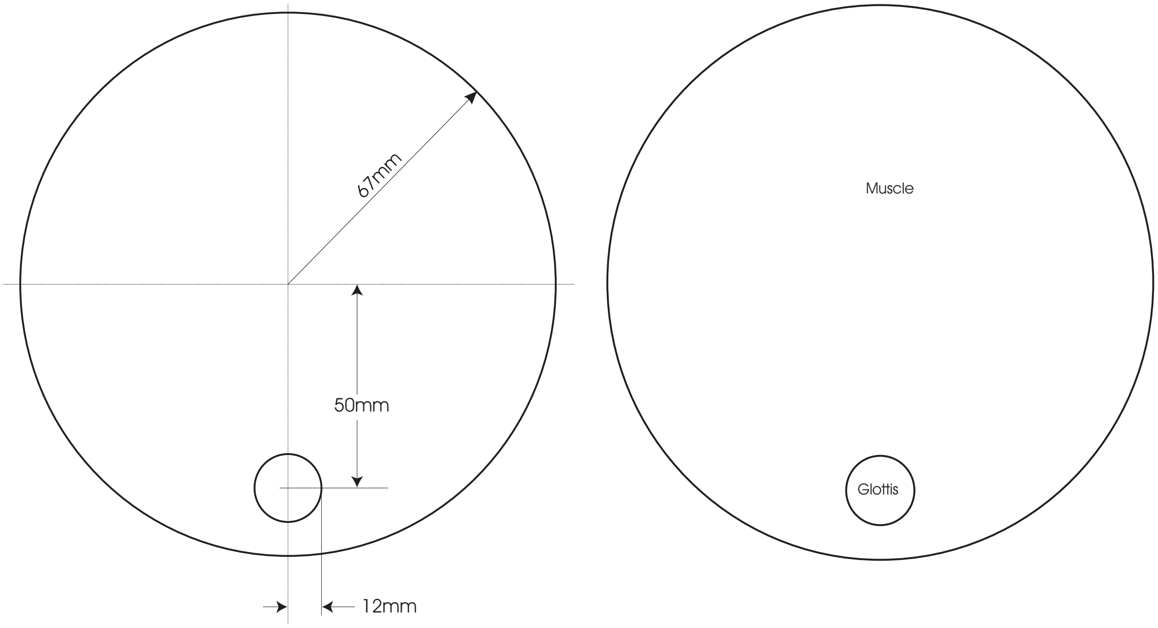

Figure 4-1: *Dimensions and materials of the MTL neck model. Note that all structures shown in this figure are cylindrical with a height of 38.1mm.*

The dielectric properties of body tissues consistent with the location of the larynx at 200MHz are given in Table 4-2.

Table 4-2: Dielectric properties of relevant tissues at 200MHz [6].

Body Tissue	**Relative Permittivity**	**Conductivity**
Skin	55.716	0.58229
Muscle	60.228	0.74307
Cartilage	49.161	0.51751
Blood	68.474	1.2802
Blood vessel	51.088	0.50861
Cancellous Bone	18.2	0.13
Spinal cord	39.70	0.38502

Figure 4-2 shows the $S_{11}(f)$ response in the open and closed glottis cases over the full simulation range, while Figure 4-3 and Figure 4-4 show detailed plots of the second and third resonant modes, respectively.

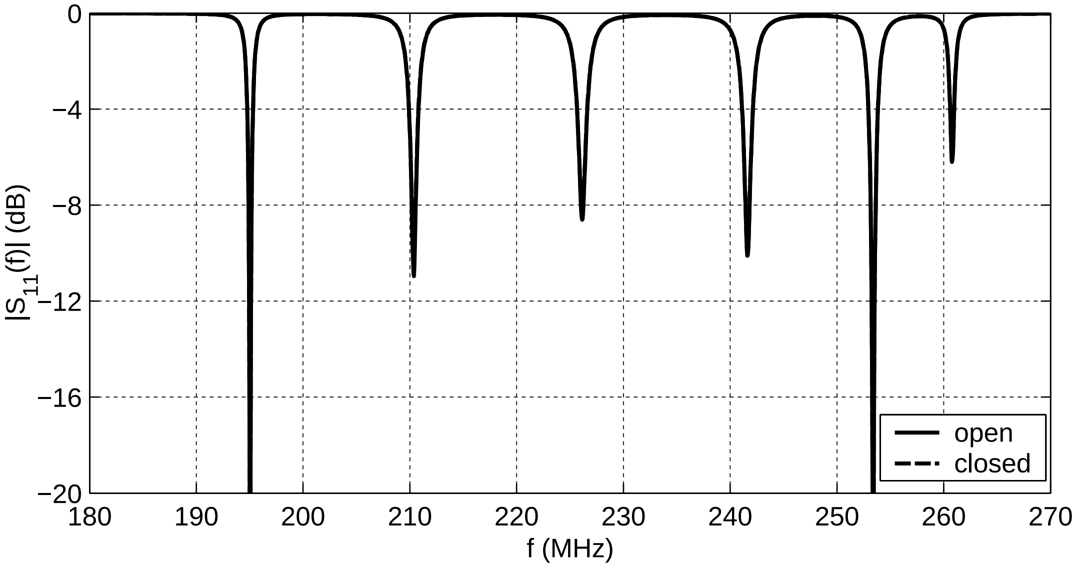

Figure 4-2: *Overall $S_{11}(f)$ response of closed vs. open from MTL tools.*

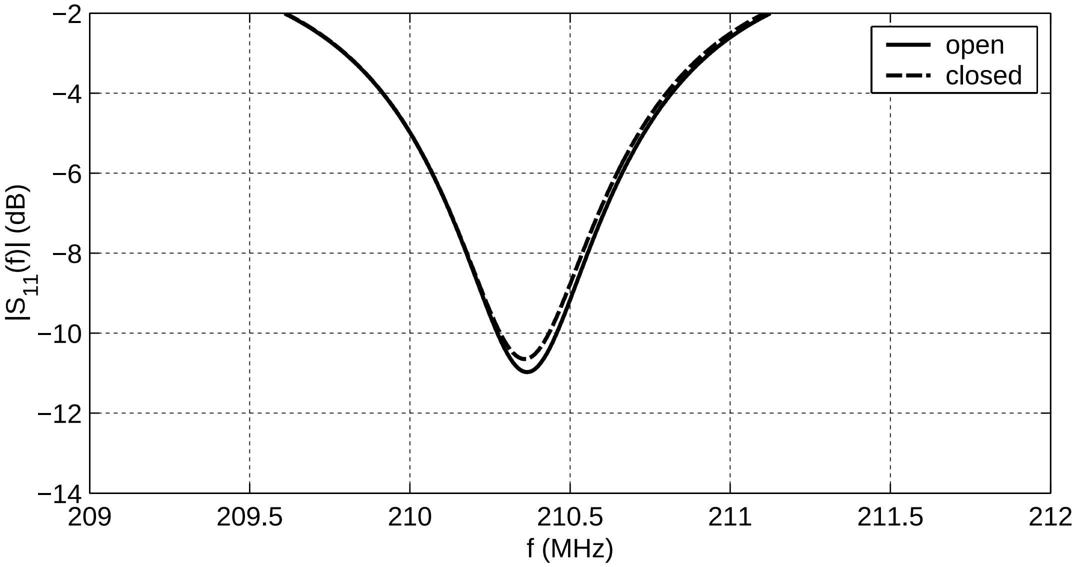

Figure 4-3: *Second mode of $S_{11}(f)$ response of closed vs. open from MTL tools.*

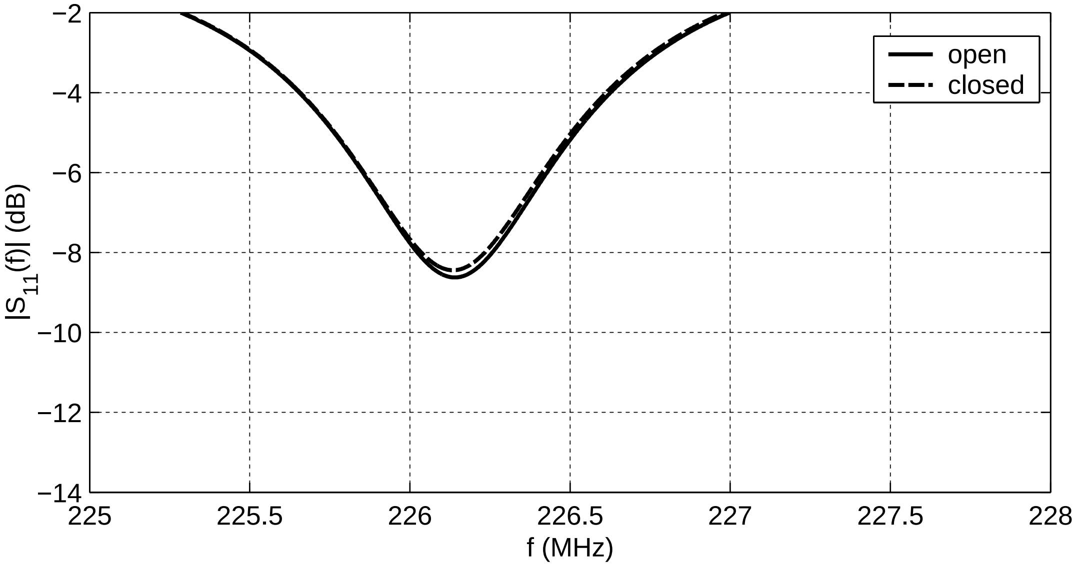

Figure 4-4: *Third mode of $S_{11}(f)$ response of closed vs. open from MTL tools.*

As seen from these plots, the MTL method predicts small variations in the $S_{11}(f)$ response during the glottal cycle. The most sensitive modes seen from the above graphs are modes 2 and 3. The magnitude changes and frequency shifts for mode 2 are: magnitude change = 0.586dB and frequency shift = 8kHz, while for mode 3: magnitude change = 0.292dB and frequency shift = 5kHz. The MTL tends to overestimate the quality factor of the resonances and underestimate losses since it cannot account for induced eddy-currents.

4.1.2 FEM simulation results

While the MTL is a computationally efficient method that can quickly approximate the behavior of the sensor, the FEM can be applied with a more anatomically accurate slice of the larynx. Figure 4-5 shows the dimensions and materials used in the FEM neck model based on the background section presented at the beginning of the thesis and a proportional analysis of a human's neck [37]. The model contains the most significant neck structures: the skin, the neck muscle, the cartilage around the trachea, the jugular veins, the spinal cord, and the vertebrae (see Figure 4-5).

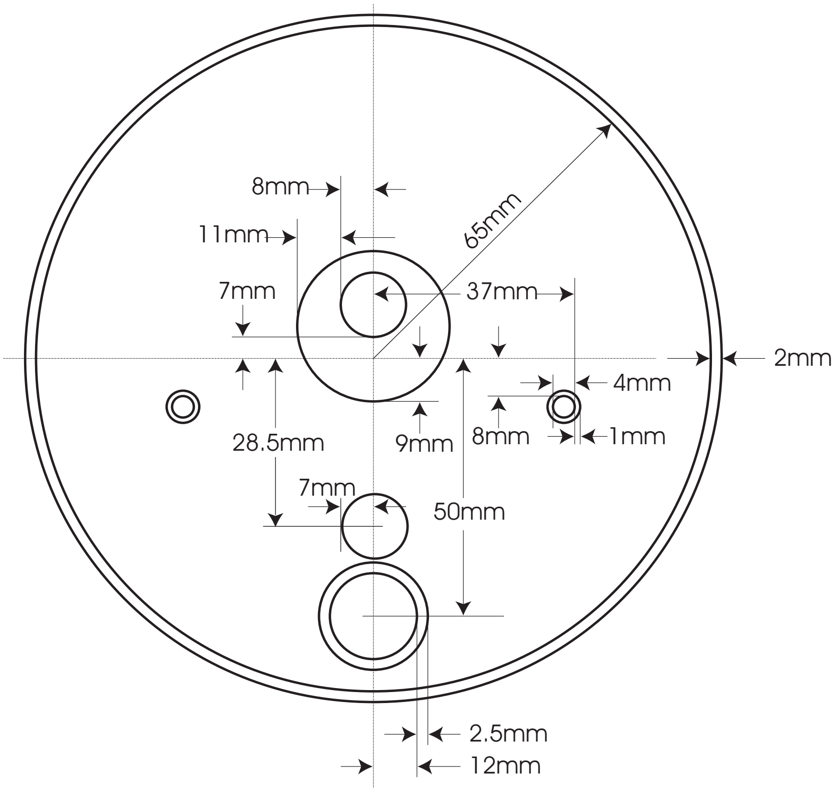

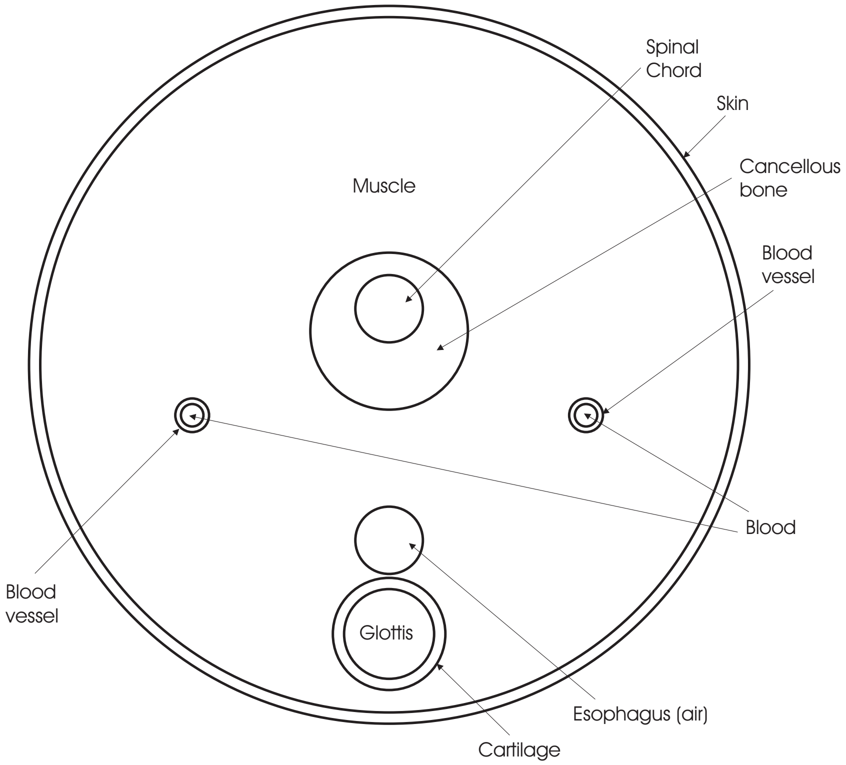

Figure 4-5: *Dimensions and materials of the FEM neck model. All structures shown above are cylinders with a height of 38.1mm [28].*

As done in the MTL case, the open and closed glottal states are modeled by alternating the material properties of the glottis cylinder from air (open glottis) to muscle (closed glottis). The dielectric properties of body tissues consistent with the location of the larynx at 200MHz are given in Table 4-2. Figure 4-6 shows the $S_{11}(f)$ response in the open and closed glottis states over the full simulation range, while Figure 4-7 and Figure 4-8 show detailed plots of the second and third resonant modes, respectively.

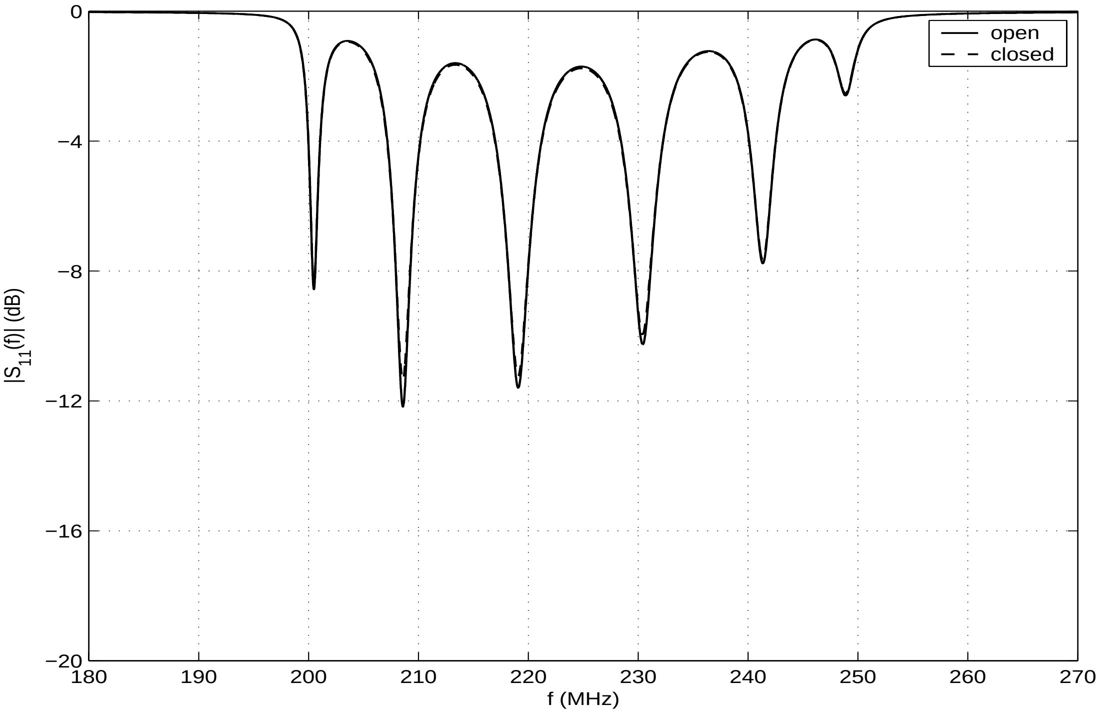

Figure 4-6: *Overall $S_{11}(f)$ response of closed vs. open from FEM tools.*

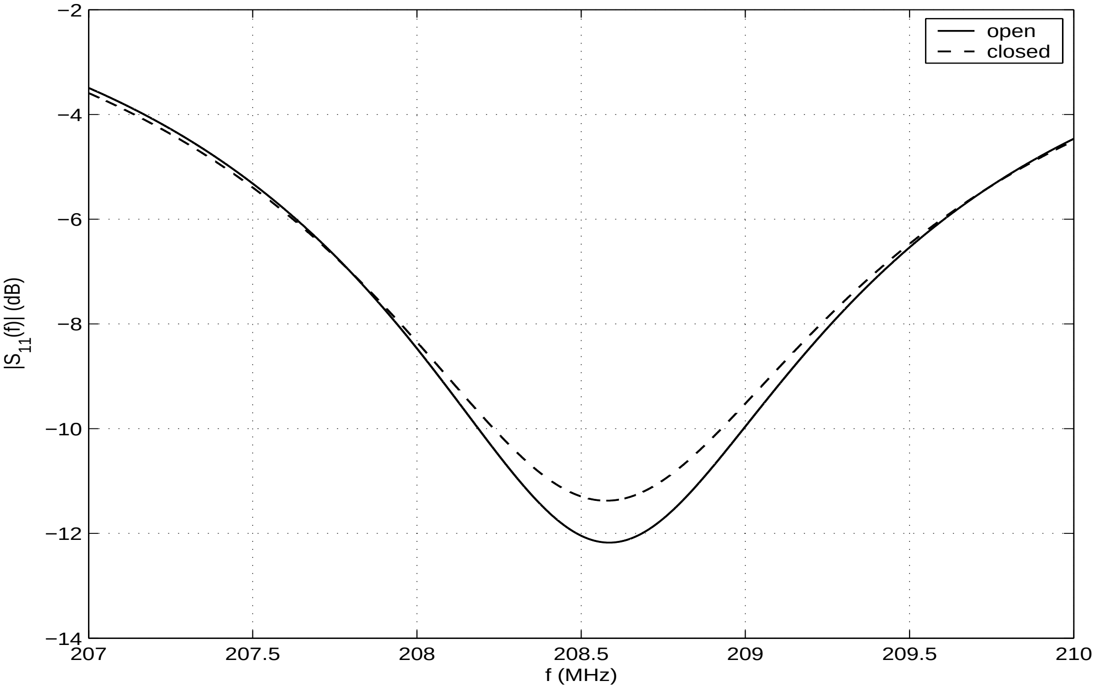

Figure 4-7: *Second mode of $S_{11}(f)$ response of closed vs. open from FEM tools.*

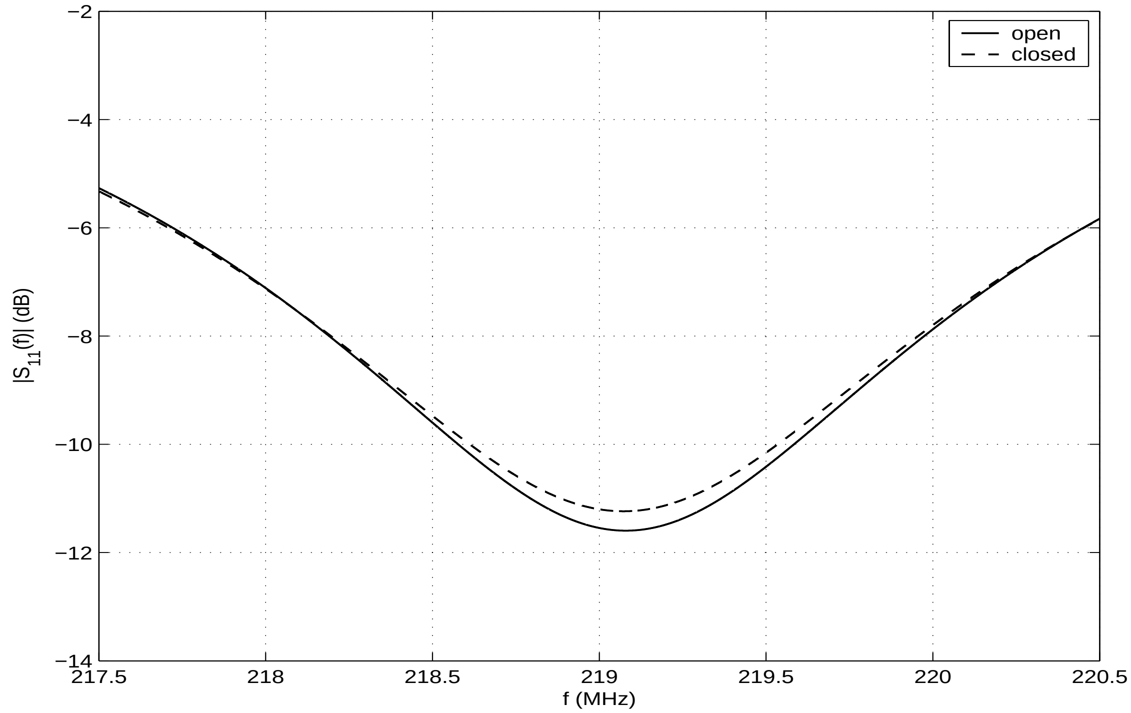

Figure 4-8: *Third mode of $S_{11}(f)$ response of closed vs. open from FEM tools.*

Similar to the MTL case, the FE tools predict a small perturbation in the S_{11} response during the glottal cycle. The relative change predicted from FE tools is comparable to the MTL results. For mode 2: magnitude change = 0.801dBc and frequency shift = 9.5kHz, while for mode 3: magnitude change = 0.358dBc and frequency shift = 6.5kHz. The change is slightly higher than in the MTL case due to the fact that the FEM can account for eddy-current losses, which play an important role in the sensitivity of this design.

A natural question may arise regarding the convergence of the FE simulations. The convergence issue can be addressed with HFSS by performing a single frequency adaptive solution. In applications where only the magnitude change in all s-parameters between two consecutive iterations is important, the ΔS_{ij} parameter can be used to quantify the solution convergence, where:

$$\Delta S_{ij} = \left| S_{ij}^{current} - S_{ij}^{previous} \right| \tag{54}$$

The iterative solver will continue to refine the mesh until either the number of iterations or the ΔS_{ij} value is met. In order to ensure conformance to the ΔS_{ij} parameter, the number of iterations can be set to a large value. On the other hand, ΔS_{ij} should not be set to a really small value, since such accuracy may not be achieved, and the solver will eventually run out of memory. For the six-element resonator the solution converged nicely after setting $\Delta S_{ij} = 0.02$. In general, the adaptive solution frequency is chosen at the higher end of a full frequency sweep, since this allows for the mesh to capture enough nodes per wavelength to ensure adequate coverage for the full frequency sweep. Although the six-element resonator has six radically different modes, the adaptive solution was conducted at the second resonant mode frequency.

The FE post-processing tools can also be utilized to generate detailed field plots in a region of interest. More intuition about the sensitivity of the six-element resonator in different modes can be gained by observing the electric field strength and the amount of field penetration into the glottal region. Figure 4-9 shows the electric field magnitudes in a cross-sectional plane of the neck for all resonant modes. The field magnitudes are plotted for the “open glottis” state only. Since the six-element resonator is an eddy current based sensor, the most sensitive modes will have greater electric field magnitudes in the glottal region. From these plots it can be deduced that that mode 2, which has the highest field strength in the glottal region, is the most sensitive mode. For mode 3, the field penetrates well in the glottal region, but it is not as strong in magnitude as mode 2. The E-field plots confirm the sensitivity results seen in the $S_{11}(f)$ plots, presented in the previous section. The sensitivity of this design can be improved by increasing the operating frequency, which increases $\omega\varepsilon$ and in turn eddy-current losses. Also, by decreasing the sensor size the fields can be more concentrated in the glottal area; however, too small a sensor may not provide enough penetration into the region of interest.

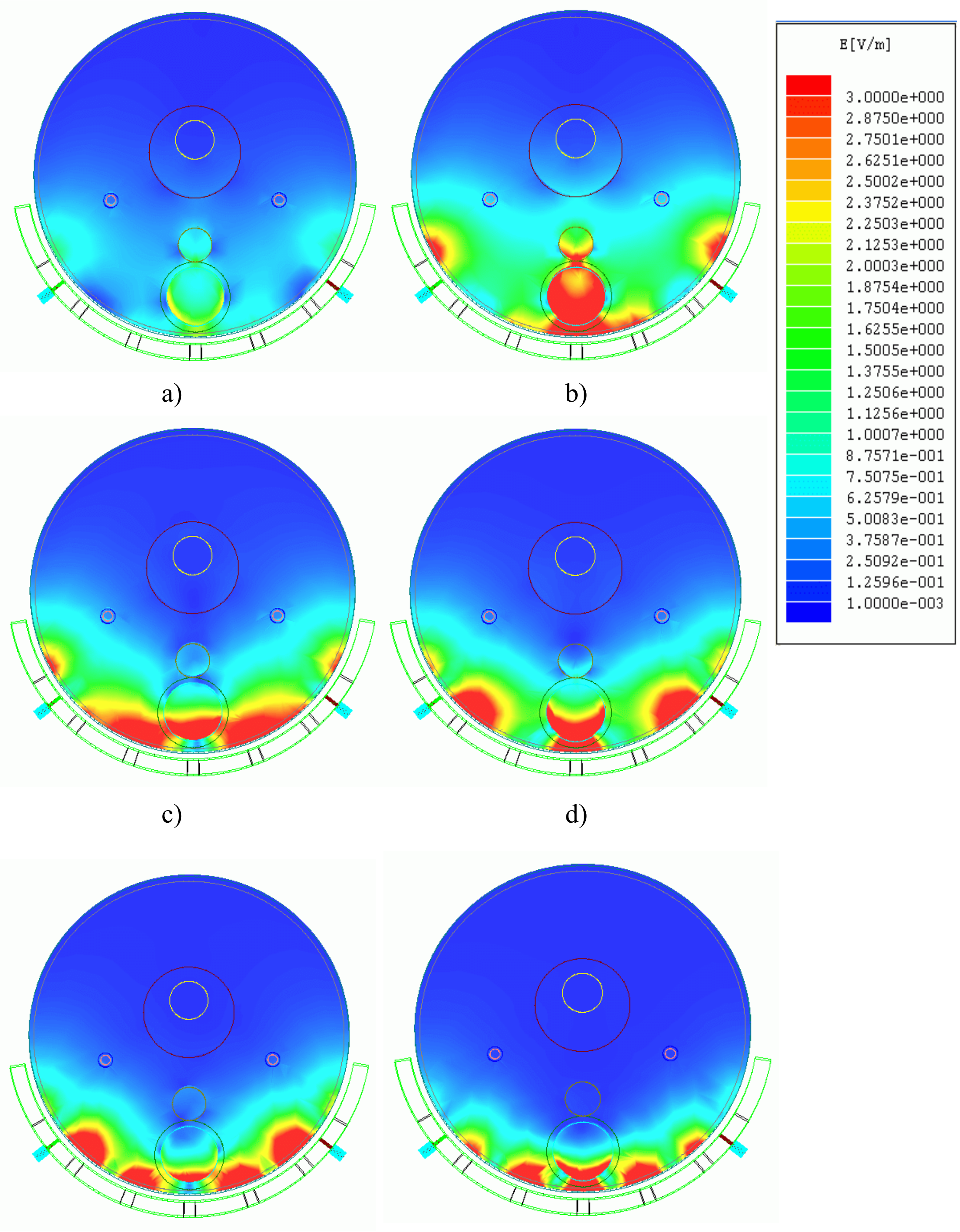

a)

b)

c)

d)

e)

f)

Figure 4-9: *Electric field plots for modes 1-6 in order are shown in a) through f).*

From the $S_{11}(f)$ response obtained through FE simulations it is apparent that the six-element resonator offers insignificant changes during the glottal cycle and cannot be implemented as an effective non-acoustic speech sensor. This is reinforced by the fact that the glottal cycle was captured by alternating an entire 38.1mm tall cylinder between neck muscle and air, which in reality is a gross approximation. While this was done as an initial proof-of-concept, a more elaborate vocal folds model must be used. A better approximation of the glottis size would be a cylinder of diameter 12mm and height of 5mm. This problem will be addressed with the parallel plate resonator by introducing a refinement to the biological model (Section 4.2.2).

As previously discussed, the six-element resonator is able to detect changes in eddy-current and conductive losses that occur during the glottal cycle. However, the aggregate effect of the small volumetric changes during the glottal cycle and the relatively small conductivity value of tissue (on the order of $0.3\frac{S}{m}$) prevents large changes in the S_{11} response. Given the time constraint of the project, an alternate sensor design, composed of two copper plates that encompass the glottal area, was investigated, instead of trying to optimize the six-element sensor. FE simulations are presented next for the parallel plate sensor.

4.2 Parallel plate resonator predictions

Initial FE simulations utilized the same biological load as shown in Figure 4-5. In addition, since the new resonator operates at a lower frequency (around 50MHz) the properties of all body tissues will be modified accordingly (see Table 4-3).

Table 4-3: Dielectric properties of relevant tissues at 50MHz [6].

Body Tissue	**Relative Permittivity**	**Conductivity**
Skin	107.17	0.40533
Muscle	77.063	0.67808
Cartilage	68.457	0.44052
Blood	94.205	1.1926
Blood vessel	74.351	0.41161
Cancellous bone	33.258	0.15505
Spinal cord	60.842	0.29877

The geometry of the parallel-plate resonator as shown in Figure 3-4 is summarized in Table 4-4.

Table 4-4: Parallel-plate speech sensor prototype design parameters.

Parameter	**Value**
Angle encompassed by lexan former	168.75°
Lexan former outer radius	69 mm
Lexan former inner radius	67 mm
Lexan former height	38.1mm
Lexan former thickness	2mm
Number of copper plates	2
Angle encompassed by each plate	45°
Angle spacing between plates	30°
Inductance value	500nH

4.2.1 FEM predictions

FE simulations were carried for the new sensor design (shown in Figure 3-4) with the aforementioned load model. The full-frequency range of the sweep in both cases is 20-70MHz. The simulation results for the entire frequency range (Figure 4-10) and a close-up view of the resonant mode (Figure 4-11) are presented below.

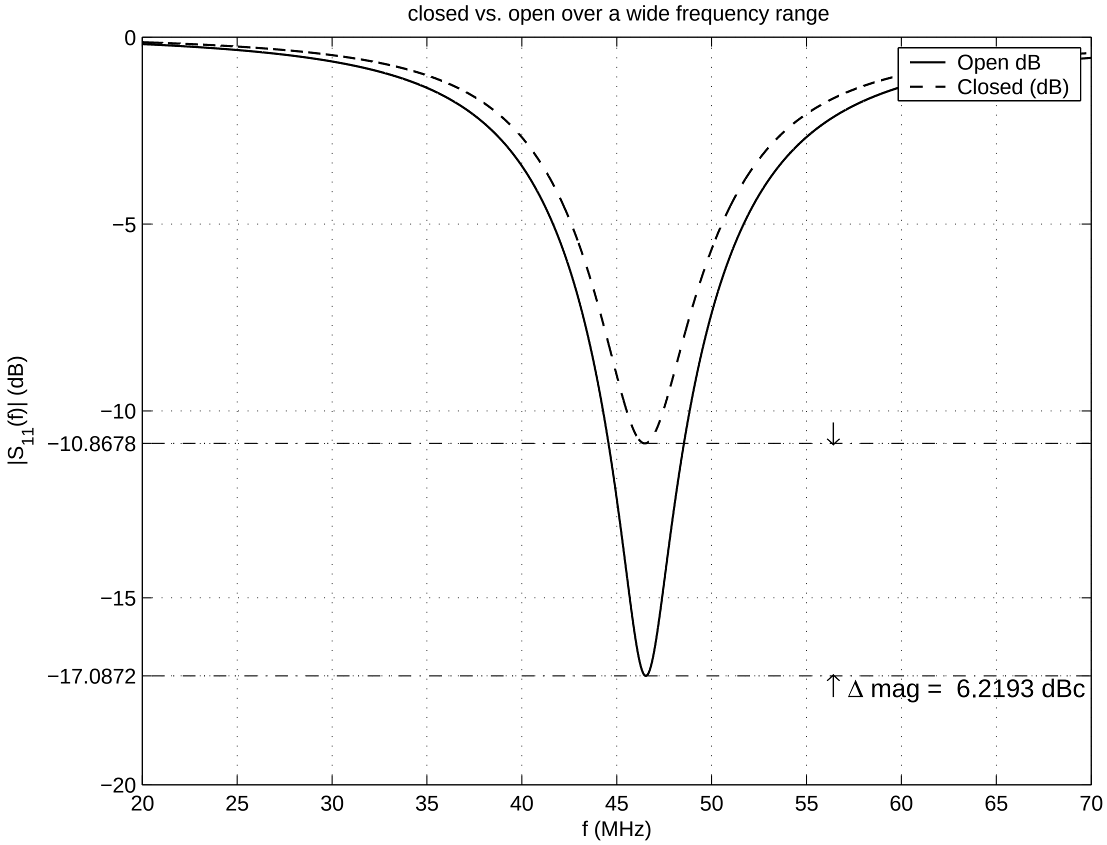

Figure 4-10: *Overall $S_{11}(f)$ response of closed vs. open for the PPRES from FEM tools, using the biological load of* Figure 4-5.

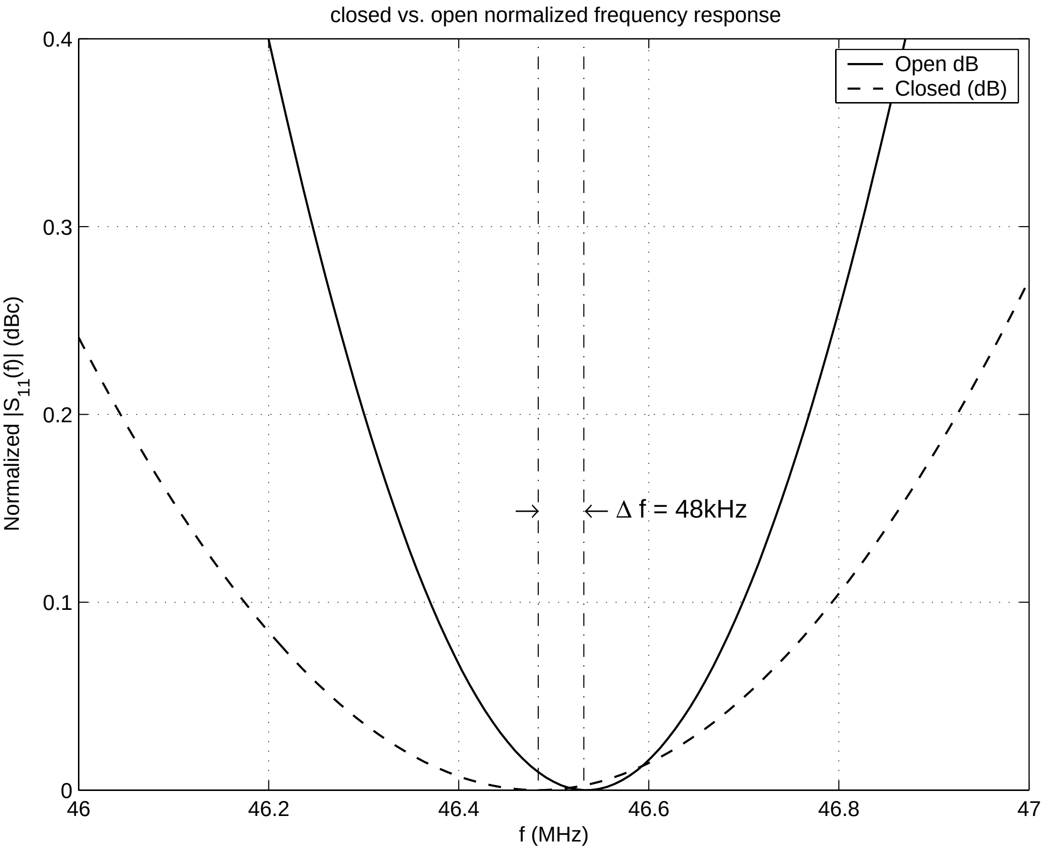

Figure 4-11: *Zoomed-in $S_{11}(f)$ response of closed vs. open for the PPRES from FEM tools, using the biological load of* Figure 4-5.

Contrary to the six-element resonator, the new sensor design offers improved sensitivity to changes during the glottal cycle. While utilizing the same load model the parallel plate resonator experiences about 6dBc magnitude change during the glottal cycle, depicting the stark contrast between the two designs. Note also that the new sensor is not very well matched at resonance. To move in the direction of a more realistic design two issues must be addressed:

1. Improve the biological load to include a realistic glottis size.
2. Improve matching at resonance via matching caps (as shown in Figure 3-6).

4.2.2 Load and resonator refinements

The biological load model of Figure 4-5 was refined in order to more realistically represent glottal changes. The only difference in the modified biological load model is the size of the glottis. The initial glottis cylinder, diameter of 12mm and height of 38.1mm, is now an air cylinder representing the larynx. However, at the midpoint of the larynx a 12mm diameter 5mm tall cylinder is introduced. This cylinder is used to capture changes during the glottal cycle: for the “closed-glottis” state the cylinder has the properties of muscle, while for the “open-glottis” state the cylinder has the properties of air. The laryngeal structure with the embedded folds is shown in Figure 4-12.

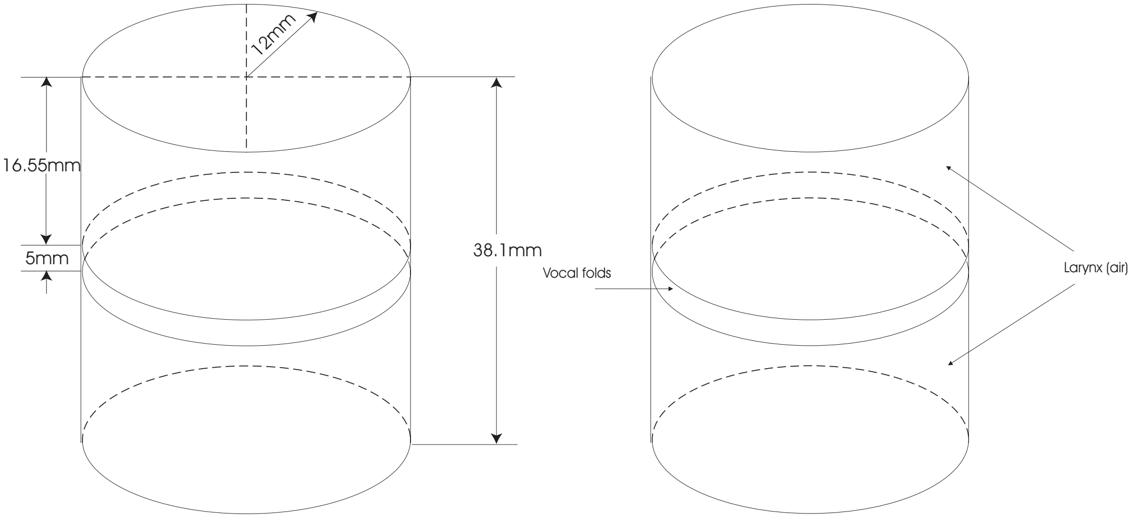

Figure 4-12: *Modifications to the laryngeal structures. The vocal folds are replaced with a 5mm tall cylinder.*

In addition to load refinements, the resonator was modified as to reflect the changes depicted in Figure 3-6. In order to match the resonator at the desired frequency of 50MHz for the “closed glottis” case, the simulations were carried with the biological load that includes the refinements of Figure 4-12 with the inductors shorted and the matching capacitor left open. The input impedance of the resonating structure was calculated with the available HFSS tools; the impedance value at 50MHz was found to be (19.95 – j174.45)Ω. A matching program was utilized to determine the lumped impedance values for an L-type configuration: the inductance value was found to be 633.23nH, while the matching capacitance value to be approximately 78.13pF. The four possible types of L-matching networks are shown in Figure 4-13.

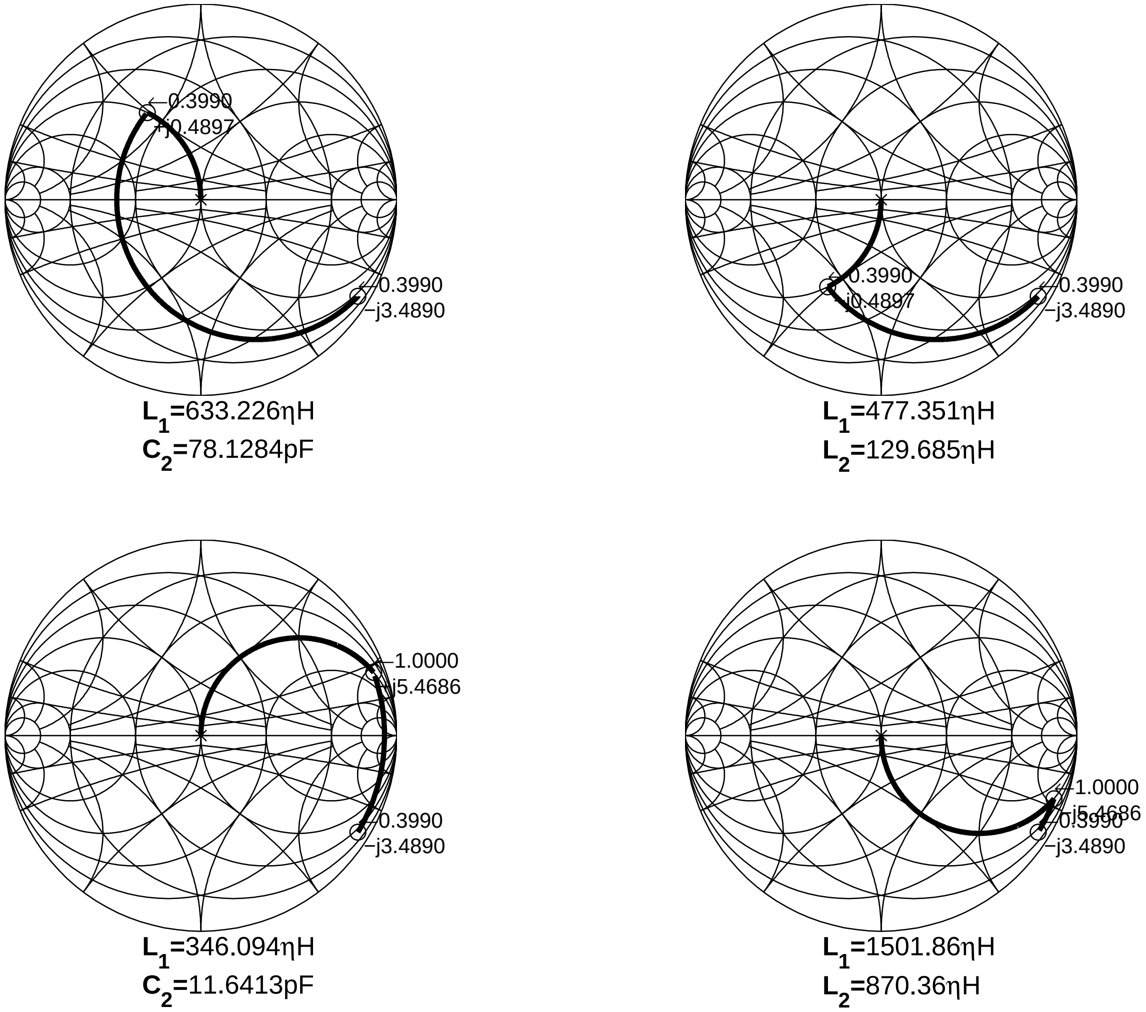

L_1=633.226ηH
C_2=78.1284pF

L_1=477.351ηH
L_2=129.685ηH

L_1=346.094ηH
C_2=11.6413pF

L_1=1501.86ηH
L_2=870.36ηH

Figure 4-13: *Matching networks for the parallel plate resonator at 50MHz.*

The first type of network was chosen because it provides reasonable inductance values, commercially available with a relatively high Q.

4.2.3 Pspice simulations

Prior to conducting simulations with the FE solver, a lumped representation of the sensor, the load and the tuning circuit was devised with Pspice. The model includes the finite Q models for the tunable inductors (Q=162) and the trimmer capacitor (Q=1000). The glottal cycle is captured by changing the value of the neck capacitance from 18.25pF (open glottis) to 18.75 (closed glottis), which is a conceivable difference.

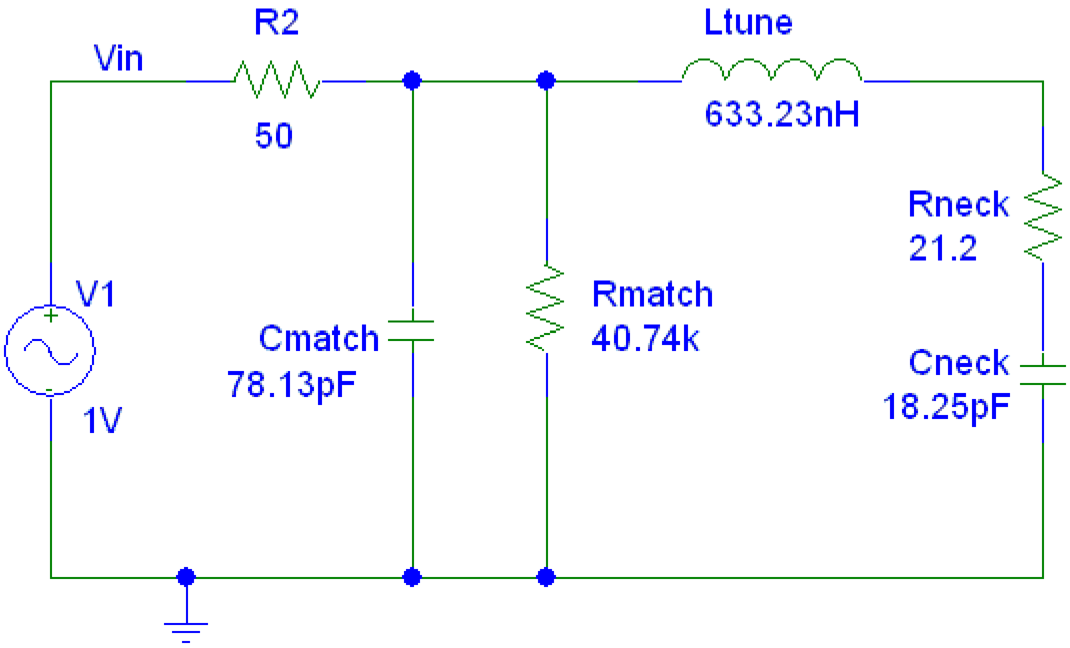

Figure 4-14: *Simulation model with Pspice.*

The input reflection coefficient of the circuit was computed and plotted over the 20-70MHz range, where the input reflection coefficient is given by:

$$S_{11}(f) = 20\log_{10}\left(1 - 2R_2 \frac{i_{R2}}{V_{in}}\right) \tag{55}$$

The simulation results for the entire frequency range (Figure 4-15) and a close-up view of the resonant mode (Figure 4-16) are presented below.

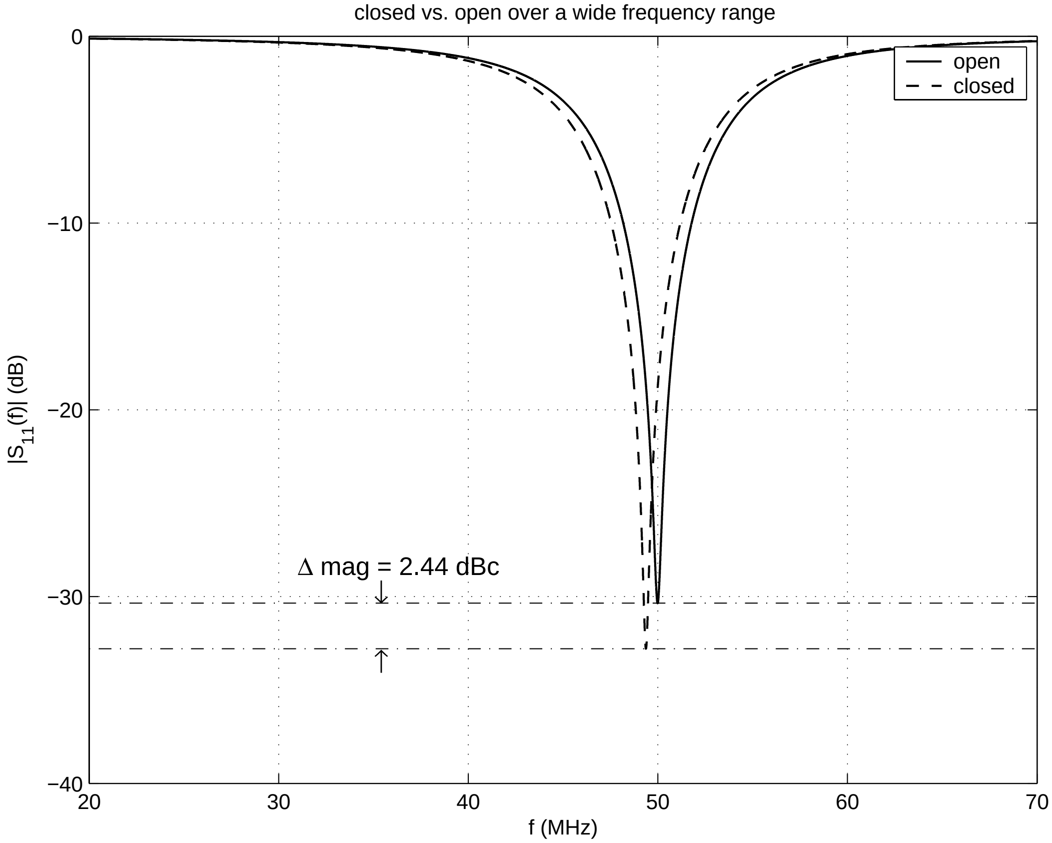

Figure 4-15: *Overall $S_{11}(f)$ response of closed vs. open for the PPRES from Pspice, using the matching circuit of* Figure 4-13.

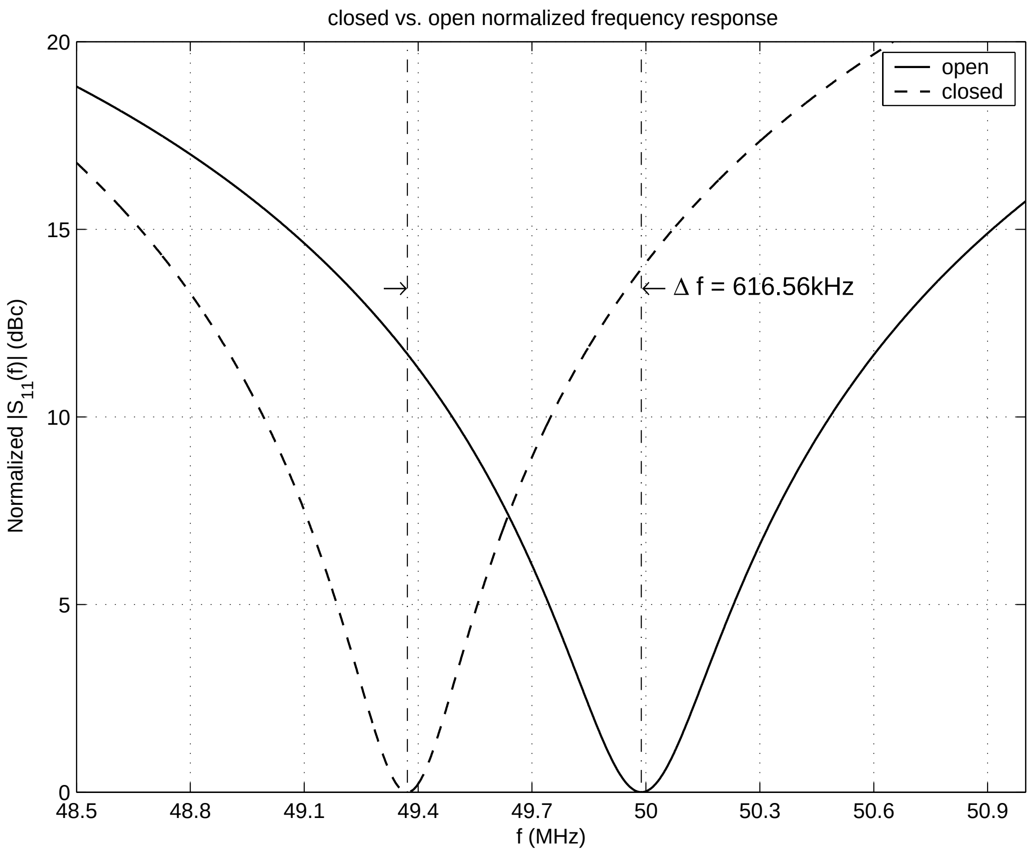

Figure 4-16: *Zoomed-in $S_{11}(f)$ response of closed vs. open for the PPRES from Pspice, using the matching circuit of* Figure 4-13.

The Pspice lumped impedance model predicts a 2.44dBc relative difference in the resonance depth and a 616.56kHz frequency shift during the glottal cycle. Regardless of the small, 0.5pF, relative capacitance change, the low operating frequency causes large shifts in the sensor response. Since the lumped model does not account for wave propagation and fringing effects, these results are next compared to what the FEM predicts.

4.2.4 FEM predictions

The balanced design in the FEM model is formulated via splitting the total inductance into two values of 316.613nH, connected to the beginning of each plate. A snapshot of the HFSS model is shown in Figure 4-17.

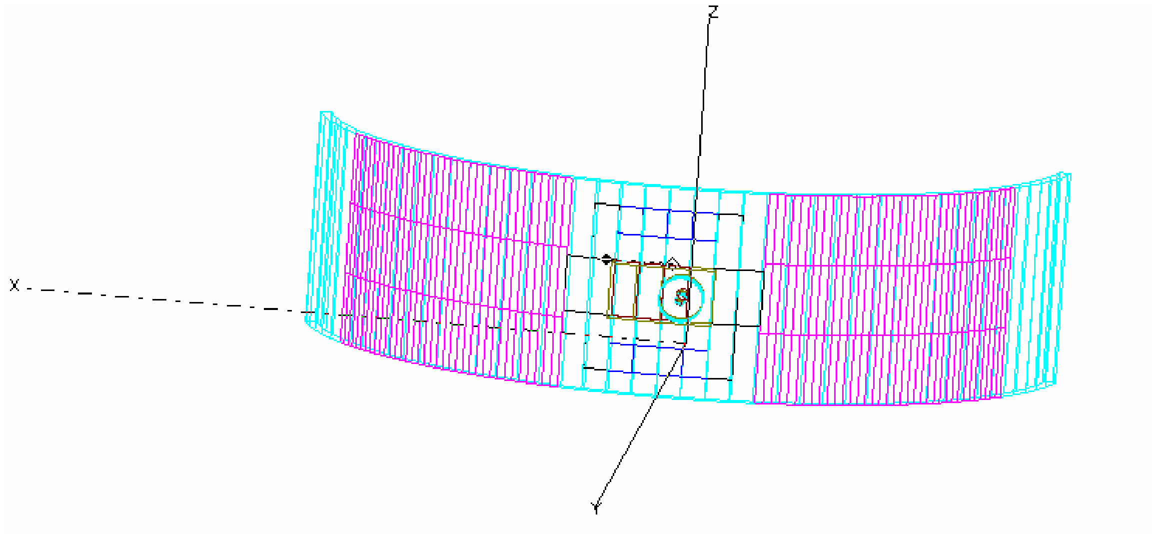

Figure 4-17: *Snapshot of the resonator model in HFSS 8.5.*

Simulations were run with the matching network of Figure 4-13, but the match was unsatisfactory: at resonance the return loss was only –14dB with an input impedance of (38.2 – j27.9)Ω. This was due to parasitics and other non-idealities associated with the modeling of the resonator. In fact, the previously computed impedance, with shorted inductors and open capacitors, appears at the input of an SMA connector, where the source is set. On the other hand, the tuning inductors and the matching capacitor appear beyond this point.

The impedance matching at the input can be improved by reducing the value of the matching capacitor. After a few iterations, the matching capacitor value was computed to be 46pF, while the tuning inductance stayed the same. Since this is not an exact method, a better approach would be to utilize an optimization program (Ansoft offers this separate from HFSS). In reality, the matching capacitance will need to vary from person to person, so a "rough estimate" is acceptable when carrying out these simulations. Figure 4-18 shows the S_{11} response over the full simulation range, while Figure 4-19 provides a zoomed in view of the resonant mode. As in the case of the six-element resonator, the convergence parameter for the adaptive solution case was set as $\Delta S_{ij} = 0.02$ prior to conducting the full-range sweeps.

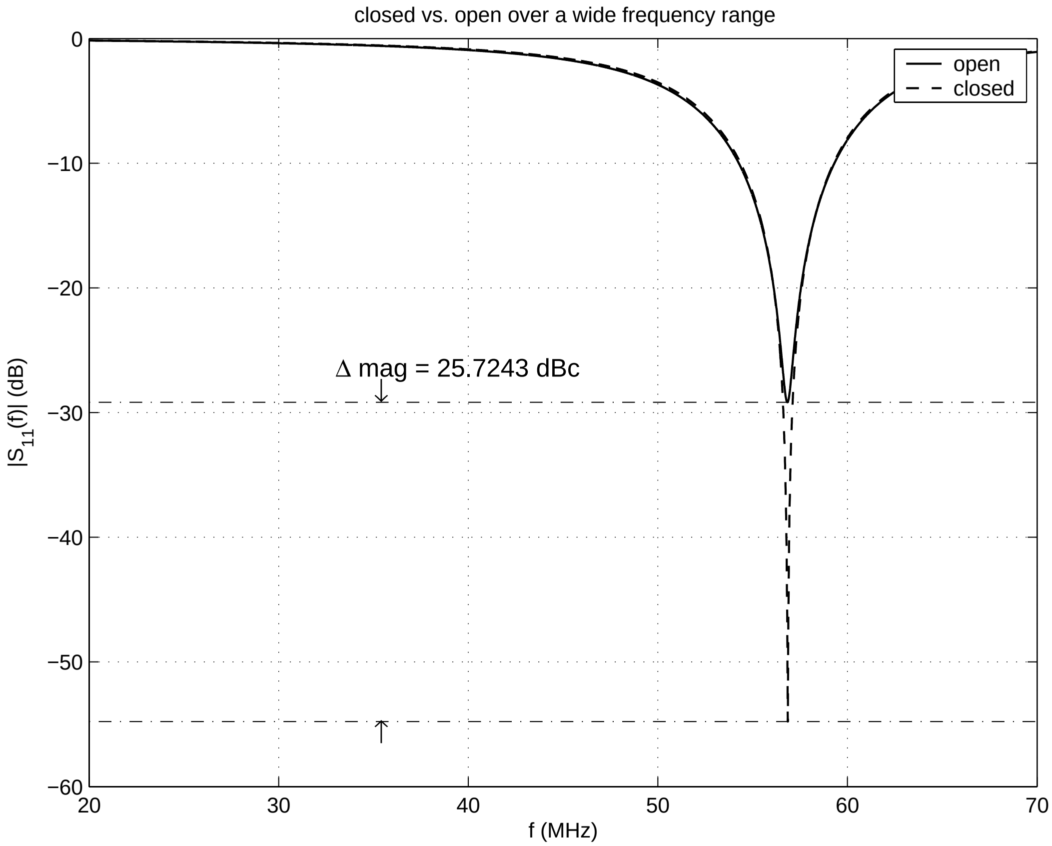

Figure 4-18: *Overall $S_{11}(f)$ response of closed vs. open for the balanced well-tuned PPRES from FEM tools using the refinement of* Figure 4-12.

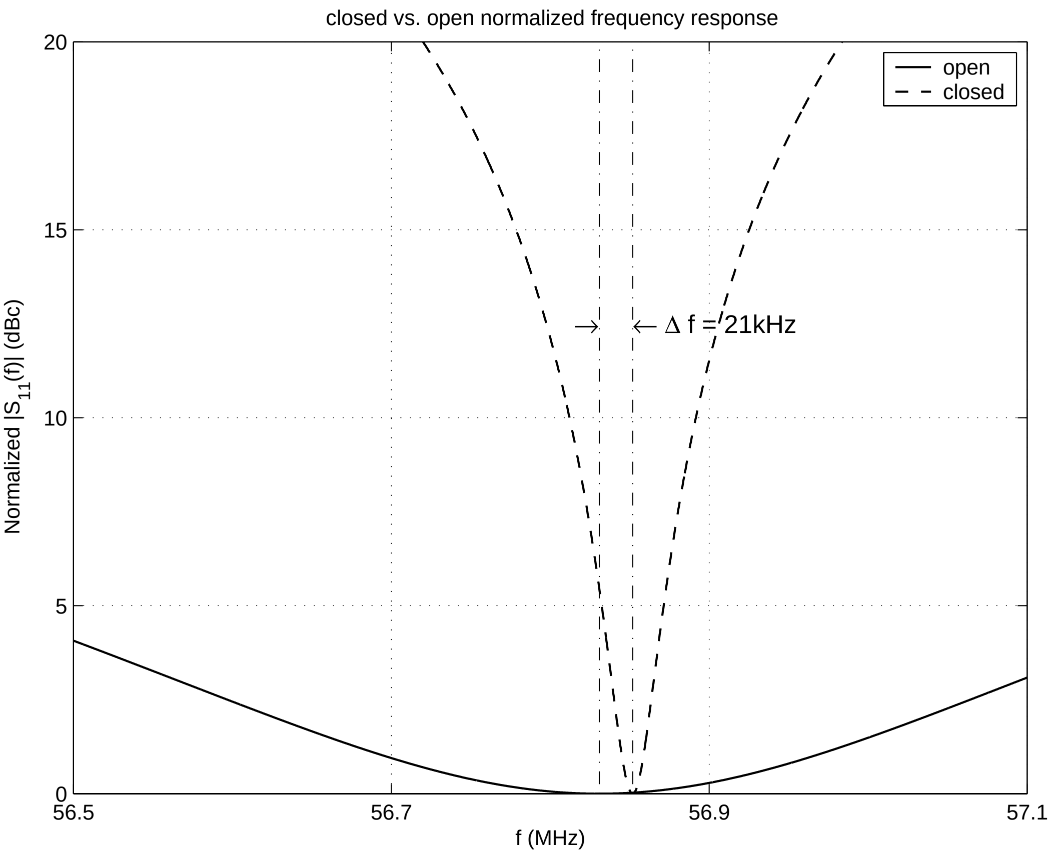

Figure 4-19: *Zoomed-in $S_{11}(f)$ response of closed vs. open for the balanced well-tuned PPRES from FEM tools using the refinement of* Figure 4-12.

Unlike the results presented in Sections 4.2.1 and 4.2.3 the new design offers significant improvements in matching. The magnitude sensitivity has greatly improved to around 25.7dBc, due to better matching, however the frequency shift has been reduced due to refinements in the load (i.e. less capacitive change). The relative change of 25.7dBc may seem extremely optimistic, but we must keep in mind that the presented results account for a fully closed versus a fully open glottis, which never occurs during normal speech. The glottal cycle can be better captured by either decreasing the size of the glottis cylinder, or even introducing an ellipsoidal shaped glottis. Further refinement of the biological model was not pursued, since the purpose of these simulations is not to exactly predict the quantitative behavior of the sensor, but to gain a better understanding of its qualitative behavior. In either case, the work had to progress in the direction of a practical implementation, and both FEM and the Pspice results provided confidence that the sensor would in fact provide a signal proportional to the glottal flow waveform during voiced segments of speech.

4.2.5 Field distribution inside the load

As in the case of the six-element resonator, using the available FE post-processing tools we can obtain detailed field plots that show the amount of electric-field penetration into the glottal area and provide some intuition about the sensitivity of the parallel-plate resonator. The magnitude of the electric field is shown for the single resonant mode of the parallel plate sensor for the case when the load is in the "open glottis" state. As it can be seen from the field plot the magnitude of the electric field in the glottal region is comparable to the case of the six-element resonator, despite being driven at ten times less the input RF power (-10dBm). More importantly the plot shows that there is a nonzero electric field gradient through the glottal area in the x-direction, which is an indication of capacitive coupling between the copper plates.

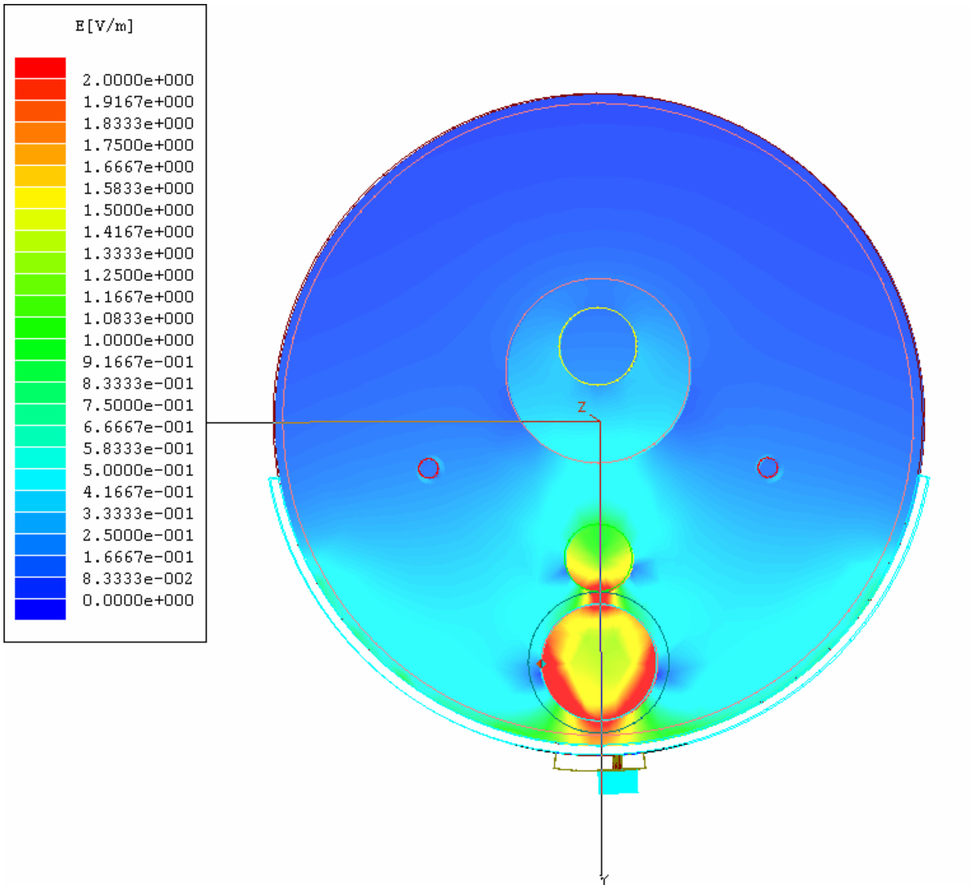

Figure 4-20: *Electric field plot for the balanced, well-matched PPRES.*

From the s-parameter and field plot results, the parallel-plate resonator is expected to offer adequate sensitivity to changes during the glottal cycle. Before implementing such resonator as a speech sensor, conformance to FCC guidelines must be considered.

4.3 Field strength issues

The Federal Communications Commission (FCC) provides strict guidelines for permissible field strengths and power density of the electromagnetic waves that human subjects can be exposed to. With the new design showing promising results from the FE simulations standpoint, the first step in doing any tests on human subjects is to conform to these guidelines. A summary of the guidelines is reported in Table 4-5.

Table 4-5: FCC Limits for Maximum Permissible Exposure (MPE) [38].

(A) Limits for Occupational/Controlled Exposure[2]

Frequency Range (MHz)	Electric Field Strength (E) (V/m)	Magnetic Field Strength (H) (A/m)	Power Density (S) (mW/cm^2)	Averaging Time $\lvert E \rvert^2$, $\lvert H \rvert^2$ or S (minutes)
0.3-3.0	614	1.63	(100)*	6
3.0-30	1842/f	4.89/f	($900/f^2$)*	6
30-300	61.4	0.163	1.0	6
300-1500	--	--	f/300	6
1500-100,000	--	--	5	6

(B) Limits for General Population/Uncontrolled Exposure[3]

Frequency Range (MHz)	Electric Field Strength (E) (V/m)	Magnetic Field Strength (H) (A/m)	Power Density (S) (mW/cm^2)	Averaging Time $\lvert E \rvert^2$, $\lvert H \rvert^2$ or S (minutes)
0.3-1.34	614	1.63	(100)*	30
1.34-30	824/f	2.19/f	($180/f^2$)*	30
30-300	27.5	0.073	0.2	30
300-1500	--	--	F/1500	30
1500-100,000	--	--	1.0	30

f = frequency in MHz *Plane-wave equivalent power density

---

[2] Occupational/controlled limits apply in situations in which persons are exposed as a consequence of their employment provided those persons are fully aware of the potential for exposure and can exercise control over their exposure. Limits for occupational/controlled exposure also apply in situations when an individual is transient through a location where occupational/controlled limits apply provided he or she is made aware of the potential for exposure.

[3] General population/uncontrolled exposures apply in situations in which the general public may be exposed, or in which persons that are exposed as a consequence of their employment may not be fully aware of the potential for exposure or cannot exercise control over their exposure.

The FE post-processor provides the necessary tools to calculate and plot the field strengths inside the biological load. The field strengths will exhibit maximum value at resonance since most of the RF power delivered stays in the load. Field strength data is obtained in the xy-plane through two lines that pass through the center of the glottis: one in the x-direction and another in the y-direction. Along these lines the following field strength plots for the six-element resonator were obtained while driving the resonator with 0dBm (1mW) RF input power.

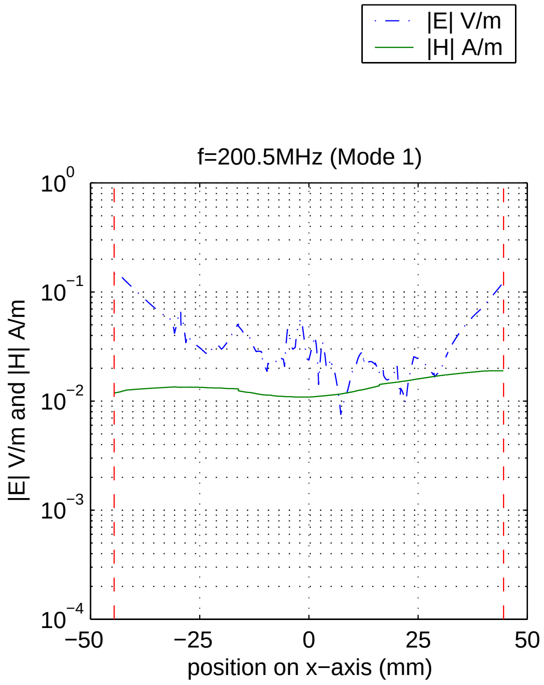

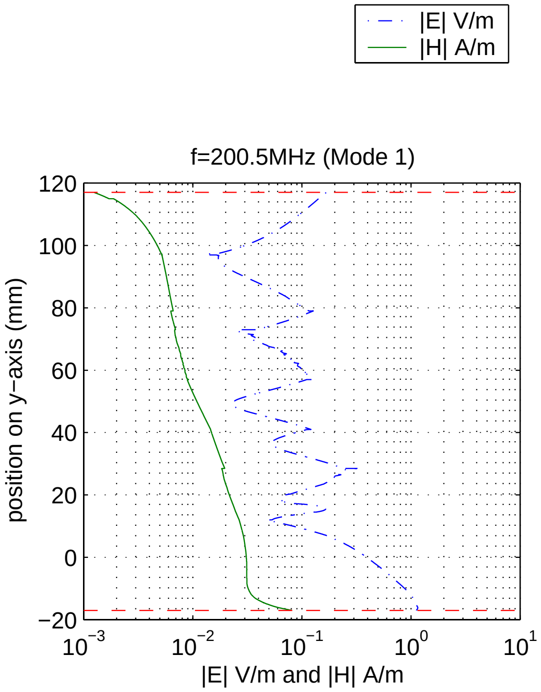

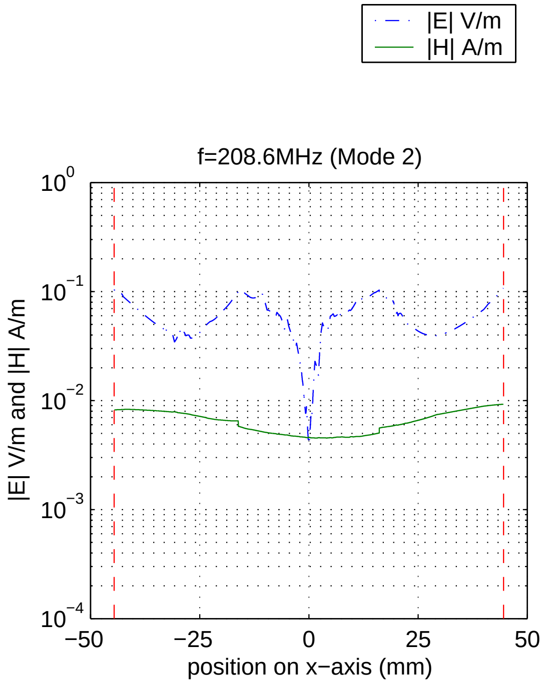
|E| V/m
|H| A/m
f=208.6MHz (Mode 2)
|E| V/m and |H| A/m
10^0
10^−1
10^−2
10^−3
10^−4
−50
−25
0
25
50
position on x−axis (mm)

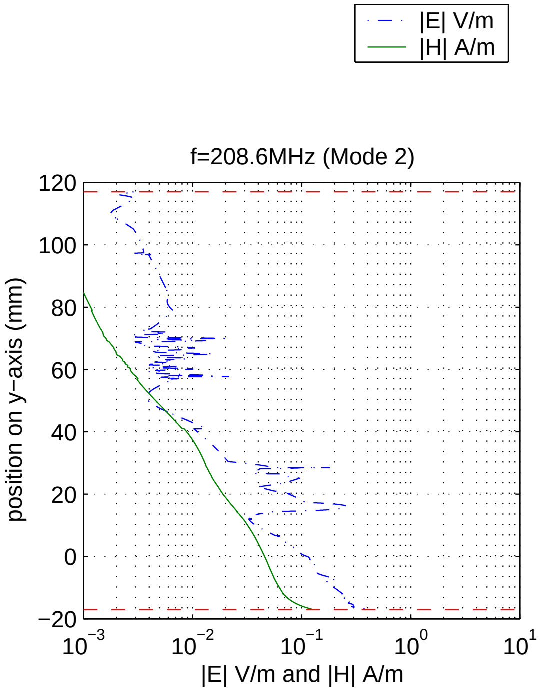
|E| V/m
|H| A/m
f=208.6MHz (Mode 2)
position on y−axis (mm)
120
100
80
60
40
20
0
−20
10^−3
10^−2
10^−1
10^0
10^1
|E| V/m and |H| A/m

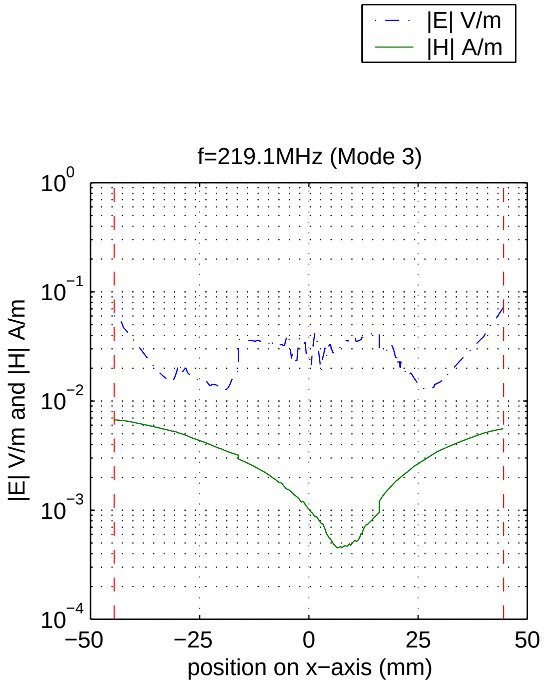
|E| V/m
|H| A/m
f=219.1MHz (Mode 3)
|E| V/m and |H| A/m
10^0
10^−1
10^−2
10^−3
10^−4
−50
−25
0
25
50
position on x−axis (mm)

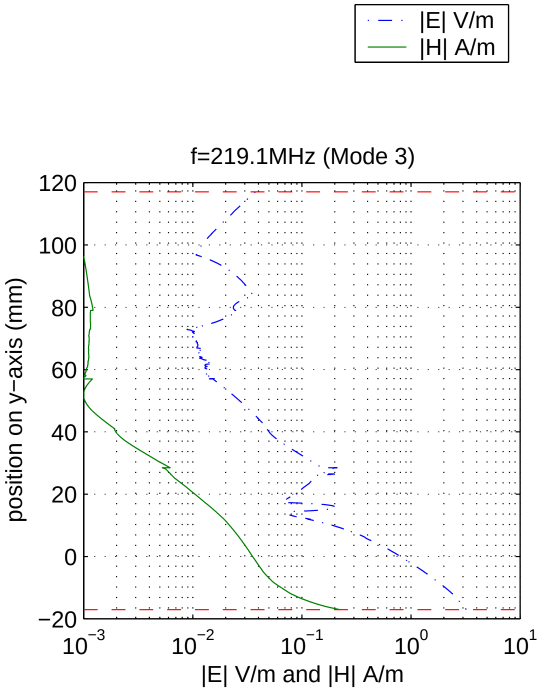
|E| V/m
|H| A/m
f=219.1MHz (Mode 3)
position on y−axis (mm)
120
100
80
60
40
20
0
−20
10^−3
10^−2
10^−1
10^0
10^1
|E| V/m and |H| A/m

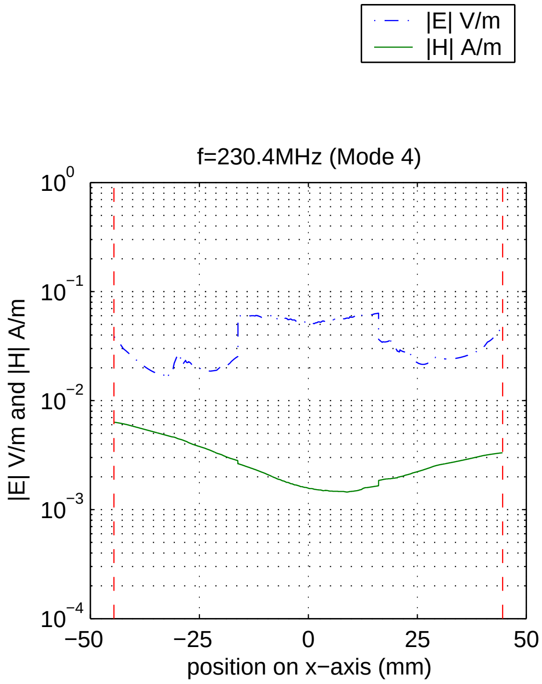
f=230.4MHz (Mode 4)

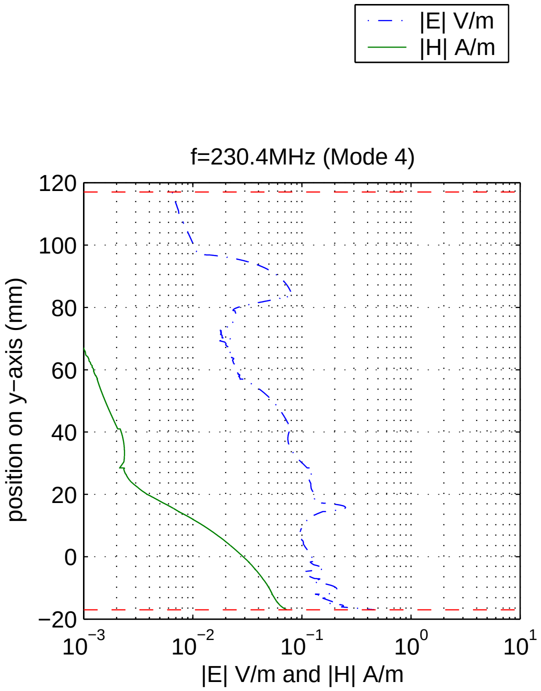
f=230.4MHz (Mode 4)

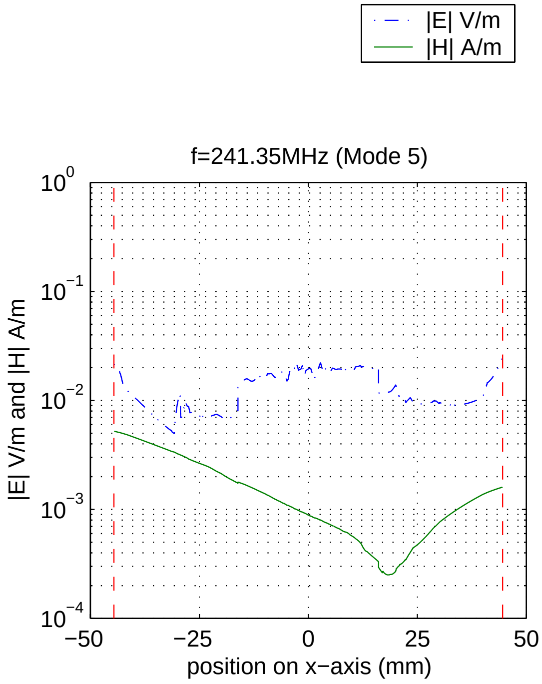
f=241.35MHz (Mode 5)

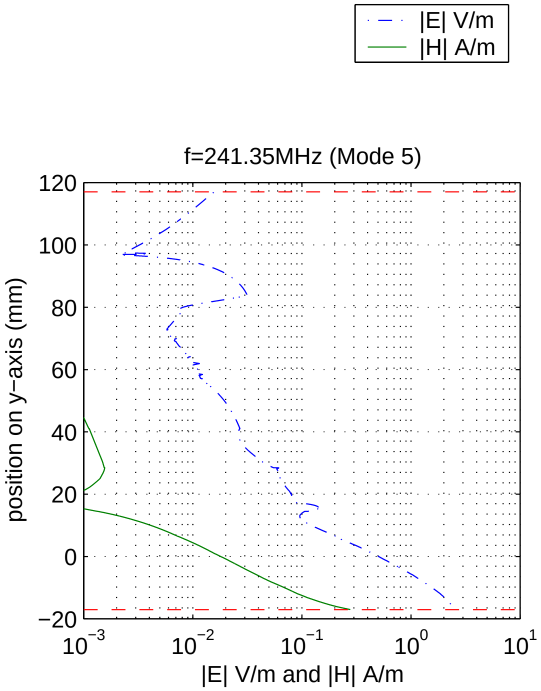
f=241.35MHz (Mode 5)

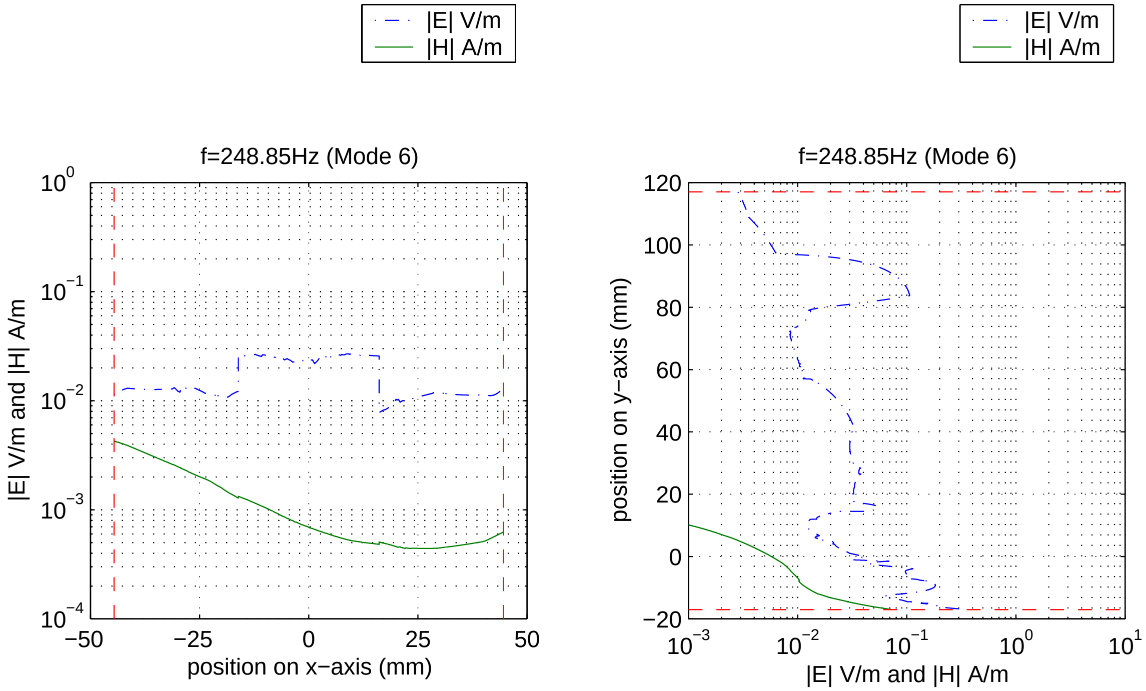

Figure 4-21: *Electric field and magnetic field strengths for the six-element resonator for all resonant modes.*

In the above plots the glottis is positioned at the (0,0) point. For the x-directed plots the neck extends approximately 44.6mm on each side of the glottis and for the y-directed plots the neck begins at –17mm (the front) and ends at 117mm (the back). The dashed red lines are drawn for convenience to indicate the beginning and end of the neck model in each direction. Data that is pertinent only to the field strength in the biological load is plotted. We can see that the six-element resonator fails to meet FCC requirements while being driven at the initially intended 0dBm RF input power, specifically surpassing the permissible magnetic field strength when driven in modes 3 and 5.

For the parallel plate resonator the input power is –10dBm (100µW) and the same field strength plots are repeated.

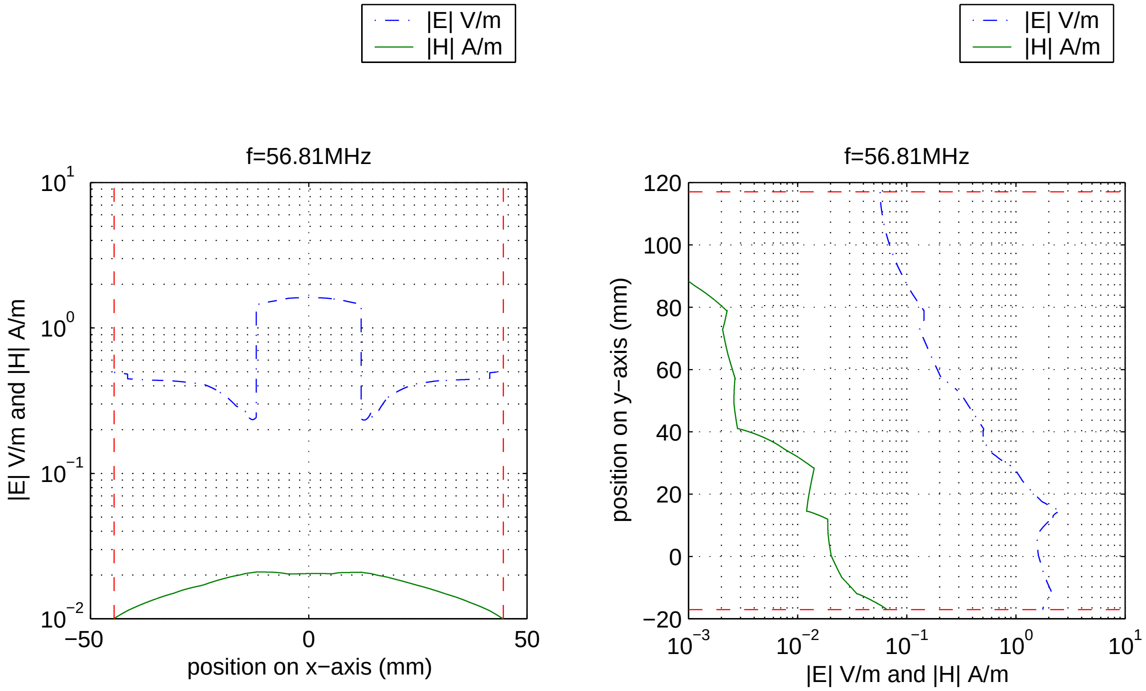

Figure 4-22: *Electric and magnetic field strengths for the parallel-plate resonator.*

The maximum safe power level can be computed by using the above graphs and the proportionality relationship: $|Field\ Strength| \sim \sqrt{P_{in}}$. To account for inaccuracies in the model and discretization errors, a 50% margin of error (with regard to field strengths) is introduced. For the six-element resonator, the calculations are based off the worst-case mode (mode 5). Results are summarized in Table 4-6.

Table 4-6: Maximum safe power level.

Type of Exposure	Maximum Allowed		Safe Input Power	
	Electric Field Strength (V/m)	Magnetic Field Strength (A/m)	Parallel Plate Resonator (μW)	Six-element Resonator (μW)
Controlled	61.4	0.163	184.51	106.3
Uncontrolled	27.5	0.073	37	21.32

5 Practical Implementation and Test Results

This section presents experimental results obtained with the six-element resonator, as well as preliminary human subject testing with the parallel plate resonator.

5.1 Six-element resonator

Non-biological tests were conducted with a physical prototype of the six-element resonator, which was constructed to the parameters of Table 4-1.

5.1.1 Construction procedure

The physical prototype was constructed on a cast acrylic (plexiglass) cylinder, having an outer diameter of 76.2mm, inner diameter of 69.8mm and a height of 38.1mm. Adhesive-backed copper tape portions, cut to the appropriate sizes, formed the microstrip lines and the ground shield. A standard, flange-type, SMA connector was mounted to the plexiglass former via nylon screws, and the body of the SMA connector was soldered directly to the endmost part of the ground shield. A small bore was drilled through the plexiglass former so as to allow for the center conductor of the SMA to connect to the endmost inner strip via a series tuning capacitor (0.5-8pF). The series capacitor was utilized to accommodate for matching to the 50Ω characteristic impedance of the coaxial cable. The terminating capacitance was formed by placing four 27pF surface-mount capacitors in a parallel configuration both on the bottom and top edges of the plexiglass former. The realized six-element structure is shown in Figure 5-1.

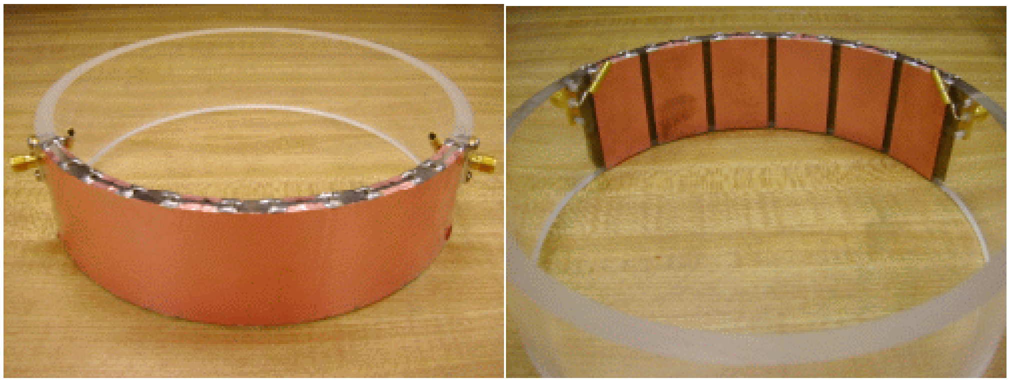

Figure 5-1. *Photos of the assembled six-element resonator*

5.1.2 Phantom load tests

Experiments with the six-element resonator were conducted with a non-biological load that resembles the dielectric properties of neck tissues. A cylinder of agarose gel with radius of 65mm and height of 38mm was built to represent a cross-sectional portion of the neck. The agarose gel, normally used to model the migration of DNA molecules, was designed to have a pH = 7.4, similar to that of blood. The gel was then placed inside of the six-element resonator, while using Kapton film to insulate it from the interior copper strips.

In order to validate the predicted results from the previous chapter, a test fixture, which acoustically excites the agarose load placed inside of the six-element resonator, was developed. A 4-inch loudspeaker, placed two feet below the agarose load, was used as a source of mechanical vibrations. The resonator and the agarose load were placed on top of a two feet tall plexiglass cylinder to minimize unwanted, external disturbances. Mechanical vibrations were caused in the agarose load by driving the loudspeaker at several acoustic frequencies with an audio amplifier. The majority of acoustic excitations are transferred to the agarose gel through air, however a certain amount of mechanical coupling occurs through the test fixture as well. The s-parameters of the resonator were monitored via a Hewlett Packard 8714ES network analyzer. Figure 5-2 shows the test setup used in this case.

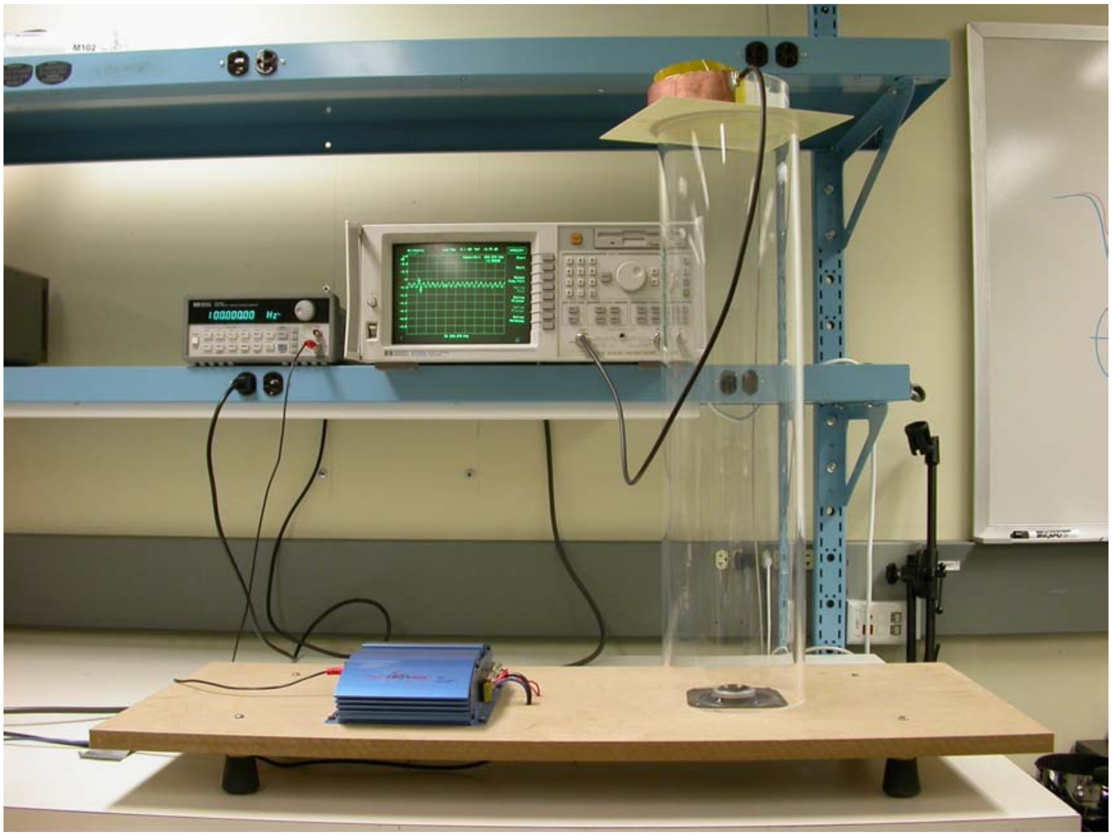

Figure 5-2: *Non-biological load test setup.*

Plots of the return loss (S_{11} in dB) versus frequency for the unloaded and loaded resonator are shown in Figure 5-3.

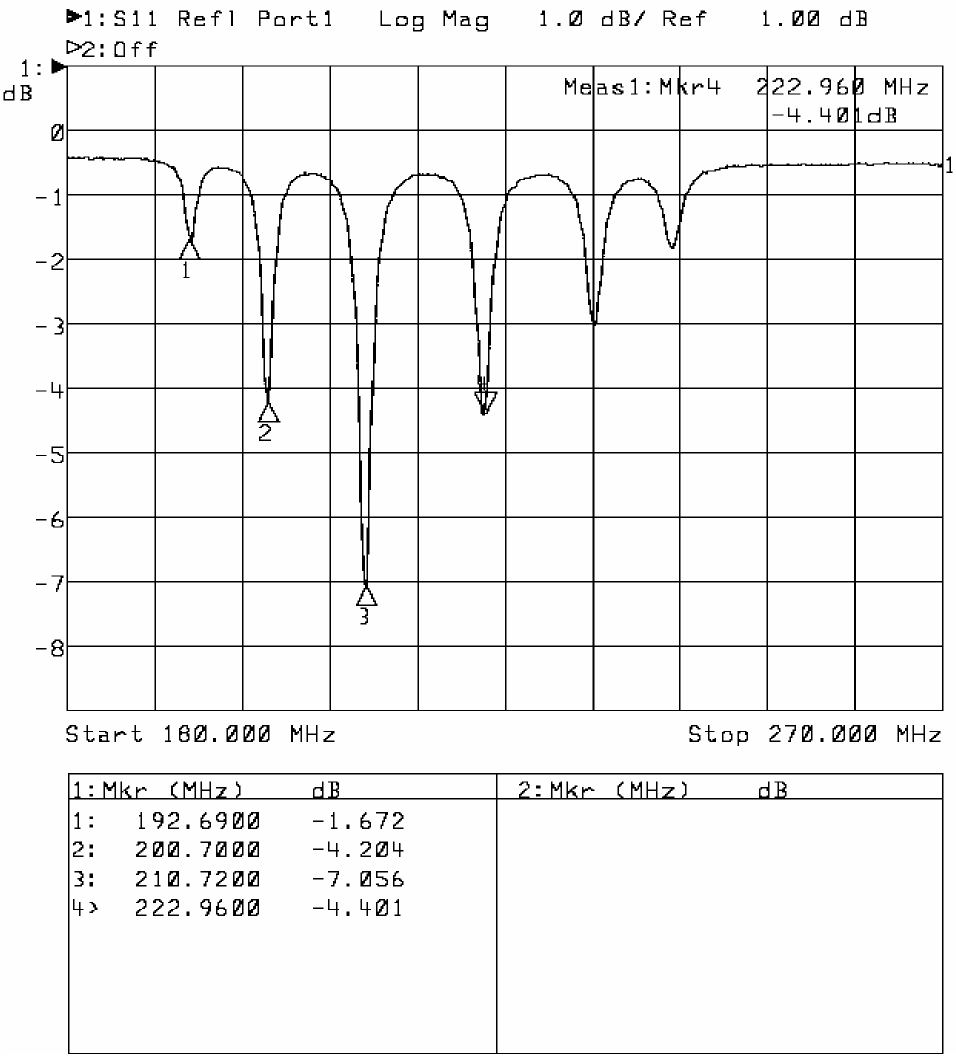

```
▶1:S11 Refl Port1   Log Mag   1.0 dB/ Ref   1.00 dB
▷2:Off
                          Meas1:Mkr4  222.960 MHz
                                      -4.401dB
Start 180.000 MHz                          Stop 270.000 MHz

1:Mkr (MHz)      dB          2:Mkr (MHz)      dB
1:   192.6900    -1.672
2:   200.7000    -4.204
3:   210.7200    -7.056
4>   222.9600    -4.401
```

a)

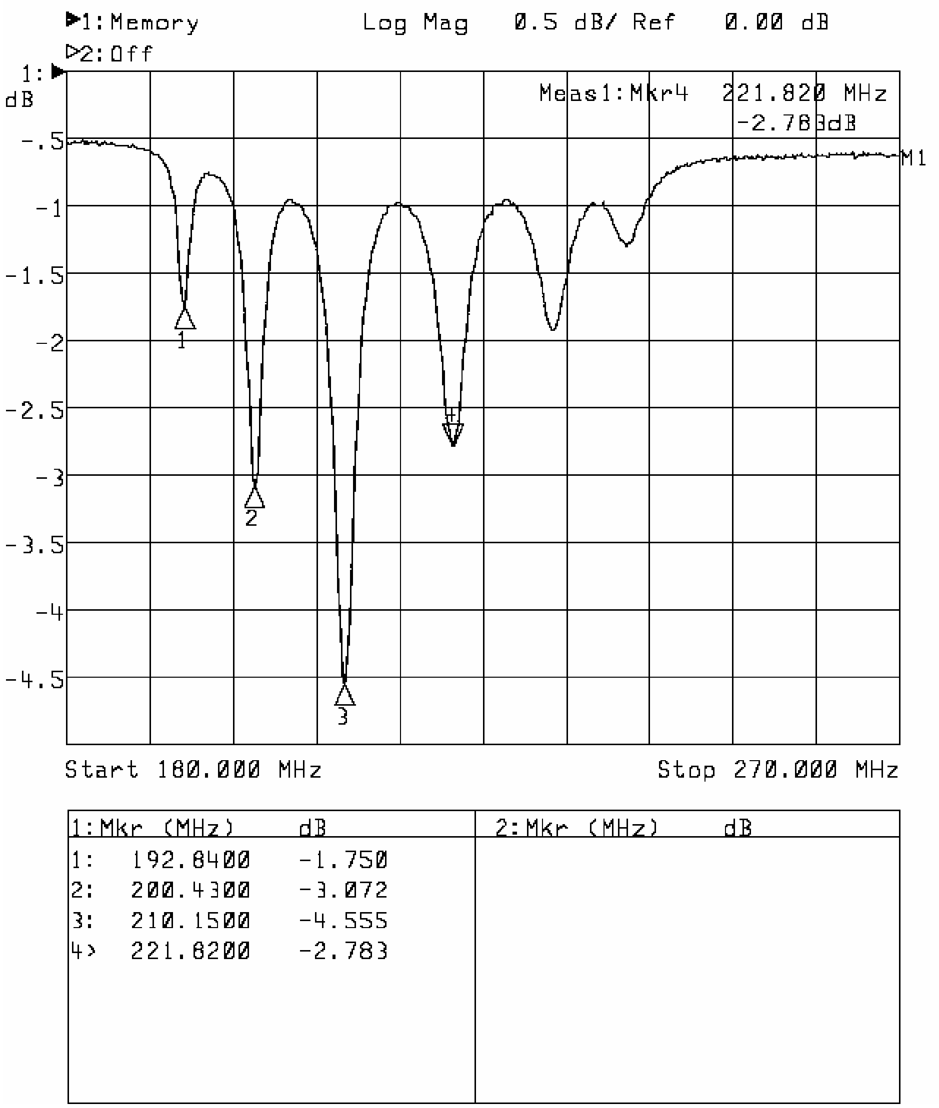

```
1:Mkr (MHz)    dB          2:Mkr (MHz)    dB
1:   192.8400   -1.750
2:   200.4300   -3.072
3:   210.1500   -4.555
4>   221.8200   -2.783
```

b)

Figure 5-3: S_{11} *(dB) of a) the unloaded resonator and b) the agarose-loaded resonator.*

We observe that in either case, mode 3 offers the best match to the 50Ω characteristic impedance of the coaxial cable. While the MTL method predicts an improvement in impedance matching at a particular mode by using a series capacitor (see Figure 3-9), we were unable to implement a capacitor with a wide tuning range.

However, the purpose of this experiment is to show that the six-element resonator detects acoustic vibrations in a phantom load regardless of a poor match.

While the loudspeaker was generating acoustic waves, the resonator was driven at its third resonant mode, and the s-parameters were monitored with the network analyzer in continuous wave (CW) mode (same as single frequency mode). Results for a 50Hz and 75Hz acoustic excitation are presented in Figure 5-4.

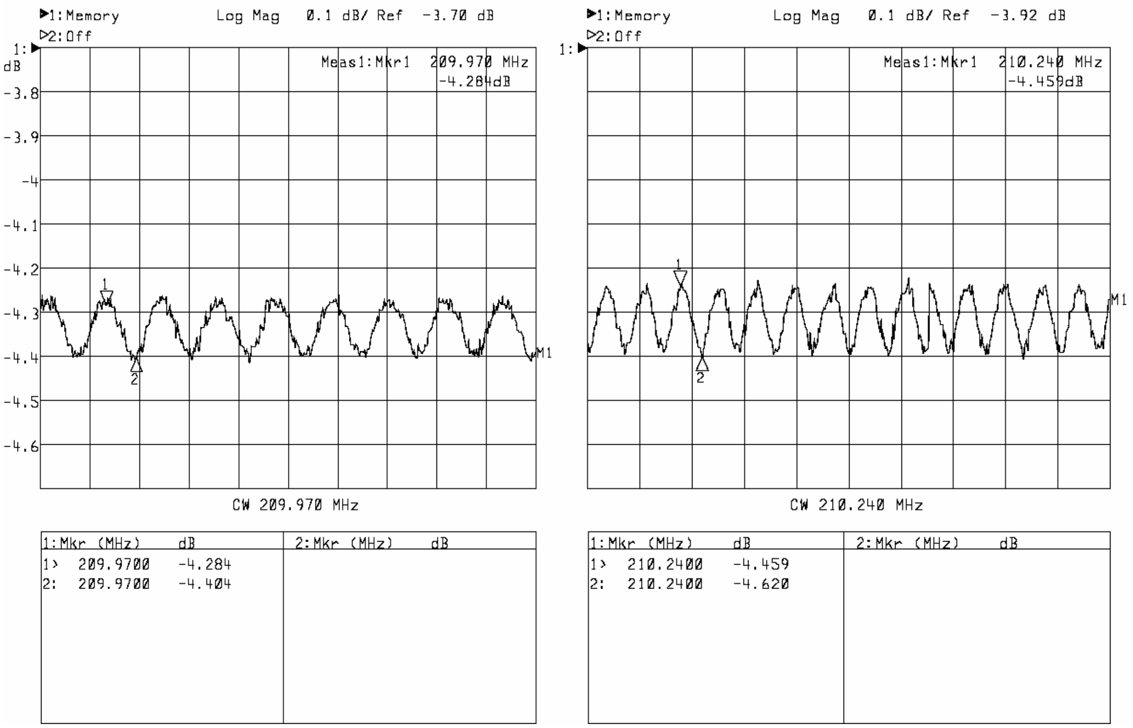

1:Mkr (MHz)	dB	2:Mkr (MHz)	dB
1› 209.9700	-4.284		
2: 209.9700	-4.404		

1:Mkr (MHz)	dB	2:Mkr (MHz)	dB
1› 210.2400	-4.459		
2: 210.2400	-4.620		

a) b)

Figure 5-4: *The s-parameters response of the six-element resonator in CW mode, while driven at its third resonance a) 50Hz excitation b) 75Hz excitation.*

The magnitude change in the return loss of the sensor is in the range of the one predicted by either the MTL or the FE method. Since everything was constructed by hand, control over geometrical variations in the width of the strips and the distance between them is poor. In addition, the biological model constructed with the simulation tools surely differs from the agarose load in terms of structure, dielectric constant and loss. When considering all the discrepancies with the modeling of the load and the resonator, experimental s-parameter measurements compare relatively well to MTL and FE predictions in terms of relative behavior and shape.

Sinusoidal patterns in the return loss at the 50 and 75Hz excitation frequencies demonstrate the ability of the sensor to capture changes in the load. While this test method vaguely resembles the speech production process, it verifies that the six-element resonator is able to detect load vibrations at speech frequencies. To remove doubts about influences from outside disturbances, such as stray fields or mechanical coupling through the structure, the CW experiment was repeated with the agarose load removed. The return loss in such case did not exhibit a sinusoidal excitation. While the six-element resonator detects relatively significant mechanical vibrations in a non-biological load, preliminary human subject tests indicated that the resonator is not suitable in detecting changes during the glottal cycle. The focus was then on performing tests with the parallel plate resonator.

5.2 Parallel-plate resonator

To confirm simulation results from Section 4, a physical prototype of the parallel plate speech sensor was constructed to the parameters of Table 4-4.

5.2.1 Construction

The physical prototype was constructed primarily of a flexible LEXAN sheet cut to a height of 38.1mm, length of 165mm and with parallel plates formed by placing adhesive-backed copper tape on the top surface of the former. The copper plates are placed 20mm apart and each one is 72.5mm long. In order to minimize parasitics, tuning inductors, matching capacitors and a standard SMA connector were placed on a mini-printed circuit board (PCB), manufactured with ExpressPCB [39]. The PCB was cut to size and placed on the space between the copper plates. The PCB features two wide traces on each end to allow for connection to the copper plates. These traces were carefully soldered directly to each copper plate. To add structural stability, room temperature vulcanising (RTV) was used to caulk around the edges of the PCB. A thin rectangular LEXAN sheet is attached to the back of the sensor to spread bending forces and add durability to the design. Part of the sensor is cut, and a slot is made to accommodate for wearing the sensor right below the Adam's apple. The resonator was enclosed in fabric material for added comfort, while Velcro was used to fasten the collar. Photos of the assembled resonator are shown below.

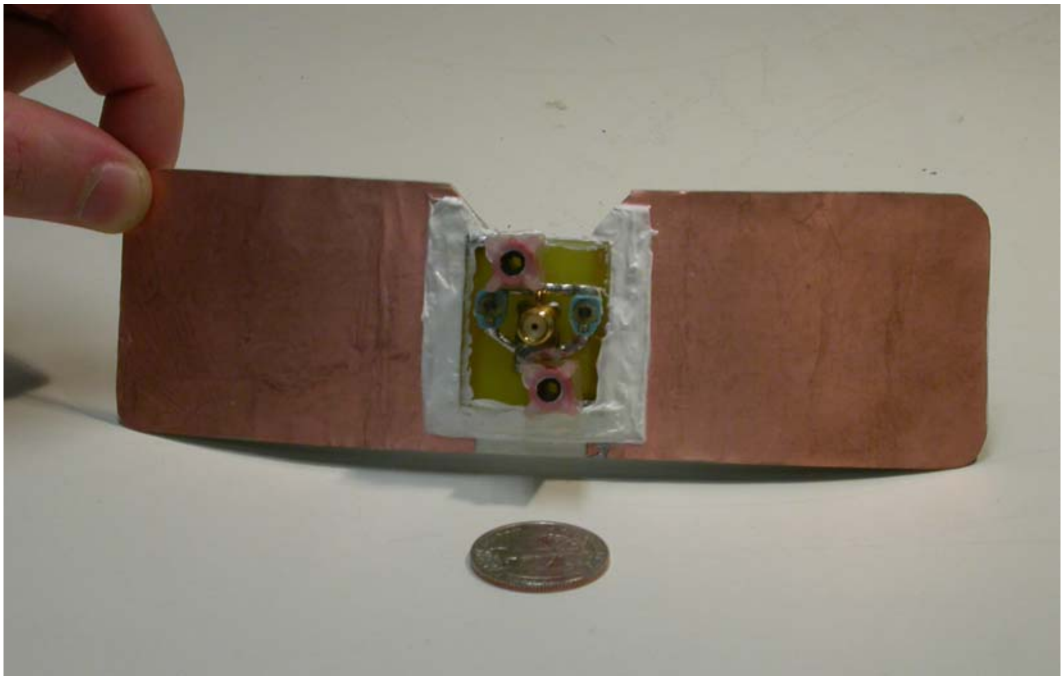

a)

b)

Figure 5-5. *Photographs of the PPRES sensor: (a) without fabric, (b) with fabric cover.*

5.2.2 Bench testing

All the experiments conducted with the parallel plate resonator utilized human subjects. As in the case of the six-element resonator, a relatively broad frequency range (20-70MHz) was used to find its resonance with an HP 8714ES network analyzer. S_{11} sweeps for a female and a male subject are shown in Figure 5-6 and Figure 5-7, respectively.

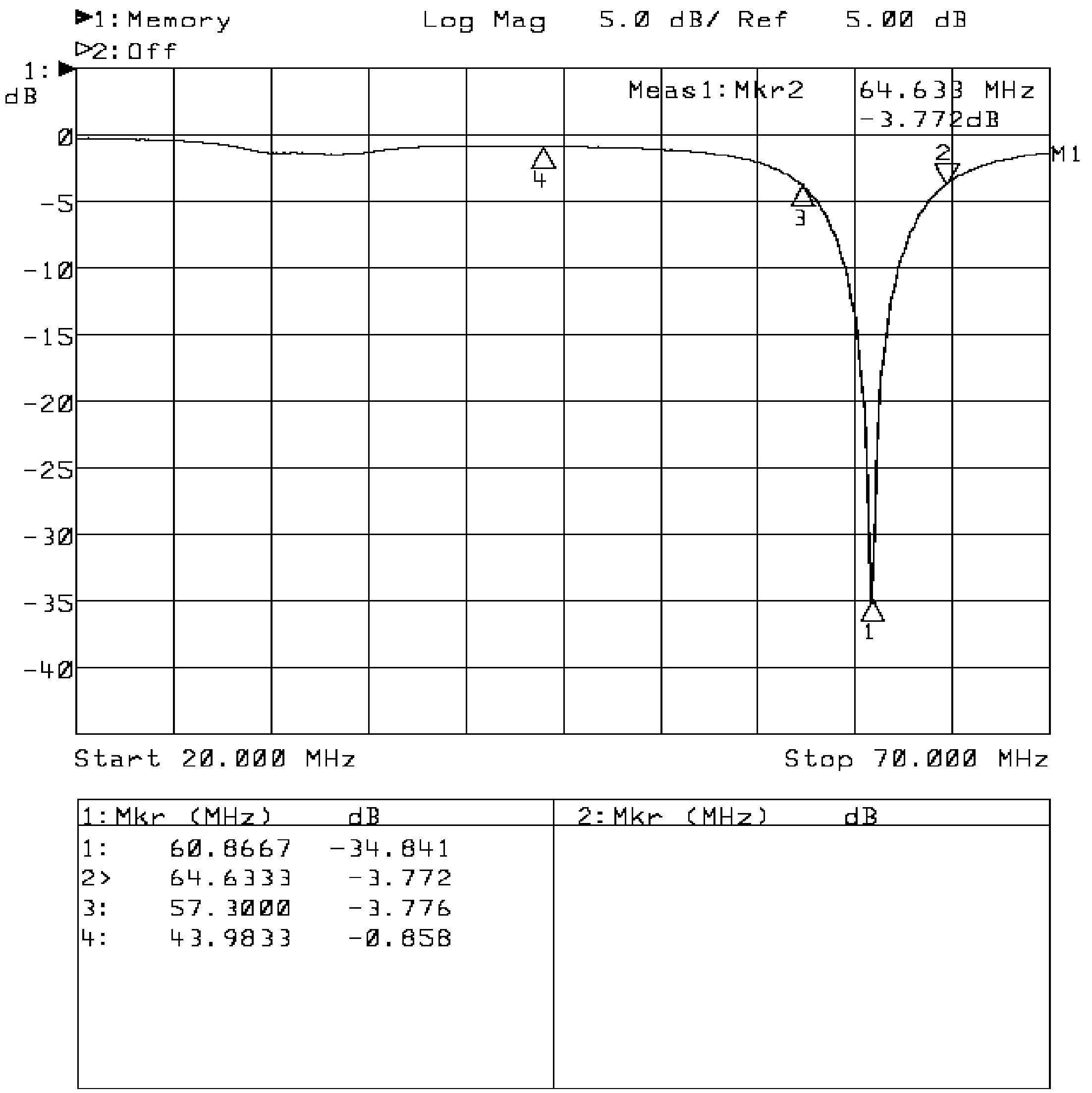

```
1:Mkr (MHz)      dB           2:Mkr (MHz)      dB
1:    60.8667  -34.841
2>    64.6333   -3.772
3:    57.3000   -3.776
4:    43.9833   -0.858
```

Figure 5-6: S_{11} *for a female subject*

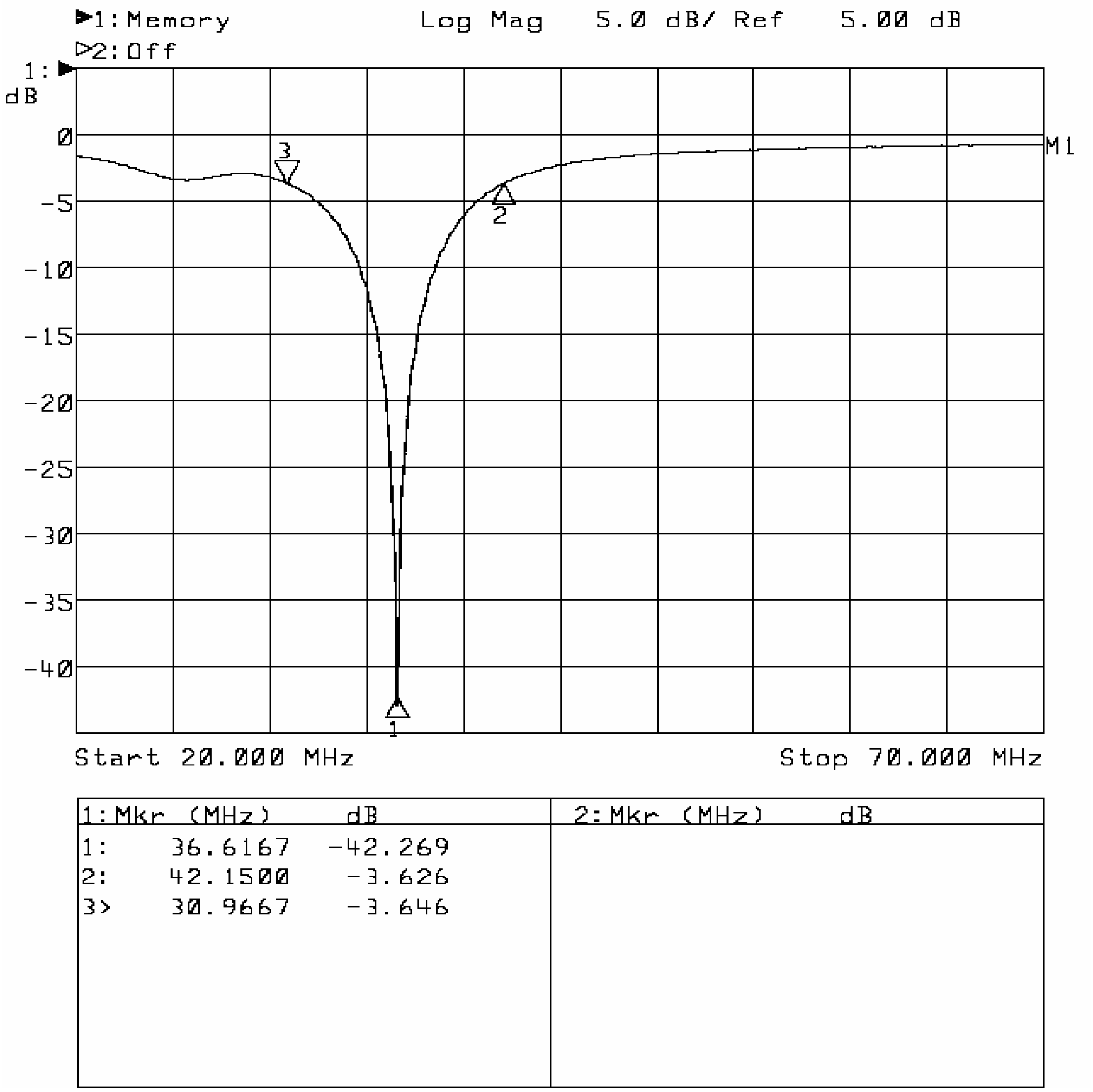

```
1:Mkr (MHz)      dB              2:Mkr (MHz)      dB
1:     36.6167  -42.269
2:     42.1500   -3.626
3>     30.9667   -3.646
```

Figure 5-7: S_{11} *for a male subject*

These waveforms match well to the ones predicted from the FEM results, especially when considering all the non-idealities in the modeling of the sensor and the load. The resonant frequencies are different between the male and the female subject. This is due to the fact that the female subject allowed more slack when wearing the sensor. For the male subject the sensor was driven near its resonance in continuous wave (CW) mode and the resulting glottal waveform was recorded with the network analyzer.

Figure 5-8 shows the PPRES sensor waveform while the male subject is humming at different frequencies.

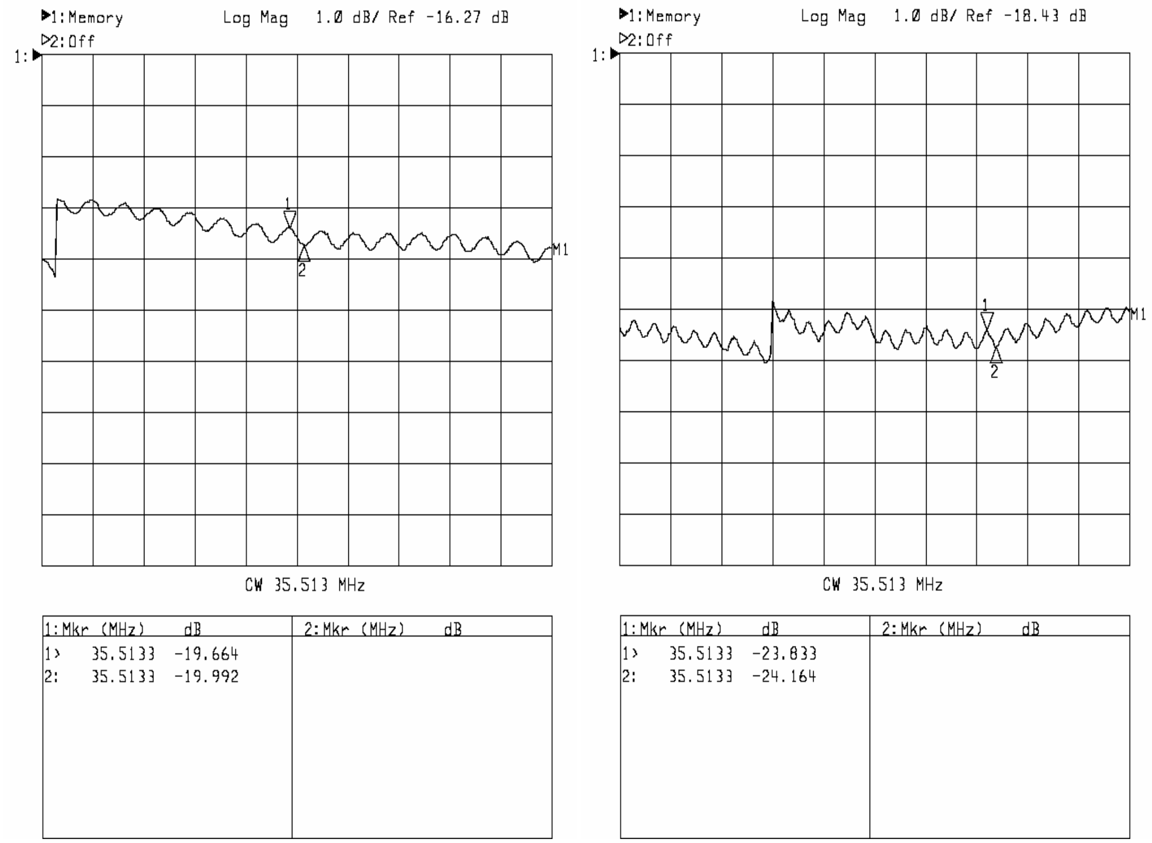

1:Mkr (MHz)		dB	2:Mkr (MHz) dB
1›	35.5133	-19.664	
2:	35.5133	-19.992	

1:Mkr (MHz)		dB	2:Mkr (MHz) dB
1›	35.5133	-23.833	
2:	35.5133	-24.164	

a) b)

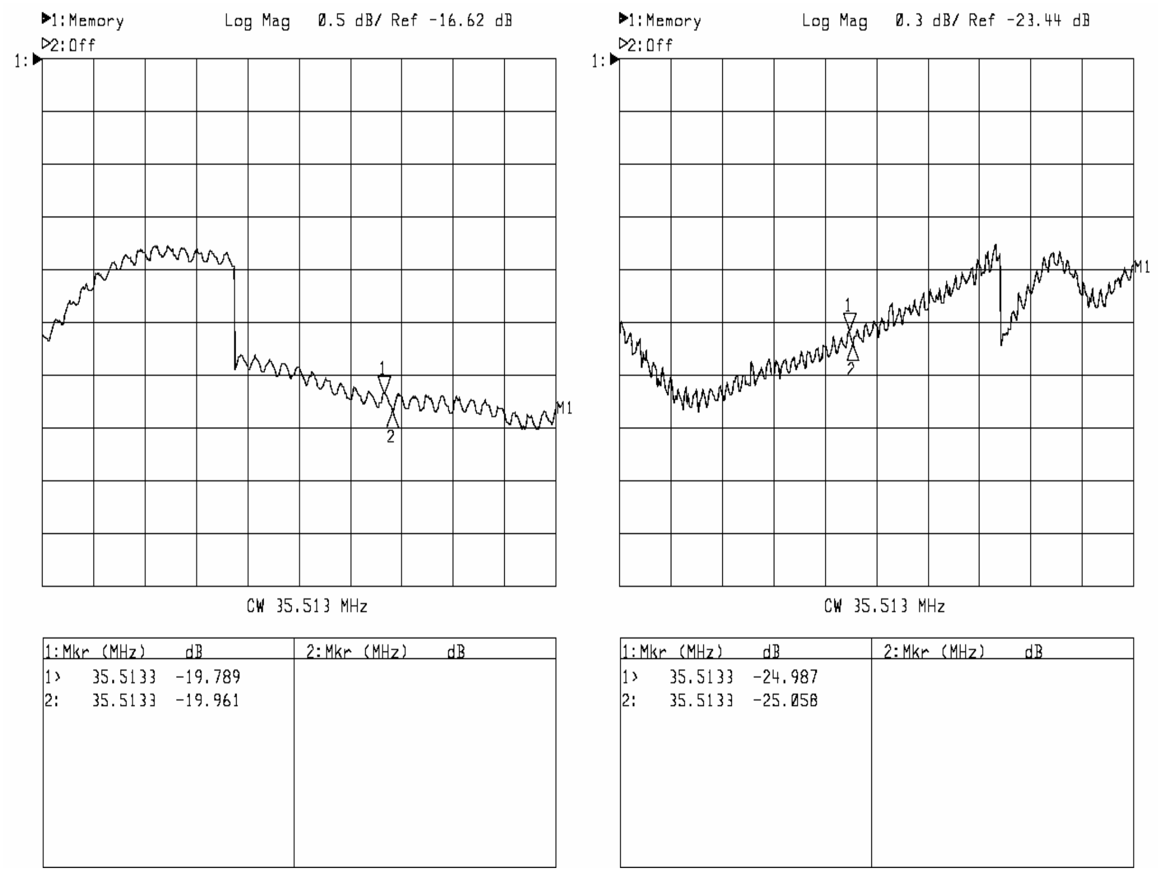

```
1:Mkr (MHz)    dB          2:Mkr (MHz)    dB
1>   35.5133  -19.789
2:   35.5133  -19.961
```

```
1:Mkr (MHz)    dB          2:Mkr (MHz)    dB
1>   35.5133  -24.987
2:   35.5133  -25.058
```

c) d)

Figure 5-8: *Tests in CW mode for a male subject when humming at a) 85.7Hz, b) 142.86Hz, c) 214.3Hz and d) 342.86Hz.*

The magnitude scale was set 1dB/division in the first two plots, 0.5dB/division in the third plot and 0.3 dB/division in the fourth plot. This was done to facilitate the data gathering, since it is very difficult to capture a screenshot, while the trace is moving up and down. The sweep time for the analyzer was set at 175ms so each division on the screen corresponds to 17.5ms. To determine the fundamental frequency of each waveform, we can estimate the number of periods per division. In doing so, the fundamental frequencies for each waveform in Figure 5-8 are approximately: a) 85.7Hz, b) 142.86Hz, c) 214.3Hz and d) 342.86Hz. These values are well within the range of the fundamental frequencies (of the glottal flow) of normal speech. Because the sensor is well matched, it is sensitive even to minor changes resulting from neck movements, pulse, breathing etc. Note the low frequency drift due to other physiological changes (possibly pulse).

There are discrepancies in the magnitude change captured with the network analyzer in CW mode versus predicted results. The differences can be contributed to a large extent to the difference between the biological model and the actual neck, specifically to the size of the glottis. The FEM model captured the glottal cycle by assuming a fully closed versus a fully open glottis, which rarely ever occurs. In addition, since the resonance shifts continuously due to other physiological events, it is not possible to drive the sensor at resonance for a sustained period of time; hence, the measured change is less than predicted. Furthermore, looking back at the FEM plots, the change can be relatively small if the sensor is driven significantly off resonance. In fact, the closer to resonance we drive the sensor, the larger the magnitude change in S_{11}; magnitude changes as high as 2dBc have been observed in CW mode, yet unable to capture due to trace movement. It can also be observed that the magnitude drops off at higher acoustic frequencies, which can be attributed to either the equipment or the magnitude of variations getting smaller. A fair comparison between measured and predicted data can be made once a more accurate neck model, a resonance tracking system and an improved receiver system are implemented.

Nevertheless, preliminary tests indicate that the parallel plate sensor is able to detect a glottal waveform signal, which can be used to carry out standardized human subject testing and determine the sensor’s feasibility in high acoustic noise environments. Prior to conducting such tests the interface circuitry must be designed and tested.

5.3 Interface electronics

In order to carry out tests with the parallel plate resonator and capture the data on a personal computer, we must find a way to differentiate between the reflected voltage wave and the incident wave. This task is usually accomplished by utilizing circulators, SWR bridges or even directional couplers.

5.3.1 Circulator

Traditional circulators at the operating frequency of the parallel plate sensor are bulky, relatively narrowband and expensive. An alternate design that utilizes wide bandwidth amplifiers instead of ferrite magnets has been recently proposed and has proven to be effective [40]. The schematic for such device is shown in Figure 5-9. This design is expected to offer high reverse isolation, good impedance matching and low-distortion. By employing current-feedback amplifiers the bandwidth of the circulator can easily extend to frequencies over several hundreds MHz and beyond.

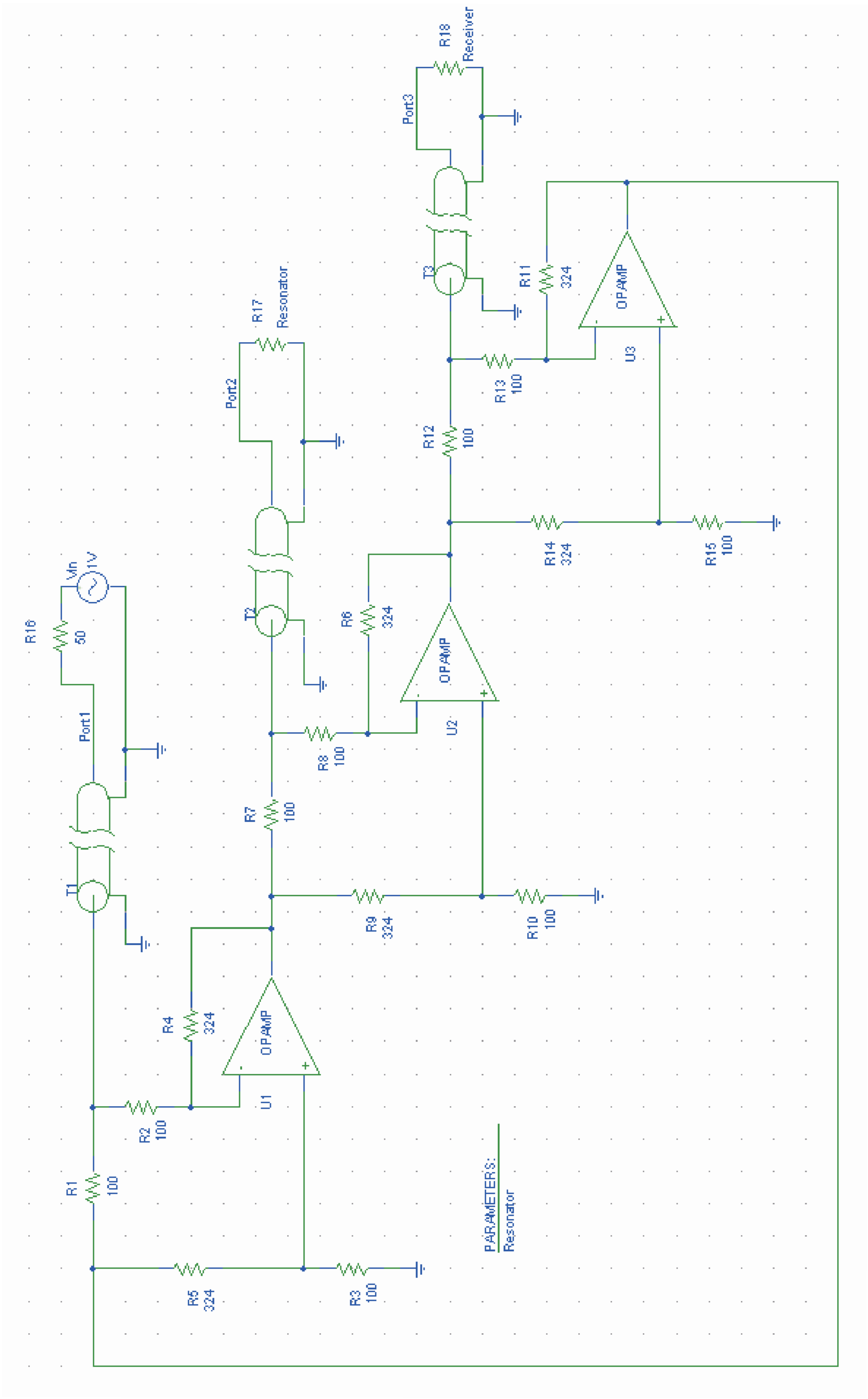

Figure 5-9: *A three-port circulator schematic.*

Construction and network analyzer tests

The circulator was constructed on a printed circuit board with the miniboard service from ExpressPCB (see Appendix B). The 50Ω microstrip lines are formed between the 80mil wide trace and a ground plane at the bottom of the 63mil thick FR4 material. While ExpressPCB offers a cost-effective solution to producing two-layer PCBs, 63mil is the only thickness available with such service. For a 50Ω transmission line the exact value of the trace width (with a 63mil thickness) was computed to be 111mil. Since this was deemed as an impractical value (too wide for the SMA connectors), the next best width value was chosen to be 80mil. The microstrip line impedance in such case is calculated to be 59.9Ω at 50MHz. This is different from the desired 50Ω, however the match is acceptable. A snapshot of the assembled circulator is shown in Figure 5-10.

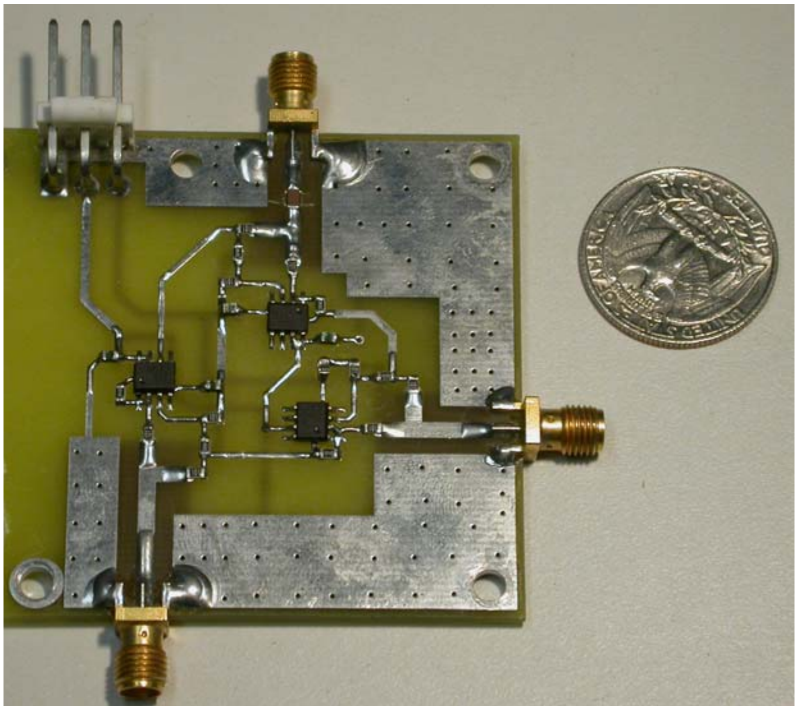

Figure 5-10: *Photo of the assembled circulator.*

Network analyzer tests were performed on the circulator to determine the input reflection coefficient, the transmission and isolation. Since the circulator has three identical ports, only three parameters need to be reported. The input reflection coefficient is simply $S_{11}(f)$ of port 1, while the other ports are terminated. Transmission is recorded as the forward gain from port 1 to 2, while port 3 is terminated. Isolation is recorded as the forward gain from port 1 to 3, while port 2 is terminated. These plots are provided in Figure 5-11.

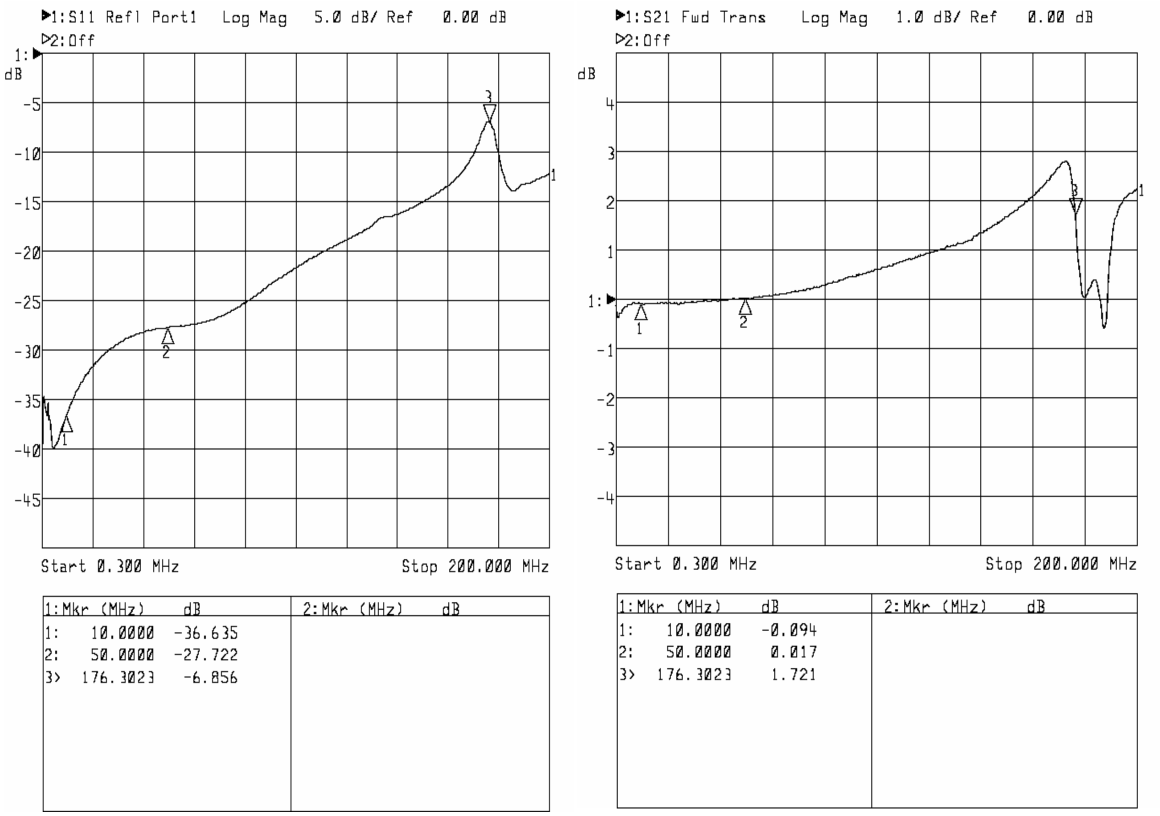

```
1:Mkr (MHz)     dB          2:Mkr (MHz)     dB
1:    10.0000  -36.635
2:    50.0000  -27.722
3>  176.3023    -6.856
```

```
1:Mkr (MHz)     dB          2:Mkr (MHz)     dB
1:    10.0000   -0.094
2:    50.0000    0.017
3>  176.3023     1.721
```

a)

b)

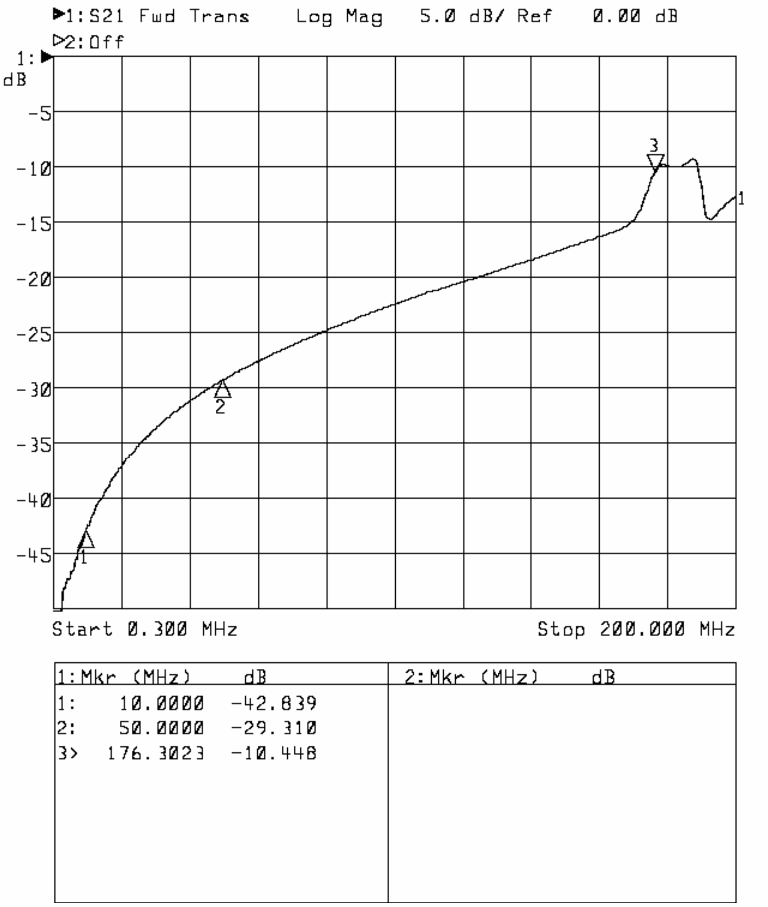

1:Mkr	(MHz)	dB	2:Mkr (MHz)	dB
1:	10.0000	-42.839		
2:	50.0000	-29.310		
3>	176.3023	-10.448		

c)

Figure 5-11: *Circulator S-parameter measurements with the HP 8714ES. a) input reflection coefficient b) transmission and c) isolation.*

From these plots, it can be seen that the circulator works well up to about 150MHz or so. If a flatter response is desired beyond such frequency, the PCB can be more carefully laid out to reduce parasitics and improve the response. Nevertheless, with the circulator offering the desired characteristics at the operation frequency of the parallel plate sensor, the main pieces are in place to conduct tests with human subjects and record the data digitally. A suggested topology of the drive and demodulating system is shown in Figure 5-12.

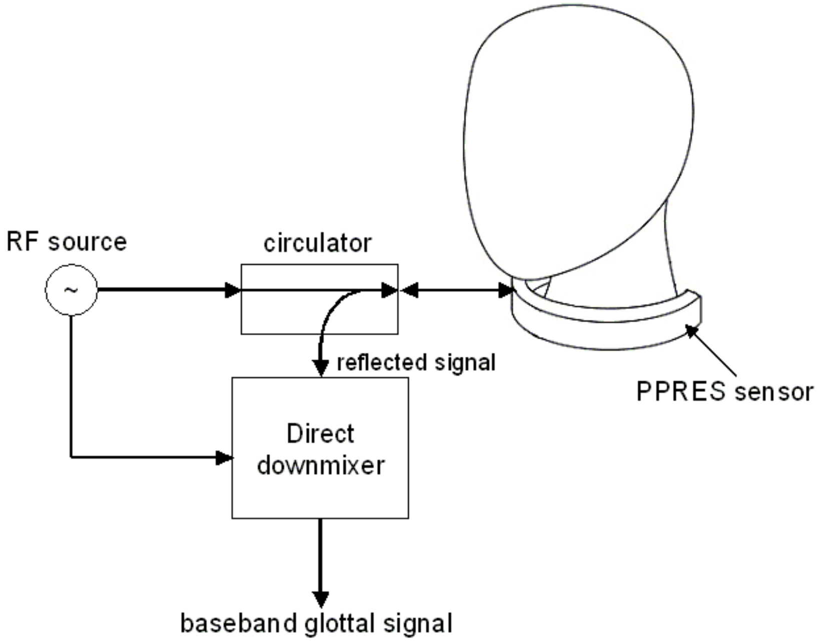

Figure 5-12: *Topology of the interface circuitry and receiver using the parallel plate resonator.*

An oscillator connected to port 1 of the circulator provides the desired RF drive at or near the resonance frequency of the PPRES sensor. Since no resonance tracking system is in place yet, manual tuning of the RF source is required to drive the sensor at its resonance. Port 2 of the circulator connects to the parallel plate resonator. The modulated signal is returned to port 3. This signal can be directly demodulated by downmixing it with the drive signal at the appropriate level. The baseband signal contains the glottal waveform as well as other lower frequency movements, such as swallowing, pulse etc.

For a full-scale of human subject testing and the performance of the PPRES sensor in standardized high acoustic noise environments, the interested reader is referred to another thesis [41], completed in conjunction with this one.

6 Conclusions

This thesis determined the feasibility of the GRES sensor for the purpose of non-acoustic voiced speech measurements. Two configurations were investigated: the six-element resonator, inspired by high-field magnetic resonance imaging, and the parallel plate resonator, a novel design. Both sensors were modeled with available software tools that can predict their behavior during changes in the glottal state. These tools include the MTL method, for rapid performance evaluation and optimization, and the FEM, when further refinement of the model and more accurate results are desired. In addition, the FEM is applicable to any three-dimensional electromagnetic structure, while the MTL is not.

Experimental results conducted with the six-element resonator were presented to confirm its sensitivity to acoustic vibrations in a non-biological phantom load. However, the six-element resonator is unfeasible in detecting small changes that occur during the glottal cycle. On the other hand, the parallel plate resonator is capable of directly detecting the glottal flow waveform through a capacitive sensing technique. Bench testing demonstrates the ability of the parallel plate sensor to offer more than adequate sensitivity and sufficient acoustic bandwidth to cover at least normal speaking glottal frequencies. The sensor is also unaffected by complicated scattering environments because it responds to the composite relative permittivity of a cross-sectional portion of the neck. The design is tunable, allowing for different people to use it, and it can be manufactured at a very low cost. The sensor may additionally provide some information about the articulation process, i.e. possibly some skin vibration due to acoustic coupling, but such claims have not yet been established. Finally, conformance to FCC guidelines regarding safe operating power levels was investigated. In addition to sensor results, an efficient method was employed to distinguish between the reflected and incident voltage, which allows for data recording and real time processing.

While the GRES sensor provides exceptional results, the project has a lot of new challenges to meet in order to generate a final product someday.

6.1 Recommendations

Recommendations for future work address two major avenues of improvement:

1) Optimization of the parallel plate sensor
2) Practical implementation issues

The sensor can be designed to operate at a higher frequency, where wave propagation plays a more prominent role. By operating at a higher frequency the size of the sensor would be reduced and the fields can be concentrated near the front of the neck, where the vocal folds are located. An optimization program can be used to investigate the effect of varying different geometrical parameters. Without an optimization program the FEM simulations would take too long, so in that case a faster modeling tool can be employed or even developed. The biological load model can be further refined to more accurately predict changes during the glottal state, although such step would probably require more computational resources (or a different platform like Unix). But with the new 64-bit computers maybe that will not be a problem in the future. The operation of the sensor can be better understood once skin and other tissue vibrations are properly modeled, and by having a longer neck model than the sensor structure (to account for stray fields in the z-direction).

With regard to practical issues, the sensor's comfort level can be improved by implementing it on a flexible PCB. Structural stability must be kept in mind when designing the flexible PCB, since the sensor could break or crack by repeated usage. In terms of interface electronics, a driving circuit that is able to track changes from non-speech related activities, such as neck movements, swallowing, pulse, must be designed and implemented. In addition to tracking the resonance frequency, the driving circuit must be able to maintain a proper impedance match. A resonance tracking system that utilizes a phase locked loop (PLL) for relatively high Q (larger than 10) applications is described in [42]. While the network analyzer provides measurements for quick comparison to predicted results, a better receiver design is required for future experiments. Due to the unavailability of tools, the noise figure of the circulator that was implemented was not measured. This task can be accomplished by utilizing a noise figure meter. Finally, once noise sources for the front-end and receive subsystem are modeled, the drive input power can be optimized based on the SNR of the system.

References

[1] Burnett, G.C., "The Physiological Basis of Glottal Electromagnetic Micropower Sensors (GEMS) and Their Use in Defining an Excitation Function for the Human Vocal Tract." Ph.D. dissertation, University of California, Davis, 1999.

[2] Boves, L., and Cranen. B., "Evaluation of glottal inverse filtering by means of physiological registrations," *in* 'Proceedings of the International Conference on Acoustics, Speech, and Signal Processing (ICASSP)', Vol. 7, pp. 1988–1991.

[3] Hess, W., *Pitch Determination of Speech Signals: Algorithm and devices*, New York: Springer-Verlag, 1983.

[4] Defense Advanced Research Projects Agency, "Advanced Speech Encoding," [Online document], [2002 November 15], Available at HTTP: http://www.darpa.mil/ato/programs/vocorder.htm

[5] Ng, L.C., Burnett, G.C., Holzrichter, J.F., Gable, T.J., "Denoising of human speech using combined acoustic and EM sensor signal processing," in *Proceedings of the International Conference on Acoustics, Speech, and Signal Processing (ICASSP)*, Istanbul, Turkey, June 2000, vol. 1, pp. 229-232.

[6] Italian National Research Council, Institute for Applied Physics, "Dielectric Properties of Body Tissues," [Online document], [2003 February 17], Available at: http://niremf.iroe.fi.cnr.it/tissprop/

[7] Clark, J. and Yallop, C., *An Introduction to Phonetics and Phonology,* 2nd edition, Oxford, UK: Blackwell Publishers, 1995.

[8] Titze, I.R., *Principles of Voice Production,* Englewood Cliffs, NJ: Prentice-Hall, 1994.

[9] American Medical Association, "AMA (Atlas) Respiratory System -- Structure Detail," [Online document], [2003 March 21], Available at HTTP: http://www.ama-assn.org/ama/pub/category/7166.html

[10] Prentice Hall Inc, "The Respiratory System," [Online document], [2003 April 12], Available at HTTP: http://media.pearsoncmg.com/ph/esm/esm_martini_fundanaphy_5/bb/obj/23/CH23/html/ch23_5_1.html

[11] Gray, H., *Anatomy of the Human Body*, 20th edition, New York: Bartleby.com, 2000.

[12] Mahshie, J., "The Morphology of the Vocal Fold," [Online document], [2003 June 3], Available at HTTP: http://aslp.gallaudet.edu/jmahshie/714/larynx/sld013.htm

[13] Flanagan, J.L., *Speech Analysis Synthesis and Perception*, New York: Springer-Verlag, 1972.

[14] Fry, D.B., Ed., *Acoustic Phonetics*, Cambridge, UK: Cambridge University Press, 1976.

[15] Minifie, F.D., Hixon, T.J., Williams, F., Eds., *Normal Aspects of Speech, Hearing, and Language,* Englewood Cliffs, NJ: Prentice-Hall, 1973.

[16] Campbell, W., Quatieri, T., Campbell, J., and Weinstein, C., 2003, Multimodal speaker authentication using nonacoustic sensors, in 'Workshop on Multimodal User Authentication', Santa Barbara, CA.

[17] Holzrichter, J.F., Burnett, G.C., Ng, L.C., and Lea, W.A., "Speech articulator measurements using low power EM-wave sensors," *Journal of the Acoustical Society of America*, vol. 103, no. 1, pp. 622-625, Jan.1998.

[18] Burnett, G.C., Holzrichter, J.F., Gable, T.J., and Ng, L.C., "Direct and indirect measures of speech articulator motions using low power EM sensors," in *Proceedings of the 14th International Congress of Phonetic Sciences*, San Francisco, CA, Aug. 1999, pp. 2247-2249.

[19] Burnett, G.C., Holzrichter, J.F., Gable, T.J., and Ng, L.C., "The use of glottal electromagnetic micropower sensors in determining a voiced excitation function," in *Proceedings of the 138th Meeting of the Acoustical Society of America*, Columbus, OH, Nov. 1999.

[20] Nikolova, N.K., "Other Practical Dipole/Monopole Geometries Matching Techniques for Dipole/Monopole Feeds," [Online document], [2003 May 5], Available at HTTP: http://www.ece.mcmaster.ca/faculty/georgieva/antenna_dload/Antennas_L10.pdf

[21] Balanis, C., *Antenna Theory: Analysis and Design*, 2nd edition, New York: John Wiley & Sons, 1996.

[22] Poynting Group, "Balun tutorial," [Online document], [2003 May 10], Available at HTTP: http://www.poynting.co.za/tech_training/tut_balun.shtml

[23] The American Radio Relay League, *The ARRL Handbook for Radio Amateurs,* 78th edition, Newington, CT: ARRL-the national association for Amateur Radio, 2001.

[24] Bowick, C., *RF Circuit Design,* Indianapolis, IN: H.W. Sams, 1982.

[25] Ludwig, R., and Bretchko, P., *RF Circuit Design: Theory and Applications,* Upper Saddle River, NJ: Prentice Hall, 2000.

[26] Pozar, D., *Microwave Engineering,* 2nd edition, New York: John Wiley & Sons, 1998.

[27] Bogdanov, G. and Ludwig, R., "Coupled Microstrip Line Transverse Electromagnetic Resonator Model for High-Field Magnetic Resonance Imaging," *Magnetic Resonance in Medicine*, vol. 47, no. 3, pp. 579-593, Mar. 2002.

[28] Brown, D.R., Ludwig, R., Pelteku, A., Bogdanov, G., and Keenaghan, K., "A Novel Non-Acoustic Speech Sensor," *Measurement Science and Technology*, submitted December 2003.

[29] Harpen, M.D., "Equivalent circuit for birdcage resonators." *Magnetic Resonance in Medicine*, vol. 29, pp. 263-268, 1993.

[30] Pascone, R., Vullo, T., Farrelly, J., and Cahill, P.T., “Explicit treatment of mutual inductance in eight-column birdcage resonators.” *Magnetic Resonance Imaging*, vol. 10, pp. 401-410, 1992.

[31] Tropp, J., “Mutual inductance in the birdcage resonator.” *Journal of Magnetic Resonance*, vol. 126, pp. 9-17, 1997.

[32] Bogdanov, G., “Radio-Frequency Coil Design for High Field Magnetic Resonance Imaging.” Ph.D. diss., Worcester Polytechnic Institute, Worcester, 2002.

[33] Van Der Vorst, H. A., *Iterative Krylov methods for large linear systems,* New York: Cambridge University Press, 2003.

[34] Bossavit, A., “Whitney forms: a class of finite elements for three dimensional computations in electromagnetism,” *IEE Proc.*, Part A, Vol. 135, No. 8, 493–500, Nov. 1988.

[35] Berenger, J. P., "A perfectly matched layer for the absorption of electromagnetic waves", *J. Comp. Phy.*, vol. 114, pp. 185-200, Oct. 1994.

[36] Sacks, Z. S., Kingsland, D. M., Lee, R., and Lee, J-F., "A perfectly matched anisotropic absorber for use as an absorbing boundary condition", *IEEE Trans. Antennas and Propagation, vol. 43, pp. 1460-1463, Dec. 1995.*

[37] Rohen, J. W., and Yokochi, C., *Color Atlas of Anatomy: A Photographic Study of the Human Body,* 3rd edition, New York, N.Y.: Igaku-Shoin Medical Publishers Inc., 1993.

[38] Federal Communications Commission, “Questions and Answers about Biological Effects and Potential Hazards of Radiofrequency Electromagnetic Fields,” [Online document], [2003 July 20], Available at HTTP: http://www.fcc.gov/Bureaus/Engineering_Technology/Documents/bulletins/oet56/oet56e4.pdf

[39] Engineering Express --- expresspcb.com, “PC board layout software and low cost board manufacturing service,” [Online software], [2003 January 20], Available at HTTP: http://www.expresspcb.com/ExpressPCBHtm/Download.htm

[40] Wenzel, C., “Low Frequency Circulator/Isolator Uses No Ferrite or Magnet,” [Online document], [2003 February 10], Available at HTTP: http://www.wenzel.com/pdffiles/RFDesign3.pdf

[41] Keenaghan, K. M., “A Novel Non-Acoustic Voiced Speech Sensor: Experimental Results and Characterization.” Master’s thesis, Worcester Polytechnic Institute, Worcester, 2004.

[42] Gokcek, C., “Tracking the resonance frequency of a series RLC circuit using a phase locked loop,” [Online document], [2003 August 4], Available at HTTP: http://www.egr.msu.edu/~gokcek/freqtrack.pdf

[43] Fabre P., “Un procede electrique percutane d’inscription de l’accolement glottique au cours de la phonation: glottographie de haute frequence,” *Bull. Nat. Med.*, pp. 66–69, 1957.

[44] Farnsworth, D.W., “High speed motion pictures of the human vocal cords,” *Bell Labs. Rec.*, vol. 18, pp. 203–208, 1940.

[45] Goldshen, A.J., Garcia, O., and Petajan, E., “Continuous optical speech recognition,” in *Proceedings of the 28th IEEE Asilomar Conference on Signals Systems, and Computers*, 1994.

[46] Jeffrey, A., *Advanced Engineering Mathematics,* Orlando, FL: Harcourt/Academic Press, 2002.

[47] Kinsler, L. and Frey, A., *Fundamentals of Acoustics,* 2nd edition, New York: Wiley, 1962.

[48] Krauss, H.L, and Bostian, C.W., *Solid State Radio Engineering,* 3rd edition, New York: John Wiley & Sons, 1980.

[49] Lapidus, L., *Numerical solution of partial differential equations in science and engineering*. New York: Wiley-Interscience, 1999.

[50] Ludwig, R., Bogdanov G., Sullivan, J.M., King, J.A., and Ferris, C., “A coupled microstrip line TEM resonator model for high-field magnetic resonance imaging”, at *HiRes Imaging in Small Animals*, Sept. 2001, p. 194.

[51] MacNeilage, P. F., Ed., *The production of Speech*, New York: Springer-Verlag, 1983.

[52] Story, B. H., “Physical modeling of voice and voice quality,” [Online document], [2003 June 21], Available at HTTP: http://www.u.arizona.edu/~bstory/voqual03_story.pdf

[53] Teager, H., and Teager, S., “Evidence for nonlinear sound production mechanisms in the vocal tract,” in *Speech Production and Speech Modeling*, (W. Hardcastle and A. Marchal, eds.), vol. D 55 of NATO ASI Series, Kluwer Academic Publishers, pp. 241-261.

[54] Tsuk, M.L., and Kong, J.A., “A hybrid method for the calculation of the resistance and inductance of transmission lines with arbitrary cross sections.” IEEE *Transaction on Microwave Theory and Techniques*, vol. 39, pp. 1338-1347, 1991.

[55] Wheeler, H.A., “Formulas for the skin effect.” *Proceedings of the IRE*, vol. 30, pp. 412-424, 1942.

Appendix A. Resonator Components

Component listing for the six-element resonator

Quantity	Manufacturer	Part number	Description	Supplier	Supplier part number
1	Plastics Unlimited	N/A	Cast Acrylic, 6"OD, 1/4" thick	Plastics Unlimited	N/A
13"	N/A	N/A	Copper tape, 2" wide, 1.5mil thick	McMaster-Carr	76555A654
48	Kemet	C1206C270J5GACTU	Ceramic 27pF cap, 1206, NPO	Digikey	399-1198-1-ND
2	Johnson Components	142-0701-621	SMA, Jack, flange mount	Digikey	J492-ND
2	Building Fasteners	NY PMS 256 0025 PH	2-56 Nylon screw	Digikey	H530-ND

Component listing for the parallel plate resonator

Quantity	Manufacturer	Part number	Description	Supplier	Supplier part number
1	Plastics Unlimited	N/A	LEXAN sheet, 0.5mm thick	Plastics Unlimited	N/A
6"	N/A	N/A	Copper tape, 2" wide, 1.5mil thick	McMaster-Carr	76555A654
2	Coilcraft	144-08J12	Tunable inductor, 0.344 μH nominal	Coilcraft	144-08J12
2	Sprague-Goodman	GCL40000	Trimmer cap, 1-40pF, Blue	Digikey	SG1037-ND
1	Amp/Tyco Electronics	221789-1	SMA, Jack, Vertical PCB	Digikey	A24691-ND

Appendix B. Circulator PCB layout and circuit components

A snapshot of the circulator PCB layout is provided below along with the components used during assembly.

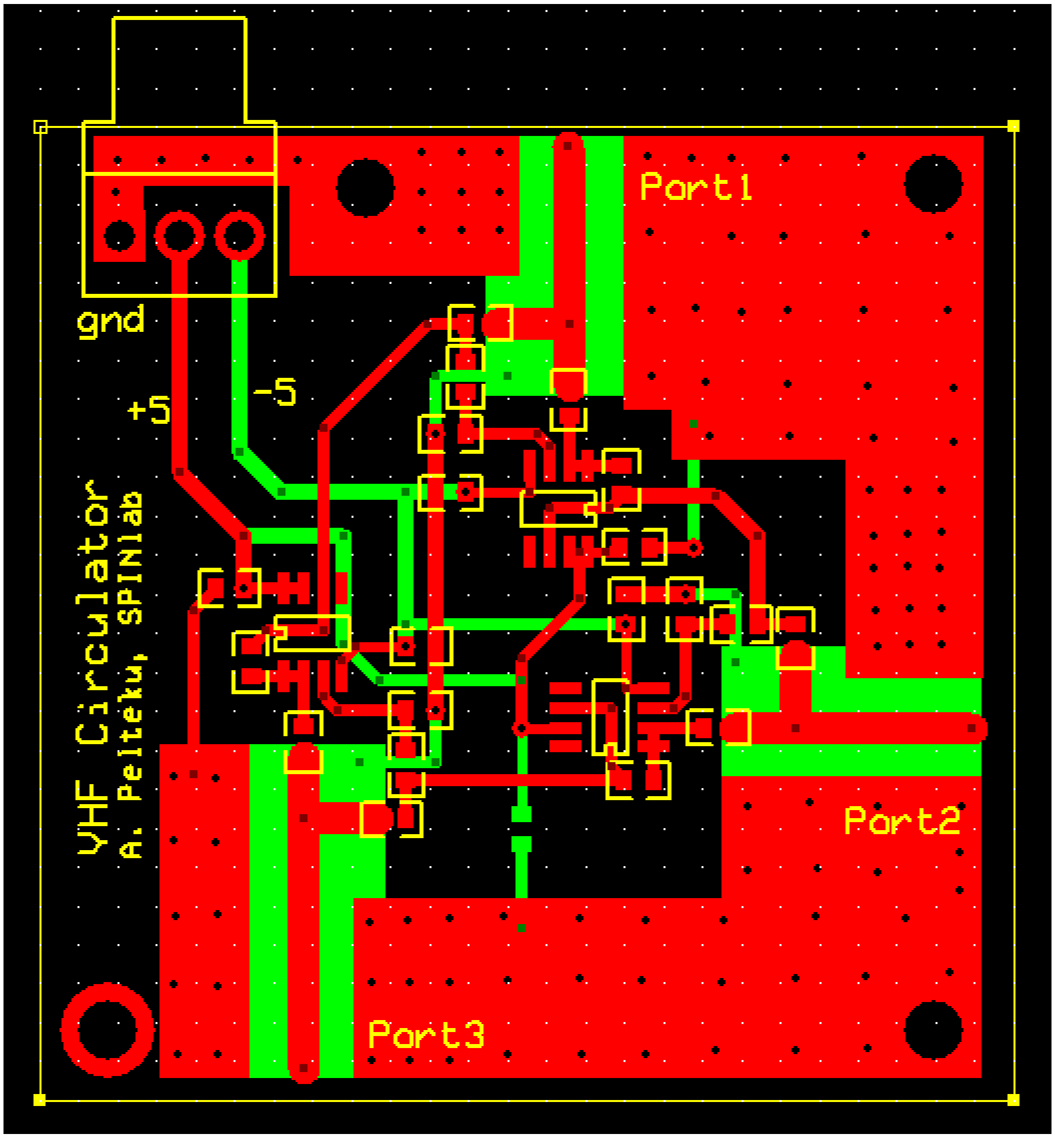

Component listing

Quantity	Manufacturer	Part number	Description	Supplier	Supplier part number
3	Analog Devices	AD8001AR	Current feedback amplifier	Analog Devices	AD8001AR
6	Panasonic-ECG	ERJ-6ENF3240V	Chip resistor, 1/10W, 324ohm, 0805	Digikey	P324CCT-ND
9	Susumu Co Ltd.	RR1220P-101-D	Chip resistor, 1/10W, 100ohm, 0805	Digikey	RR12P100DCT-ND
6	Panasonic-ECG	ECP-U1C104MA5	0.1uF cap, 16V, 0805	Digikey	PCF1126CT-ND
3	Johnson Components	142-0711-821	SMA, Jack, End launch PCB	Digikey	J629-ND
1	Molex/Waldom Electronics	26-60-5030	Connector Header 3POS, .156	Digikey	WM4641-ND
1	Molex/Waldom Electronics	09-50-8033	Connector housing, .156	Digikey	WM2112-ND
4	Molex/Waldom Electronics	08-50-0106	Crimp terminal, .156	Digikey	WM2300-ND